Imperial College London

Mechanical performance of transparent laminated materials for aircraft

Yi Wang

Mechanics of Materials Division

Department of Mechanical Engineering

Imperial College London

A thesis submitted for the degree of Doctor of Philosophy of

Imperial College London and the Diploma of Imperial College

March 2016

Declaration of Originality

The work presented in this thesis was produced by me during the course of my PhD studies. Where contributions by others are used, they have been appropriately referenced in the text and in the bibliography.

Copyright Declaration

Abstract

To fully understand mechanical and structural performance of laminated glass, seven laminated cases were designed to assess the influence of glass types, polymer interlayer thickness, polymer interlayer types and multi-layered interlayer.

An innovative apparatus combining 3D-Digital-Image-Correlation and ring on ring tests have been tested successfully, major strain and out of plane displacement at the supporting side were monitored. Novel sabot design helped the rubber projectile to eject without deformation in gas gun tests. The third innovative design was the gas gun system which allowed a stereo system of two high speed cameras for 3D-Digital-Image-Correlation and one camera monitoring impact performance, strain gauge system, and detecting velocity to be synchronised at the same time.

Regarding major research findings, for monolithic glasses, an approximate 0.8% major failure strain was identified regardless of its thickness which was used as a failure criterion for laminated glass. For laminated glasses, an increase of thermoplastic-polyurethane thickness will allow laminate to absorb more energy at quasi static and low velocity ranges, but lower the supporting face strain at high velocity. Chemically strengthened glass used as frontal glass layer has better performance in terms of energy consumption in quasi static and low velocity ranges comparing to thermally strengthened glass. Different types of interlayer have different functionalities. Sentry-glass-plus is more rigid comparing thermoplastic-polyurethane and polyvinyl-butyral which can transfer more shear between layers and lower the strain at the back. However, it has poor adhesion on glass proven by large peeling off of the glass fragments after gas gun experiments. Comparing with polyvinyl-butyral, thermoplastic-polyurethane has good adhesive properties with Sentry-glass-plus and glass. A multi-layered interlayer system using structural Sentry-glass-plus and adhesive thermoplastic-polyurethane as interlayers can significantly reduce the strain during impact and prevent glass fragments from flying off at high velocity which is favourable in real scenarios (e.g. bird-strike).

Acknowledgements

I would like to thank my supervisor Professor John Dear, Dr. Iman Mohagheghian and Professor Tony Kinloch for their valuable support and advice throughout the project.

Professor Yue Yan and his team, from Beijing Institute for Aeronautical Materials (BIAM - AVIC), are also greatly appreciated for their valuable support and guidance on the project and also for providing all the expensive test materials.

I would like to thank my friends, colleagues for their valuable support and encouragement, without all their helps, I won't be able to finish this project.

I thank my parents and family for all their encouragement, support and inspiration; without it I would surely not be writing this today.

Finally, this work has been financed by BIAM AVIC and I would like to express my gratitude for this financial support.

Table of Contents

List of Tables

List of Figures

Nomenclature

b	Characteristic size of square glass sheet
b’	Dimension of the square shape glass sheet
h	Thickness of the glass sheet
m	Weibull factor/modulus
r_l	Radius of the loading ring
r_s	Radius of the supporting ring
tanδ	Tangent of the phase angle
γ	Shear strain
ϑ	Poisson ratio of glass
τ	Shear stress
σ_{rad}	Radial stress
σ_T	Tangential stress
σ	Applied stress
σ_0	Threshold failure stress
ε_{rad}	Strain in radial direction
ε_T	Strain in tangential direction
ε_f	Failure strain
ε_{gauge},	Strain obtained by strain gauge
E	Tension quantity
E’	In phase stress – strain tension quantity
E’’	Out of phase stress – strain tension quantity
E_y	Young’s modulus
G	Shear modulus or quantity
G’	In phase stress – strain shear quantity
G’’	Iut of phase stress – strain shear quantity
P	Applied load
P_f	Failure probability at applied stress
T_{gs}	Glass transition temperature via loss modulus
T_{gs}	Glass transition temperature via storage modulus

Acronyms and abbreviations

ASTM	American Society for Testing and Materials
ALE	Arbitrary Lagrangian Eulerian
BIAM	Beijing Institute of Aeronautical Materials
BSI	British Standards Institution
CG	Chemically strengthened glass
DIC	Digital image correlation
DMA	Dynamic mechanical analysis
EVA	Ethylene-vinyl acetate
FAR	Federal Aviation Regulations
GF	Gauge factor
LG	Lamination of glass and polymer
PMMA	Poly methyl methacrylate
PVB	Polyvinyl Butyral
SGP	Sentry glass plus
SPH	Smoothed Particle Hydrodynamics
SOFCs	Solid oxide fuel cells
TG	Thermally strengthened glass
TPU	Thermoplastic polyurethane

1. Introduction

This chapter describes the importance of structural performance against bird strike. Basic concepts and problems concerned with windshield design are presented and the aim and objectives for this project are outlined. The thesis structure and contents of each chapter are briefed.

1.1. Lamination structures used for aircraft

The development of aeronautic technology has allowed humans to explore the sky freely and made travelling cross long distances easier, faster and more frequently. Whilst passengers may enjoy their journey during flights, the safety of aircraft is always primary concerns. Aircraft safety design needs to consider various potential risks, such as lighting shock, hail impact (Figure 1, left), bird strike (Figure 1, right) and different types of extreme weather circumstances. Bird strike, which common impact incidents on ground or low altitude and can take place at any parts of the aircrafts, is a significant threat, presenting a directly risk to the pilots' life and consequently threatening the safety of the aircraft passengers [1,2]. Depending on the size of the aircraft, according to CS 23 and CS 25 certifications, respectively, at cruise speed, the windshield could withstand an impact by either a 0.9 kg and 1.8 kg bird without penetration [3].

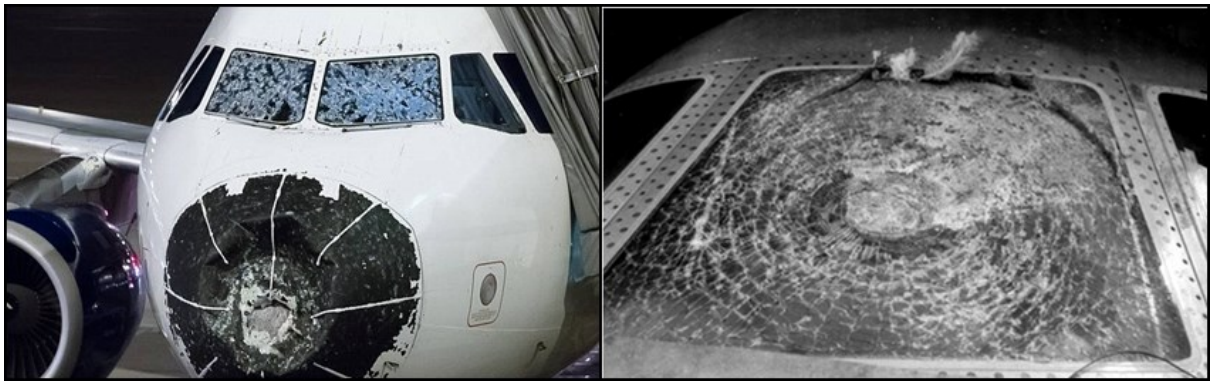

Figure 1-1. Illustration of damage on an aircraft's windshield. Left: Broken windshield and nose on Airbus A320 after encountering hail storm and landing in Denver, USA on 9 August, 2015 [4]. Right: Damage from a bird strike test by the Flight Impact Simulator facility, National Research Council of Canada [5].

Laminates for glass and polymer (laminated glass or LG) are manufactured in an autoclave by bonding two or more pieces of glass ply with heat processing and high pressure, using adhesive polymer to obtain transparent interlayers. After the first laminated glass was invented and patented by Edouard Benedictus in 1909 [6], the PPG Industries, Inc (a major windshield manufactory company in the world) introduced the first laminated aircraft glass in the late 1920s [7]. Since then, laminated structures have become the main options for window design in a majority of aircraft. Mainstream selections of glass and polymer used in the laminate design include toughened glass, Polyvinyl Butyral (PVB) and Thermoplastic polyurethane (TPU) [8–13]. The toughened glasses are Herculite® I & II thermally tempered soda lime and chemically strengthened glass respectively; specially, graded PVB and TPU are used for polymer interlayering in conjunction with the heating de-icing and de-fogging system on the windshield.

1.2.Laminated glass under impact loading

Statistically, the location and percentage of bird strike damages largely depends on the geographic area and bird distributions. Figure 2 shows the distribution of major bird strikes according to their location on the aircraft. The nose and windshield take approximately one fifth of the impact whereby the windshield alone occupies thirteen percent and takes a large portion of the impacts [1]. Although bird strike is relatively common, and has become less harzardous at this stage of aviation technology, catastrophic failure and accidents do happens,

affecting financial stability as well as safety. A thorough understanding and careful design is still needed to improve the mechanical performance of windshield structure so they can withstand higher standards in extreme or unexpected conditions.

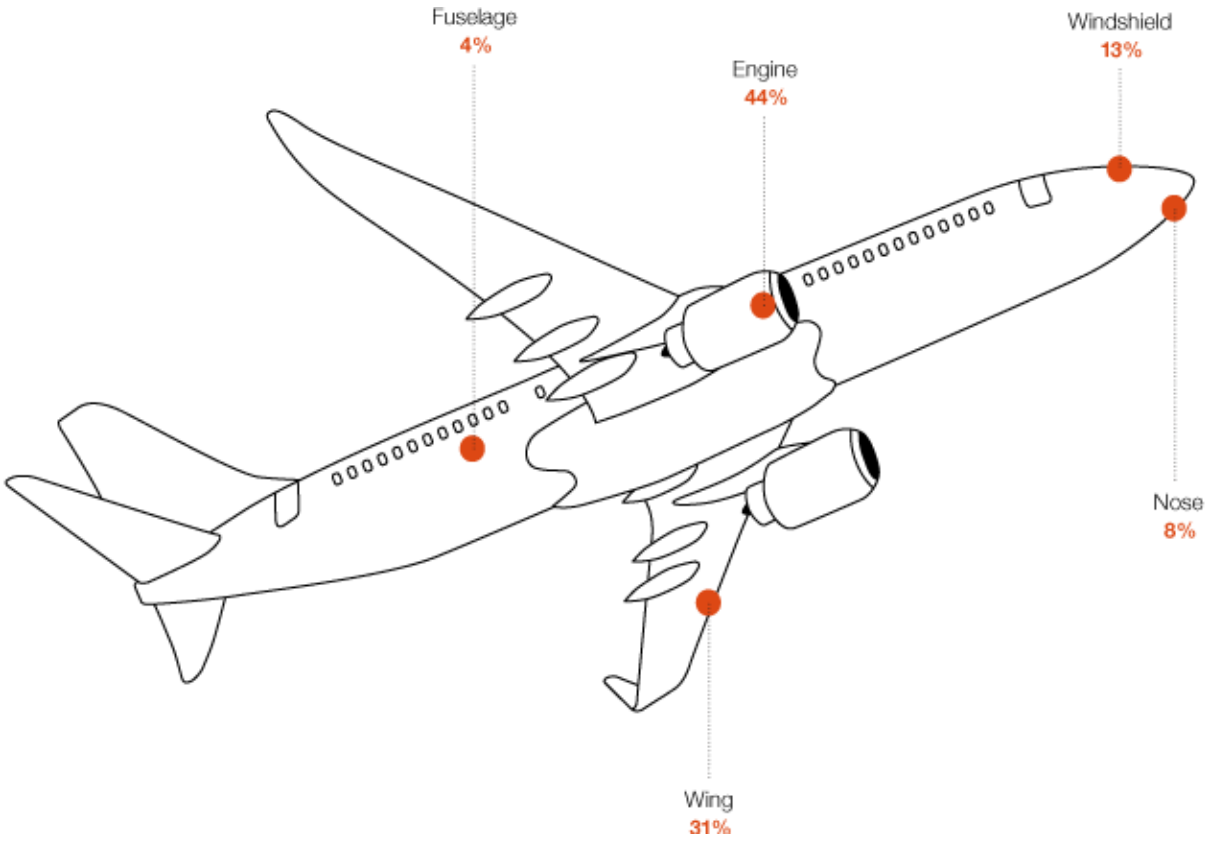

Figure 1-2. Probability of bird strike damages on aircraft based on location [1].

Transparent monolithic glass or poly methyl methacrylate (PMMA) was previously used as a windshield material, yet the chance of breaking these types of windshield was high. Monolithic glass with different strengthening methods improves the structural behaviour of the windshield and reduce the time dependence of its strength, but the brittleness of the monolithic glass restricts bending absorption from the impact energy. Similar problem have been found in rigid polymer, whereby post breakage fragmentation and the detachment of the fragments still cause great danger to pilots and aircraft. In modern aircraft design, one solution to such problems is to use a laminated system of glasses and polymers. According to the design and construction standards of Federal Aviation Regulations (FAR), transport category aircraft must have a mean to minimise danger to pilots from flying windshield fragments[14]. Applying a laminated glass structure not only overcomes the drawbacks of monolithic glass by improving post-impact and -breakage behaviours, it also allows the entire structure to absorb impact energy with

substantial safety even after the glass is shattered. Based on these merits, lamination has frequently been used in building construction, automotive and aeronautic constructions for applications requiring high resistance to failure and better performance with security features, such as bullet-proofing, blast protection and structural components [15–17]. Laminated glass was invented by French artist and chemist, Édouard Bénédictus in 1903 [6], and has long been used in aircraft. However, as aircraft technology continues to develope, faster speed increase the potential for damage, in which requires further improvement to accomplish lighter and higher impact resistance in windshields which is a goal of this research into the mechanical performance of laminated glasses used in aircraft.

1.3.Laminated glass structure for windshields

Laminated glass is a composite material comprised of monolithic glass plies and different types of polymer interlayers. Monolithic glass used for windshields is normally toughened glass, which can be strengthened either thermally or chemically. Depending on rigidity and thickness, polymer interlayers can be assigned to functional or structural uses: for de-icing and de-fogging; a thick and rigid polymer acts as an impact resisting layer to help transfer shear; while an adhesive thin polymer layer is used to join glass and other poor-glass-adhesive but useful polymer layers. Combinations of different interlayers with glass will result in different windshield strengths in impact performance.

Nowadays, most aircraft windshields from major suppliers such as Boeing and Airbus have introduced new techniques for innovative design and higher impact tolerance shown in Figure 1-3, such as multi structural polymer interlayering and a sacrificial impact front layer. Laminated windshields are typically comprised of five layers: three layers of monolithic strengthened glass plies plus two layers of multifunctional polymer interlayers. Based on the research literature [10,12], monolithic glass plies for heating and defogging facilities are arranged in such order: 1) a thin glass ply at the impacting outer face, which also takes on structural functions by dissipating energy from breakage/fracture (i.e., a sacrificial layer); 2) then a thick strengthened monolithic glass ply follows a polymer interlayer, which is the main structural monolithic glass component that protects the whole from the majority of impact energy; 3) lastly, a thinner or equivalent structural monolithic glass ply is used at the backing layer facing the cockpit to guarantee safety from impact damage.

The polymer interlayer structure has been innovated as well. Between the first and middle monolithic glass plies, the multi-polymer interlayer concept is introduced to provide good adhesion properties and possible shear force transfer between monolithic glass layers.

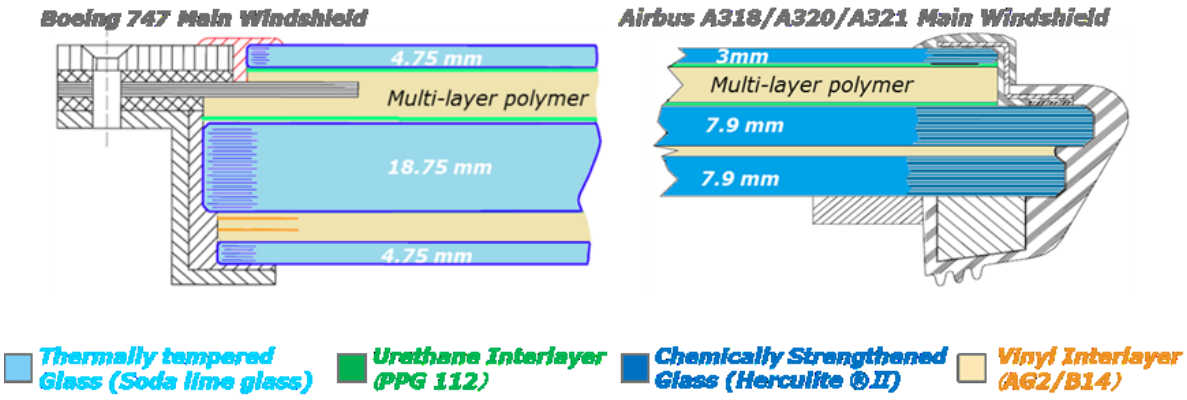

Figure 1-3. Classic aircraft windshield structural design configuration from Boeing and Airbus [10,12].

1.4.Aims and thesis outline

The selection of monolithic glass plies, interlayers and their corresponding thicknesses varies according to structurel designs, applications and purposes.

Designing a lighter and safer windshield, which remains a challenge, is the ultimate target for this study. The ultimate service condition would include pressurisation and functional coatings and 5 layer systems under high speeds and working environmental conditions. Based on observations of the current serving model among major manufacturers, the structure of laminate is affected by the thickness of the monolithic glass layer, the adhesion properties between glass and polymer, as well as interlayer polymers and the order of layering. Some of these aspects have been considered in this study, with special plans and tests simulating high speed impacts from bird strike.

To fully understand the mechanical performance of different laminated windshield structures used in major aircraft, the study was broken down into branches for each element of the laminate as well as the integrity of the structural performance. This helped to make the work manageable and offered a better understanding of the lamination design. Seven laminated glass structures (cases) were designed by methodology, with a single variable changed in each configuration in order to assess the influence of the following factors:

a. Effect of polymer interlayer thickness
b. Effect of glass types
c. Effect of polymer interlayer types
d. Effect of multi layered interlayer

Figure 1- is a detailed diagram illustrating different cases used for the experiment design, whereby each case number represents a different combination structure for laminated glass. Due to the capacity limit of the equipments, the lamination was confined to only two layers of monolithic glass.

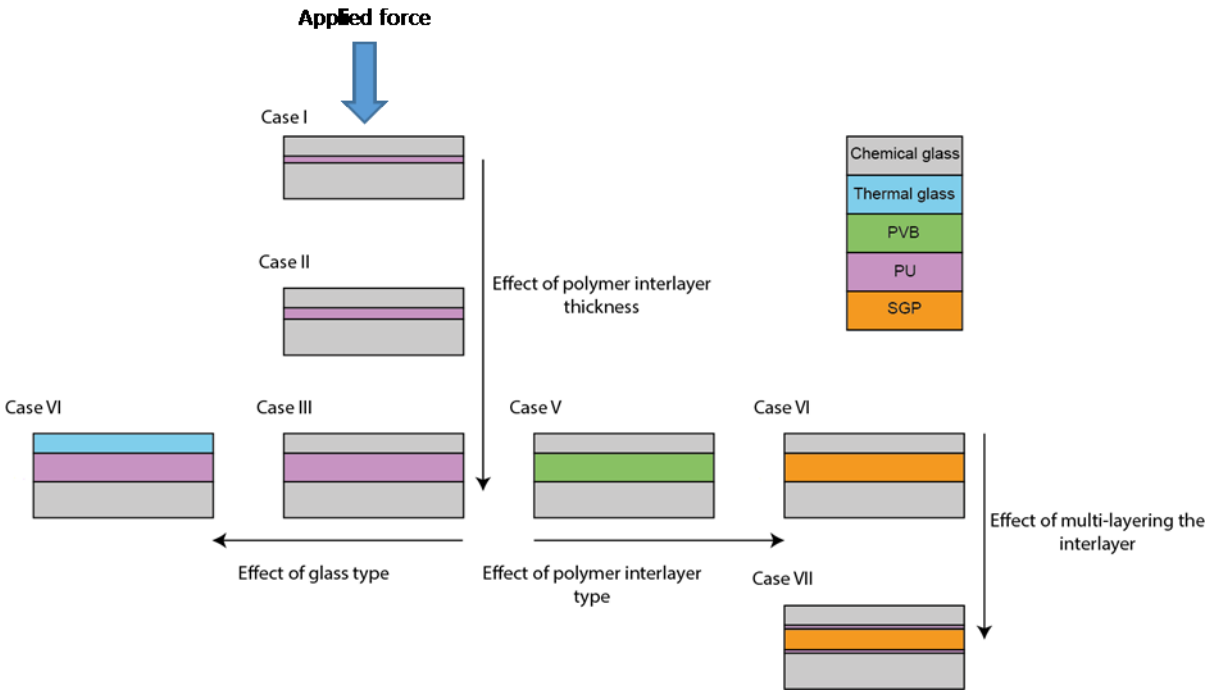

Figure 1-4. Laminated glass structural design and parameter controls layout.

Case 1 to case 3 investigate the effect of polymer interlayer thickness by varying polymer interlayer thickness while keeping all the other conditions at the same. Case 3 and case 4 investigate the effect of glass type by varying the treatment conditions of impacting face glass plies (change from chemical strengthened glass to thermally toughened glass) while keeping all other conditions the same. Case 3, case 5 and case 6 investigate different types of polymer interlayers by changing the interlayer combination while using the same monolithic glass and geometry (Case 5 used sentry glass plus (SGP) which is a rigid type of PVB, Case 6 used ordinary PVB and Case 3 used TPU). Cases 6 and 7 investigate the effects of multi interlayer structuring by changing the single polymer interlayer to a multi-layered interlayer. Laminate

configurations were tested under various impact methods. In the following chapters, all the cases will be using shortcut of capital ‘C’ with case number, e.g. ‘C1’ represents ‘case 1’.

An understanding of mechanical behaviour under real speed impact is essential to determine the appropriate structural design for various laminations, yet this has to be divided into many steps in order to understand all the aspects of the lamination, including different test speed ranges. Various glass testing methods have been undertaken by two major available test standard resources: the British Standards Institution (BSI) and the American Society for Testing and Materials (ASTM). Possible testing methods include the ball drop and axe on glass [18,19], the pendulum test [20], the ballistic or blast test for glass [21,22], the ring on ring or ball on ring [23,24], the three points and four points bending tests [25,26] for monolithic glass, the peeling test for adhesion properties between polymer and glass after lamination [27], and the thermal shock test for sudden temperature changes [28,29]. Choosing the appropriate test methods was critical to gleaning the mechanical behaviours involved in the structural performance of laminated glass, and a series of experimental design and testing methods were approached for this study to achieve a better and systematic understanding of each laminated windshield component. The structure for windshield design was tested at different velocities, ranging from using light gas gun (ballistic) to simulate dynamic speed similar to aircraft cruising speeds, to the implementation of the drop weight tower for studies of lower speed impacts. Some of the tests were performed with the assistant of optical measuring techniques and traditional strain gauges for validation purposes and to obtain a full range of data. A quasi static test was performed using the ring on ring test method to investigate the maximum flexural bending strength of the glass components and monolithic glass, and tensile data of selected polymer materials were tested at different strain ranges to observe mechanical behaviours under working conditions. In this study, the standards will be mainly using BSI, nevertheless, both BSI and ASTM are similar in theory.

This thesis is divided into three major chapters to illustrate mechanical and structural performance of monolithic and laminated glasses in different test ranges in order to provide a holistic view of the performance at different velocity ranges. Chapter 2 introduces the related literature reviewed for the study. Chapter 3 describes experimental materials used in this study. Chapter 4 examines the mechanical performance of monolithic glass and laminated glass at quasi static level. Chapter 5 investigates the mechanical performance of monolithic glass and laminated glass at low velocities with a drop weight machine by soft rubber impact (<10 m s^{-}

[1]), while Chapter 6 studies the same at high velocities (>100 m s^{-1}) with a gas gun machine by soft rubber projectile to simulate bird strike scenarios. All three chapters are currently in the process of publication in academic journals, and the content presented in this thesis also exists as drafts prepared for publication. Chapter 7 is the conclusion and Chapter 8 is the future work.

2. Literature review

Aspects related to the structural performance of laminated glass and basic knowledge of mechanical mechanics are described here. Essential knowledge is necessary to guide efforts to interpret and understand the structural performance of laminated glass under different velocity ranges.

2.1.Structural performance of laminated glass at quasi static level

The development of lightweight transparent structures used for aircraft has made travelling long distances easier, faster and more frequent; however, while in the air, aircraft can incur great damage, with risks to structural performance in the air. Studies of such damage indicate that approximately 13% of threats occur on the windshield [1], which has drawn great attention towards the need to develop of thinner and more lightweight transparent structures for aircraft windshields. The following paragraphs review properties of monolithic glass and laminated glass related to the structural performance of aircraft windshields.

Previous study of flexural bending strength measurement

Conventionally, the analytical methods used to assess flexural bending strength are derived from the applied load of the experiment. For normal applications, whereby the central deflection of the glass plate is smaller than half of the specimen's thickness, the calculation and procedure are well established in standards from both ASTM and BSI [23,24]. For the situation of large deflections, as can occur with chemically toughened glass, there have been many attempts at interpretation, either through nonlinear analytical solutions considering membrane force or based on finite element analysis [30–33].

Timoshenko and colleagues published a nonlinear theory of plate bending considering membrane stress [30]. Kao and colleagues studied large deflection (3 to 4.5 times the specimen's thickness) using chemically ion exchanged strengthened glass in ring on ring (or point on ring) compression configuration [31]. Their research resulted in the development of a mathematical model based on the nonlinear relaxation technique by solving a set of two nonlinear algebraic finite equations governing plate bending and accounting for membrane stress. The model worked well, affirming experimental results and showing a significant stress

concentration in cases of large central deflection [31]. However, referencing standards from both ASTM and BSI [23,24], the analysis by Kao and colleagues did not consider frictions with regard to all contacts between specimen and metallic compression rig, and its axisymmetric assumption was limited by special specimen/ring geometries [31]. As a result, the analysis derived by Kao and colleagues has certain limitations, which can lead to inaccuracies in measurements of stress response and differences from actual experimental output.

Finite element analysis is a better method to interpret large deflection with consideration of membrane stress. Wilcox and colleagues developed both a numerical and an analytical model based on ring on ring configuration for thin glass [32]. Their numerical model was based on shell elements and correlated well with the result from their unpublished analytical solution. Pećanac and colleagues numerically studied ~310 μm multi layered thin film of solid oxide fuel cells (SOFCs) of large deflection using 2D axis symmetry [33], and their result is comparable with linear elastic bending analytical solution rearranged for bi layered material. A non-linear bending result was observed from the finite element method for both convex and concave shapes of material. However, the whole numerical model depends on material geometry and conditions.

In addition to the above methods, a more direct and straightforward method has been applied to measure flexural bending strength via related measurements of maximum strain before the specimen's failure. This method has not often been tested on glass due to the difficulty of measurement and indirect measurement using strain acquisition equipment [34,35]. Bennison and colleagues calculated flexural bending stress based on strain measurement, using strain gauge to validate numerical simulation results on float glass fabricated into laminated glass [34]. The validity of the method was demonstrated by the closeness of the results achieved for strain gauge calculated bending strength and FEA bending strength. Vepakomma and colleagues observed a great deal of deflection during investigations of the flexural bending strength of LCD panels (consisting of two pieces of glass with liquid crystal and spacers between them) using strain measurement via ring on ring compression [35]. The type of glass used in this case is not specified, yet the experimental results correlated well with expectations from numerical calculations. However, this method also has limitations, as strain gauge only measures a single data point, and the measurement depends on soldering preparation and environmental conditions such as humidity and temperature. Moreover, wiring is geometrically dependant on fixture design, and it may be impossible to place gauges on objects with rough surface conditions or inconvenient shapes. A solution for this problem is 3D digital image

correlation (DIC), which offers a full specimen's geometric view from the testing object's supporting surface. In general, the DIC technique uses a series of digital images that are captured continuously from monitoring the surface throughout the compression testing process. The technique allows these captured images to be divided into sub-regions of pixels known as facets, from which the inter-facet displacements can be calculated between each adjacent image.

There are no literature applying this 3D DIC monitoring method of calculating flexural bending strength for chemically strengthened glass and its laminates on ring on ring compression configuration. Related literature has mentioned the DIC technique used to locate the nucleation of brittle graphite and study the initial propagation of the fracture initiator under linear elastic bending range [36].

Previous study of structural performance of laminated glass

Although chemically strengthened monolithic glass is highly reliable during normal usage, it can still fail very quickly if subjected to extreme external loading conditions. To prevent this from happening, a solution from modern aircraft design is to use laminated glass composed of chemically strengthened glass plies. Using this combination not only overcomes the potential risks of post-breakage in monolithic glass, it allows the entire laminated structure to absorb impact energy even after the glass shatters, with substantial safety provided from the adhesion of lamination. Because of these advantages, laminated glass has been used on applications with security features that require safer and advanced performance, e.g. bullet proof, blast protection and structural components for building construction and the automotive and aeronautic industries [15–17]. The interest of this study is to focus on the structural performance of laminated glass used on aircraft.

The first laminated glass was patented by Edouard Benedictus in 1909 [6]. Since then, laminated structures have become the primary option for the design of major aircraft windows. The majority of glass and polymer used in the laminated design are strengthened glass, Polyvinyl Butyral (PVB) and Thermoplastic polyurethane (TPU). Specially graded PVB and TPU are used for the polymer interlayer in conjunction with the windshield's heating and de-ice/ de-fogging system. One issue regarding some laminated structures using strengthened glass and multi-layered polymer interlayer with different thicknesses concerns the structural performance at quasi static level.

An understanding of the structural performance of laminated glass begins with the study of structural behaviour, of which there are many researches. Hooper studied the structural behaviour of laminated glass experimentally and numerically, using annealed glass with different hardness of PVB interlayer lamination to conduct a four point bending test using strain gauge [37]. When short term load was applied, there was no interfacial slippage and the laminated glass obeyed the linear load-deflexion response, i.e., the laminated glass behaved like monolithic glass at equivalent thickness. More importantly, when sustained load was applied, laminated glass using soft PVB reacted in a manner comparable to two separate stacked glasses, yet without demonstrating the coupling effect.

The latter result was confirmed by Linden and colleagues [38], who conducted a non-destructive study on monolithic, layered, and laminated structure using PVB and anneal glass with strain gauges, concluding that the laminated glass and monolithic glass of equivalent thickness had similar mechanical strength at room temperature as well as at elevated temperatures. Vallabhan and colleagues have demonstrated a nonlinear mathematical model to determine the stresses for two annealed glass plates stacked without interlayer, and this method has been further developed to understand the behaviour of laminated glass [39]. This study also found that laminated glass had a similar maximum stress as that for monolithic glass of equivalent thickness.

Similar conclusions have been delivered by Minor and colleagues, who report the failure strengths (destructive and non-destructive) of annealed laminated glass specimens to be similar to the strength of monolithic glass of equivalent thickness [40]. These researchers also tested laminated glass with PVB and annealed glass under lateral pressure at different temperatures [41], determining that at temperatures of 49 °C or above, PVB became soft and unlikely to present flexural stiffness from the laminate, whereas at temperatures below 0 °C, the laminate exhibited similar behaviour as monolithic glass.

Such results highlight the need to focus on the influences of polymer rigidity and working temperatures. Structural performance is observed to be not only a function of polymer interlayer type, but also of loading rate and temperature. Bennison and colleagues studied fracturing in laminated glass using PVB (Butacite®) interlayer using a ball on three ball compression set up [34] , noting differences in fracture sequence depending on the combination of temperature and test loading rate. The biaxial bending stress was calculated based on direct strain measurement from strain gauge. During either high temperature (close to glass transition

temperature) and/or low loading rate conditions, the maximum biaxial stress first occurred in the upper glass ply, whereas low temperatures and/or high loading rates resulted in the maximum biaxial stress occurring first in the lower glass ply. Bennison et al also compared the structural performance of laminated glass using ordinary PVB and that using sentry glass plus (SGP), which is a modified PVB with higher glass transition temperature [42], concluding that the SGP showed much better structural performance compared to ordinary PVB.

Norville and colleagues developed a mathematical LG beam model to explain the behaviour of laminated glass [43]. The laminate used in this case was thermally tempered glass with PVB, which again decreased in strength with higher temperatures. Duser and colleagues presented a computational model by finite element simulation, taking account of nonlinear large deflection, polymer viscoelasticity and the large rigidity mismatch between polymer and glass [44]. Ivanov developed a plane finite element model for triplex laminated glass using PVB as a polymer interlayer on a simple support beam test [45], adding a differential equation of shear interaction.

Jalham and colleagues studied the effect of glass thickness and interlayer polymer thickness on the mechanical behaviour of LG [46]. PVB and ethylene-vinyl acetate (EVA) interlayer materials were compared as components of the triplex laminate structure, with the result that LG using PVB absorbed more energy than that with EVA under the same conditions, thus demonstrating a mechanical distinction between different interlayer materials in the laminate structure. Shitanokia led a study of thin glass lamination using both ordinary PVB and rigid SGP on four point bending tests [47], and in measurements of effective thickness, which refers to the shear coupling between two glass plies through the interlayer, the thickness and weight reduction of glass was more significant using SGP than with ordinary PVB laminates.

Different types of polymers have been used in laminated glass, and the structural performance of these configurations is of great concern for those invested in aircraft safety. Most studies have been conducted under rigid contact conditions, such as three/four bending or ring on ring compression. Systematic investigations of chemically strengthened glass in combination with different types of polymer have rarely attempted to make comparisons between rigid and soft contact loading conditions. Literature reviews located no studies published on rubber loading and no research concerning this type of compression using 3D DIC on chemically strengthened laminated glass from ring on ring compression. While chemically strengthened laminated glass has occasionally been examined under ring on ring compression, there is no relevant research

comparing the effects of different glass strengthening techniques on front glass ply from the laminate, and even rarer are studies of the multi-layered interlayer structure of the laminate.

In summary, the majority of researches on calculating the biaxial bending stress of monolithic glass have been carried out using either numerical simulation or the analytical application of failure load, with limited attention to the calculation method via direct strain measurement. Due to limitations associated with strain measurement, 3D DIC strain measurement is a better means to monitor a specimen's supporting side, and also has the advantage of providing the opportunity to observe strain and displacement profile during testing, yet there have been few studies published in this area. The only related literature has mentioned the DIC technique used to locate the nucleation of brittle graphite and study the initial propagation of fracturing under linear elastic bending range, with no research reporting strain measurement using 3D DIC on the supporting glass side from compression tests for chemically strengthened glass and its laminates. The majority of studies on the structural performance of laminated glass have mainly focussed on rigid loading conditions, with limited investigation of soft loading conditions like rubber loading, and systematic research is also lacking of different laminated glass configurations using PVB, TPU, SGP and combinations of multi layered structures. Therefore, this paper will focus on the direct measurement of a specimen's biaxial bending stress via direct strain measurement using 3D DIC. By applying this technique, the structural performance of chemically strengthened monolithic and laminated glass will be examined using rigid and soft loading conditions.

2.2.Low velocity impact performance

Laminating glass panels is an effective strategy for improving the safety of glass structures against impact. Due to intrinsic brittleness, monolithic glass panels can fail abruptly when subjected to impact, with many sharp and small fragments flying at high velocity and causing great danger to people around these structures. In laminated glass windows, the glass panels are adhered with polymer interlayer, which preserves the structural integrity in the case of failure in glass layers, thus reducing the risk of flying glass fragments.

Impact on laminated glass windows can be hard or soft. The term 'hard impact' refers to an impact in which the deformation of the projectile is negligible compared to that of the target. In contrast, "soft impact" occurs when the strength of the projectile is far less than that of the

target, and the projectile itself undergoes extensive deformation during its interaction with the target. The impact can be further sub-divided according to its velocity to low and high velocity. According to Backman and Goldsmith [48] , for example, the "low velocity" term refers to impacts occurring at velocities less than 25 m s^{-1}, which includes the impacts made by large, windborne objects on architectural glass windows or pedestrian head impact to car windshields. For the purposes of this study, the term "high velocity" only refers to sub-ordnance velocities (25-500 m s^{-1}) [48] , as this is a relevant velocity range for bird strike, which mostly happens during aircraft take-off and landing.

Despite detailed studies on the performance of laminated glass in cases of hard impact, far less attention has been paid toward the soft impact response of these structures. Dharani and Yu numerically investigated the impact response of laminated glass windows against impact by large soft projectiles such as collapsed trees or ceiling wood flying during hurricanes [49]. The failure modes and the location of failure initiation were examined for soft projectiles with both hemi-spherical and blunt nose shapes. In contrast to hard impact situations, in which the failure is initiated by Hertzian contact stresses, bending stresses at the opposite surface to the impact are responsible for failure with a large and soft projectile. The nose shape of the impactor also determines the failure mode; while for a soft hemi-spherical impactor, the failure occurs at the back side of the outer glass layer, the failure is initiated at the back side of the inner layer for a blunt projectile. Shetty and colleagues numerically investigated the impact response of laminated glass windows for both soft and hard impacts [50], concluding that in both cases, the thinner outer glass layer results in a better prefigure stress pattern than a thicker layer, and that a thicker interlayer generally lowers the stresses in the critical failure-prone areas.

Pacios led a study investigating the soft impact response of monolithic and laminated glass using a 50 kg twin-tire pendulum at the speed up to 4.85 m s^{-1} [51] to compare the effect of glass type, boundary conditions, thickness and dimensions of the glass plates. The height of impact was gradually increased until the sample broke. It was found that the loading is significantly influenced by the boundary condition (i.e., four pin supported compared to two sides supported). While the shape of strain and acceleration traces is strongly affected by the boundary condition, increasing the height only increases the level of strain or force, while giving similar shape and contact time.

Pedestrian head impact on the car windshield can also be considered as a form of low velocity soft impact. Normally, laminated glass windows are tested with a headform consisting of a

hollow aluminum sphere with a rubber [52]or PVC skin [53]. Zhao et al. [54] numerically studied the response of laminated glass against pedestrian head impact, arguing that while the thickness of inner glass layer (non-impacted side) is an important design parameter, determining the impact resistance of the structure, the thickness of outer glass layer (impacted side) and PVB interlayer has no significant effect on the impact resistance.

2.3.High velocity impact performance

Bird strike imposes great safety concerns in the aviation industry, and an increasing number of bird strike accidents has spurred greater efforts at designing new aircraft with more impact resistant components. The number of wildlife strikes on the civil aircrafts in the United States, of which 97% are by birds, has increased 6.1 times in 2013 compared to 1990, with deadly results: 243 aircrafts have been destroyed and 255 people killed globally since 1988 [55].

Frontal facing components of aircraft, such as windshields, nose cones, wings and engine blades are all vulnerable to bird strike during flights, especially when approaching, descending or taking off [56]. In general, engine ingestion has been recognised as a major threat for transport and executive jets, accounting for 77% of all accidents, whereas windshield impacts are only associated with 10 percent of accidents. Fifty-two percent of fatal accidents, however, have occurred on smaller aircrafts. These have largely been caused by bird strike on windshields [57] , which is the main safety concern of this study. Similar bird strike figures have been reported in [58] : of the 51 fatal airplane accidents occurring between 1962 to 2009, over fifty percent (n=27) occurred on the windshield.

Depending on the type of aircraft and the structure of its windshield, different materials are possible candidates in monolithic or laminated formats, including thermally and chemically toughened glass, polycarbonate and cast and stretch acrylic. In the case of modern passenger aircrafts, windshields have a very complex structural design consisting of several layers of glass and polymer interlayer.

Despite testing requirements for new windshields, there are very few published experimental studies on the performance of laminated glass windows, particularly in cases of bird strike, which is due either to the high cost of full scale tests, or more likely, to the confidentially of the results. Doubrava and Strnad investigated the performance of laminated glass windows

with thicknesses of 14, 18 and 20 mm against impact by a 1.81 kg bird at the velocity range from 300-450 km h^{-1} (83-125 m s^{-1}) [59]. The details of the laminated configuration are not specified, but the velocity at which the failure occurred indicates a linear trend with the thickness of the windshield. Kangas and Pigman used bird impact at velocities up to 725 km h^{-1} (208 m s^{-1}) to conduct impact tests on various windshield materials and construction types [60]. Their study suggests that the primary factor influencing the impact strength of laminated glass window is the thickness of the plastic interlayer. Different methods of installation of the windshield to the cockpit were also investigated and shown to have a strong effect on the impact strength of the windshield [60].

Due to high cost of running full scale experimental investigations, many researches have tried using numerical methods to study the effects of impact, such as the finite element [61–66]. Salehi and colleagues [61] investigated the response of various aircraft bubble windows using three different numerical methods, namely Lagrangian, Arbitrary Lagrangian Eulerian (ALE) and Smoothed Particle Hydrodynamics (SPH). Single layer stretched acrylic, multi-walled stretch acrylic, laminated acrylic with Poly Vinyl Bromides (PVB) and Polyurethane (PU) were tested, and the laminate with the PU interlayer was shown to be able to withstand the bird strike according to CS25 certification [3]. Dar and colleagues [63] studied the response of canopy made of monolithic PMMA, investigating parameters such as mass, shape and velocity of the bird, as well as angle and location of the impact. Wang and colleagues [64] also tested the response of PMMA canopy, considering the influence of environmental temperature, impact location and velocity.

There are fewer numerical studies available on laminated glass windshields [65,66]. Grimaldi and colleagues used the SPH method to parametrically describe the response of a laminated glass window consisting of three layers of glass and two layers of PVB [65]. They studied the effect of target geometry, impact angle and plate curvature on the response of the windshield against bird strike, with the impact angle found to have the strongest influence on performance. Changing the thickness ratio of glass to polymer from 1 to 2 reduced the maximum absorbed energy in the plate by 20-30%, yet a further increase of the ratio to 1:3 was found to have no significant effect. Hedayati and colleagues [66] also used the SPH method to determine the best material for a helicopter windshield according to CS 29, concluding that the laminated glass with PVB interlayer performs best.

2.4. Hydrodynamic loading

Bird impact at high velocities can be considered as a "soft body impact". As mentioned above, soft body impact refers to an impact in which the strength of the projectile is much lower than that of the target, and consequently the projectile undergoes extensive deformation. The loading imposed on the target is very different from a hard impact, in which the extent of deformation from the projectile is negligible compared to the target and which can be well described by hydrodynamic theory, in which the loading mainly depends on the density and velocity of the projectile, and projectile strength and viscosity are neglected [67]. According to [67,68] bird impact loading on a rigid target can be divided into two states: i) one in which the intensity of loading is high but the duration is very short (transient state); and ii) and one of longer duration but less intensity (steady state).

The loading can also be affected by the response of the target, as there is a close relationship between the two. Factors such as shock impedance, compliance and deformability of the target can significantly affect all aspects of the loading, including peak force and pressure, rise time, magnitude of impulse and duration of decay and steady state process [69]. The response of the target can be very different in various stages of the loading. In the transient stage, which lasts only few microseconds, depending on the material and diameter of the projectile [67], the response is dominated by high intensity waves, the propagation of which can be very complex, especially in windshields made of laminated glass, where the structure can consist of several layers of material with different acoustic impedances. The duration of the steady state stage, which can be approximated by the time the projectile needs to travel over its length, is normally long enough for the whole target to respond.

2.5. Conclusion

A significant amount of research concerning the structural performance of laminated glass at different velocities is of interest to this study. As glass has been developed in more advanced formats and its mechanical performance has improved, researchers have explored more accurate means of measuring flexural bending stress both analytically and numerically. For this study, due to the complexities hindering analytical research and the technical limitations of numerical simulation, a more direct and effect method of measurement and calculation has

been developed to work out maximum flexural bending stress for monolithic glass using the 3D DIC technique.

The literature shows that there have been many researches on structural performance at quasi static and low velocity conditions using rigid impactors, yet more rare are studies of soft rubber contact performance, indicating an area in need of more scholarly attention. Also, due to various reasons described above, laminated glass impact tests using soft projectile at high velocities has been studied numerically, but there has been limited systematic study of different laminated structures at this point.

3. Experimental materials

In this chapter, experimental materials including glass and polymer were introduced. These materials were designed and laminated into different cases/configurations to help to understand the structural performance of laminated glass systems.

3.1. Types of glass and polymer used in different laminated glass cases

The chemically toughened monolithic glass plates used in this study were manufactured using alumina silicate float glasses that had been initially edge smoothed and then soaked in potassium salt solution for ion exchange at 420˚C for 5 hours at the Beijing Institute of Aeronautical Materials (BIAM). Monolithic glass was tested at a thickness of 2.2 mm, 4 mm and 6 mm to compare its linear elasticity and large deflection phenomena.

Basically, the laminated glass used in this study consisted of two plies of strengthened glass and one interlayer of polymer, which were laminated by autoclave from research sponsor BIAM. Glass plies were made of thermally and chemically strengthened alumina silicate glass. Alumina silicate float glasses were initially edge smoothed, and then chemically strengthened by ion exchange via soaking in potassium salt solution for 5 hours at 420˚C, which generated compressive layers of 38 μm depth and 740 MPa mechanical strength at two free surfaces from the glass, and the figures were provided by sponsor BIAM. Thermally strengthened glasses were half strengthened due to the thickness versus pressure limitation, as requested by sponsor BIAM. The 2.2 mm thick thermally strengthened glass ply used in this paper can only afford half of the power of strengthening treatment. For purposes of consistency, all of the glass was initially cleaned, and the tin side was used for lamination. The polymer was selected from those available in the market that fitted the purpose of this study. Three types of the polymer were chosen:

- Thermoplastic Polyurethane (TPU) from PE499 KRYSTALFEX ®, Huntsman,
- Polyvinyl Butyral (PVB) from Butacite ®, DuPont,
- Modified PVB from Sentry Glass Plus (SGP) ®, DuPont.

The quasi-static uni-axial tensile behaviour of these three polymer interlayers is shown in **Figure 3-1**. At room temperature, PVB and TPU are in the rubbery state while the SGP shows a more glassy response. In the literature, the glass transition temperature of three different polymers are TPU at -49 °C [70], PVB at 20 deg glass [71] and SGP at 55 deg glass [42].

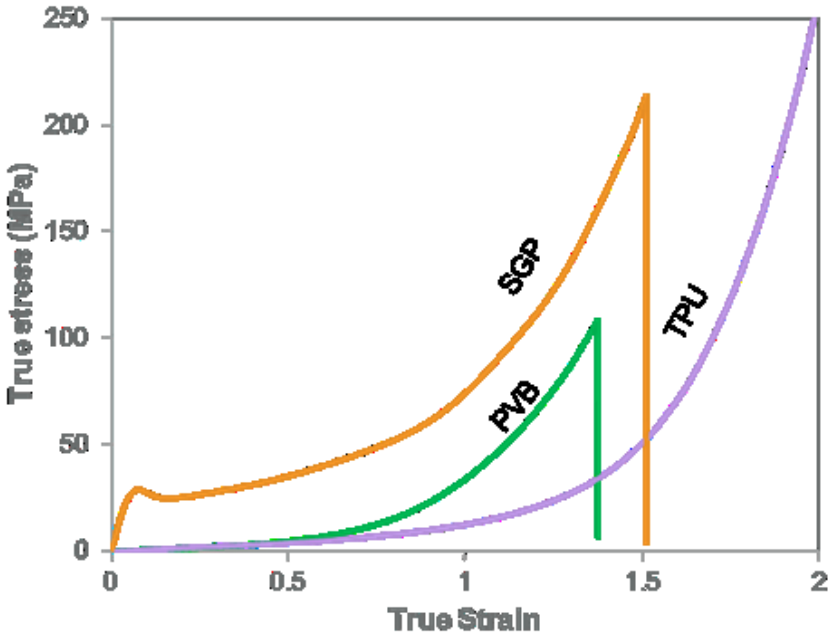

Figure 3-1. Quasi-static uni-axial tensile response of three types of polymer interlayer used in this study, the speed was 5 mm/min and performed at a temperature of 22°C ± 2°C and relative humidity of 50% ± 2% under a laboratory level closed loop controller.

In total, eight different configurations were used for laminated glass testing and three different thickness of monolithic glass was chosen. The details of each test specimen configuration can be found in **Table 3-1**. For laminated glass configurations, C1 to C7, two layers of toughened glass with the thickness of 2.2 and 4.0 mm were used (the thinner glass layer always faced the impactor). For laminated glasses, C3 was treated as a reference case, and the effects of different design parameters, e.g. polymer type and thickness, glass type and the effect of multi-layering the interlayer, are compared against it.

The effect of polymer interlayer thickness on the structural performance was investigated through C1 to C3 and C3H. The thickness of the polymer interlayer (TPU), was changed from 0.76 mm to 3.18 mm (C1, C2 and C3) in quasi static compression and drop weight low velocity experiments and 1.27 mm to 5.09 mm (C2, C3 and C3H) in high velocity gas gun experiments, while other parameters including glass type and thickness and polymer type remained unchanged. Due to limitations in the conventional polymer interlayer thickness available in the

market, two or more layers of polymer were laminated together to achieve thicker interlayers. The effect of the type of glass frontal layer, which is 2.2 mm thick glass, is investigated to compare the performance of C3 with C4, which has a thermally rather than chemically toughened glass for its frontal layer. In both cases, a 3.18 mm TPU interlayer was used. The type of polymer interlayer was changed in C5 and C6 by using SGP and PVB respectively. In both cases, 3.04 mm thicknesses of polymer layer were used, which is close to the thickness of the reference case (i.e., C3 has slightly thicker layer of 3.18 mm, which is the only available closest thickness in the market). The effect of multi-layering the polymer interlayer was explored in C7 by using a 2.28 mm SGP layer sandwiched between two thin layers of TPU of 0.38 mm thickness each, resulting in a total interlayer thickness of 3.04 mm, similar to that of C3. Finally, a 6.0 mm thick monolithic chemically toughened glass was used in order to compare the performance of laminated glass with monolithic glass. Although the thickness of this glass plate is not exactly equal to the total thickness of glass layers used for laminated glass specimens (0.2 mm thinner), its mechanical performance will be used as a guideline for comparison with laminated glass plates. C8, C9 and C10 were chemically strengthened monolithic glass with different thickness of 6 mm, 4 mm and 2.2 mm, respectively.

Table 3-1 Summary of different laminated glass configurations.

Number	Loading glass layer	Polymer interlayer	Supporting glass layer
C1	CG, 2.2mm thickness	TPU, 0.76 mm, PE399	CG, 4.0mm thickness
C2	CG, 2.2mm thickness	TPU, 1.27 mm, PE399	CG, 4.0mm thickness
C3	CG, 2.2mm thickness	TPU, 3.18 mm, PE399	CG, 4.0mm thickness
C3H	CG, 2.2mm thickness	TPU, 5.09 mm, PE399	CG, 4.0mm thickness
C4	TG, 2.2mm thickness	TPU, 3.18 mm, PE399	CG, 4.0mm thickness
C5	CG, 2.2mm thickness	SGP, 3.04 mm, rigid type of PVB	CG, 4.0mm thickness
C6	CG, 2.2mm thickness	PVB, 3.04 mm, ordinary PVB	CG, 4.0mm thickness
C7	CG, 2.2mm thickness	Multi interlayer: 0.38mmTPU/2.28mmSGP/0.38mmTPU	CG, 4.0mm thickness
C8	Monolithic glass, 6 mm thick CG at 420° Celsius for 5 hours		
C9	Monolithic glass, 4 mm thick CG 420° Celsius for 5 hours		
C10	Monolithic glass, 2.2 mm thick CG at 420° Celsius for 5 hours		

In Chapter 4, the quasi static coaxial ring compression experiments, C1, C2, C3, C4, C5, C6, C7, C8, C9 and C10 were used. The specimens used in all tests were of a 100 x 100 mm square flat shape for both monolithic and laminated glasses.

In Chapter 5, the low velocity drop weight experiments, C1, C2, C3, C4, C5, C6, C7 and C8 were used. The specimens used in all tests were of a 100 x 100 mm square flat shape for both monolithic and laminated glasses. Five repeat tests were conducted for each configuration.

In Chapter 6, the high velocity gas gun experiments, C2, C3, C3H, C4, C5, C6, C7 and C8 were used. The laminated glass specimens used in this study were square plates with dimension of 180×180 mm.

4. Mechanical performance of monolithic and laminated glass at quasi static level

The development of chemically strengthened glass and variety of polymer interlayer types has improved the structural performance of laminated glass. A new method involving a combination of 3D DIC monitoring and strain calculation method was developed to calculate flexural bending stress, which increases the ability to study laminated glass's structural performance at quasi static level. We investigated the influence of the thickness of chemically strengthened monolithic glass on the flexural bending strength, as well as the polymer influence of thermoplastic polyurethane (TPU), polyvinyl butyral thermal (PVB), and special grade rigid PVB (sentry glass plus, SGP) used in the laminated glass system. Testing was done experimentally by following the test protocol of coaxial double ring compression with 3D DIC measurement of strain and displacement developed by the researcher.

4.1.Method

4.1.1. Ring on ring

4.1.1.1. Experimental setup

This study aimed to correlate strain profiles from the 3D DIC technique and ring on ring compression to investigate the maximum flexural bending strength of laminated glass before failure. To achieve this purpose, a fixture was designed based on the coaxial ring on ring test method in combination with the 3D DIC technique shown in **Figure 4-1**. **Figure 4-1**.a shows the actual on site experimental set up of 3D DIC kit and testing fixture. The key feature of this design is the 45° mirror used in the test, which makes is feasible for the 3D DIC to capture the specimen's supporting side strain and displacement visualisation profiles. By positioning the mirror at 45°, cameras equally record live images from the supporting surface of the specimen, with images flipped vertically, which requires indirect image processing of both calibration and test data, in contrast to the standard procedure of ordinary 3D DIC. Raw images were captured from the system, processed using image processing software to be flipped vertically and externally, and then inputted to the system again for data processing and analysis. The mirror used was a first surface reflection mirror that has been aluminised on the top surface of the flat mirror, which is the nearest position to the incident light. The benefit of using this type

of mirror is that light reflects at the mirrored surface and does not need to penetrate through glass, thus minimising light loss. Enhanced aluminium mirrors have an average of 95% reflection [72]. **Figure 4-1**.b shows a schematic drawing of the design. An open volume was created to allow this mirror to be seated underneath the hollow loading ring and reflect all the live images back to the 3D DIC system for data acquisition. Load was applied through the circular shape loading ring on the top surface of the glass plate, which rests freely on the circular shape supporting ring. There was no contact of the coaxial rings with specimen edges except at the top and bottom surfaces. A transparent polycarbonate protecting shield covered the opening loading area to prevent glass fragments from flying off after fracture, and a similar protecting shield was used to cover the observing mirror perimeter. Internal LED light was used on the two sides to enhance brightness and limit reflection from external light sources through the protecting shield. **Figure 4-1**.c shows the specimen geometry and an example of the random speckle pattern used in the tests. Two types of the loading condition were applied in the tests. One of these was the conventional coaxial ring on ring, whereby the force is applied through the loading side with 2a diameter of 18 mm, and the supporting ring has a diameter 2b of 90 mm. The other type was the rubber loading, which uses the same type of supporting ring used in the first conventional coaxial ring on ring of 90 mm. The rubber used in this case was a 60 shore silicone cord of 20 mm length and 14 mm diameter [73]. The difference between the first and second loading conditions is that the ring loading has concentrated stress distribution along the loading ring, whereas the rubber loading is more like the pressurised uniform load at the centre from the loading side. On the other hand, the rubber loading used an initial 14 mm in diameter rubber cord, which is indicated as 'A' in **Figure 4-1**.c. Once the load begins to be loaded (P) onto the rubber, it starts to deform into shape 'B', and the contacting area changes from initial area A, which has diameter of 14 mm in diameter to the expanded area B, which is kept unknown. An illustration of a random speckle pattern is shown in **Figure 4-1** as an example. The specimens used in all tests were of a 100 x 100 mm square flat shape for both monolithic and laminated glasses. For ring on ring test, there are gasket used in between rigid rings to prevent premature failure of specimen. Also, there was no lubricant used on rubber compression experiments due to potential slippage of the rubber during the experiment. One assumption made for the experiment was that there was no friction between rubber and glass specimens. The majority of the test were tested without lubricant. Tests with lubricant were left for future studies.

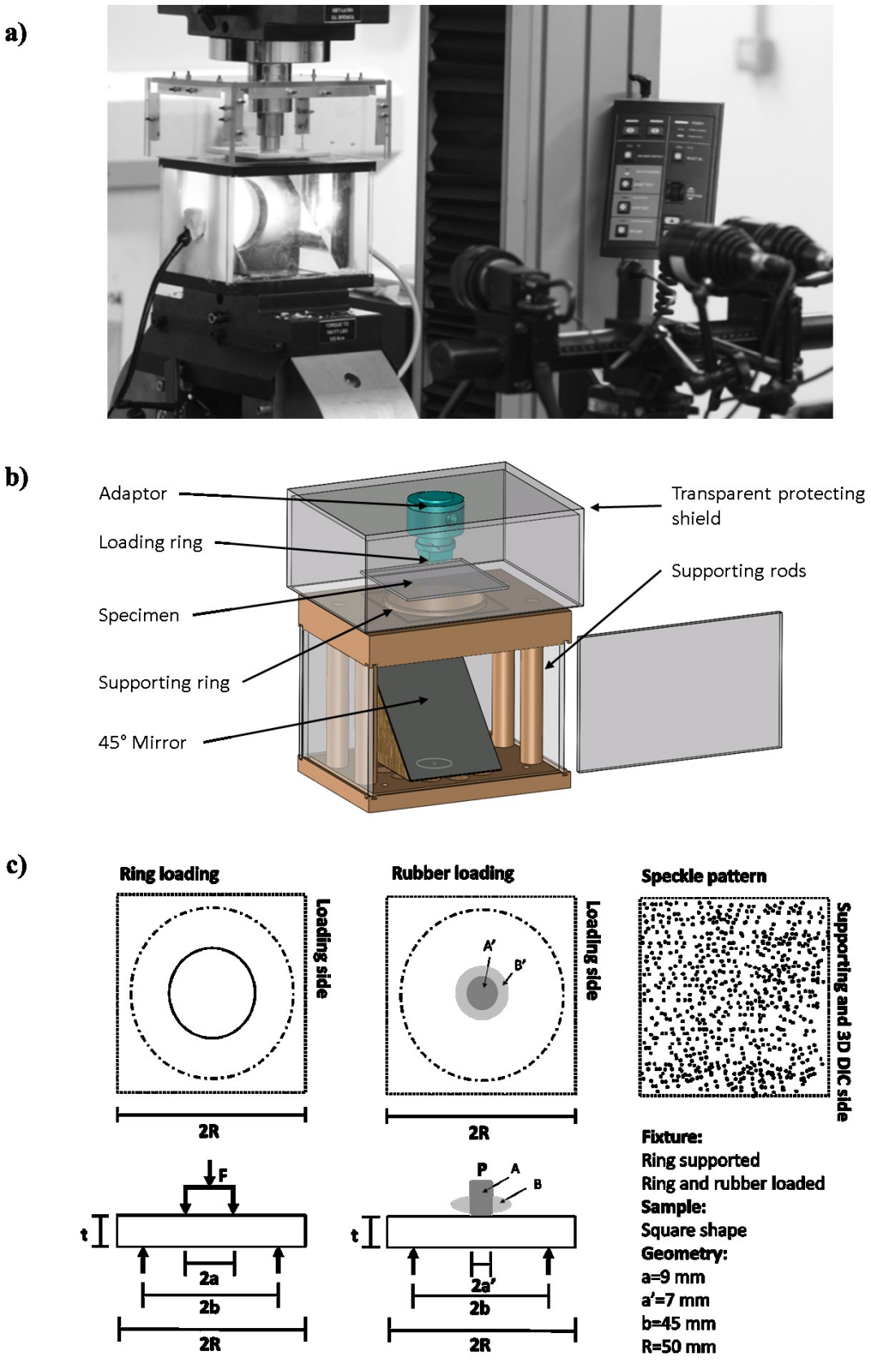

E

Figure 4-1. Experimental setup: a) ARAMIS system and testing rig; b) Specimen geometry and loading; c) Front view showing supporting ring.

All of the coaxial ring on ring tests were performed at a temperature of 22°C ± 2°C and relative humidity of 50% ± 2% under a laboratory level closed loop controller.

4.1.1.2. Linear bending theory applied by standards

Following ASTM and BSI standards under linear bending theory, equi-biaxial bending stress ($\sigma_{flexural}$) equals to radial stress (σ_{rad}) and tangential stress (σ_T) is given by:

$$\sigma_T = \sigma_{rad} = \sigma_{flexural} = \frac{3P}{2\pi h^2}\left[(1-\vartheta)\frac{r_s^2 - r_l^2}{2r_s^2}\cdot\frac{r_s^2}{b^2} + (1+\vartheta)\ln\frac{r_s}{r_l}\right] \quad \textit{Equation 4-1}$$

Where P (P=F shown in **Figure 4-1**.c) is the applied load during the experiment; h is the thickness of the glass sheet; ϑ is the Poisson ratio of glass; r_s is the radius of supporting ring (r_s=2a shown in **Figure 4-1**.c) and r_l is the radius of the loading ring (r_l=2b shown in **Figure 4-1**.c); b' is the dimension of the square shaped glass sheet and b is the characteristic size of the square glass sheet related to above equation where b=1.21b'.

4.1.1.3. Validation of 3D DIC by strain gauge

3D Digital image correlation (DIC) – Aramis

3D Digital image correlation (DIC) was used to track full view of specimen's back surface during the quasi static compression test. 3D DIC for quasi static compression tests is from GOM Ltd.; recommended speckle size is 3-5 pixels per dot and this is used for optimizing image correlation; white and black acrylic mat sprays are used to paint specimen where light and thin layer of white acrylic on transparent glass and then black speckles randomly sprayed later, for full detail of image correlation refer to Aramis manual [74]. In general, the digital image correlation technique uses a series of digital images captured continuously from the monitoring surface throughout the compression test. A high density of random speckle pattern was painted on each specimen's supporting side, allowing a correlation to be established

between the specimen's physical profile and digital calculations. The technique divides the test image into sub-region of pixels known as facets, from which the inter-facet displacements can be calculated between adjacent images. A list of evaluated displacement matrices can be differentiated to produce a full-field strain map of the monitoring surface. In the end, visualisation of the strain or displacement can be obtained on any images taken throughout the test.

Constitutive equation for stress strain material behavior

A general Hooke's law in 2D was used to work out the strain to stress relationship for biaxial bending stress. Glass is a homogeneous isotropic material and behaves like a linear elastic with large deflection in chemically strengthened glass scenarios. By considering tensile stress only in biaxial direction, radial stress (σ_{rad}), tangential stress (σ_T) and shear stress (τ) are given by Hooke's matrix:

$$\begin{Bmatrix} \sigma_{rad} \\ \sigma_T \\ \tau \end{Bmatrix} = \begin{bmatrix} \frac{E_y}{(1-\vartheta^2)} & \frac{\vartheta \cdot E_y}{(1-\vartheta^2)} & 0 \\ \frac{\vartheta \cdot E_y}{(1-\vartheta^2)} & \frac{E_y}{(1-\vartheta^2)} & 0 \\ 0 & 0 & G \end{bmatrix} \begin{Bmatrix} \varepsilon_{rad} \\ \varepsilon_T \\ \gamma \end{Bmatrix} \qquad \textbf{Equation 4-2}$$

where E_y denotes the Young's modulus of glass (≈72 GPa); ϑ represents the Poisson ratio of glass; ε_{rad} is the strain in radial direction; ε_T is the strain in tangential direction; γ is the shear strain and G denotes the shear modulus or quantity. Rearranging the equation according to large deflection theory [30], the radial stress (σ_{rad}) and tangential stress (σ_T) are given by:

$$\sigma_{rad} = E_y \frac{(\varepsilon_{rad} + \vartheta \cdot \varepsilon_T)}{(1-\vartheta^2)} \qquad \textbf{Equation 4-3}$$

$$\sigma_T = E_y \frac{(\varepsilon_T + \vartheta \cdot \varepsilon_{rad})}{(1 - \vartheta^2)}$$ **Equation 4-4**

For equi-biaxial conditions, **Equation 4-3** equals **Equation 4-4,** and the radial strain (ε_{rad}) is the same as tangential strain (ε_T) for the failure strain (ε_f). The equi-biaxial stress or the flexural bending stress (σ_b) is given by

$$\sigma_{rad} = \sigma_T = \sigma_b = E_y \frac{\left(\varepsilon_f + \vartheta \cdot \varepsilon_f\right)}{(1 - \vartheta^2)} = \frac{E_y \varepsilon_f}{(1 + \vartheta)}$$ **Equation 4-5**

4.1.1.4. Strain acquisition

There are two ways of monitoring strain information: 3D DIC and strain gauge. **Figure 4-2** illustrates a comparison between these two methods. In **Figure 4-2**.a, by applying a mirror at 45°, a researcher can obtain both major strain and displacement profiles from the experiment after images have been processed. Strain gauge was used to validate 3D DIC strain results, and **Figure 4-2**.b shows the set-up for the strain gauge, whereby a single element FLA-2-8 foil strain gauge from Tokyo Sokki Kenkyujo Ltd. was soldered at the central point position from the back side/rear surface of the specimen. The PC-based, CompactDAQ measurement system from National Instruments Ltd. was used for the modular data logger (the gauge logger). During the compression, strain gauge soldered at the central position detected strain and recorded it in the gauge logger, from which an external PC was used to receive and process strain data.

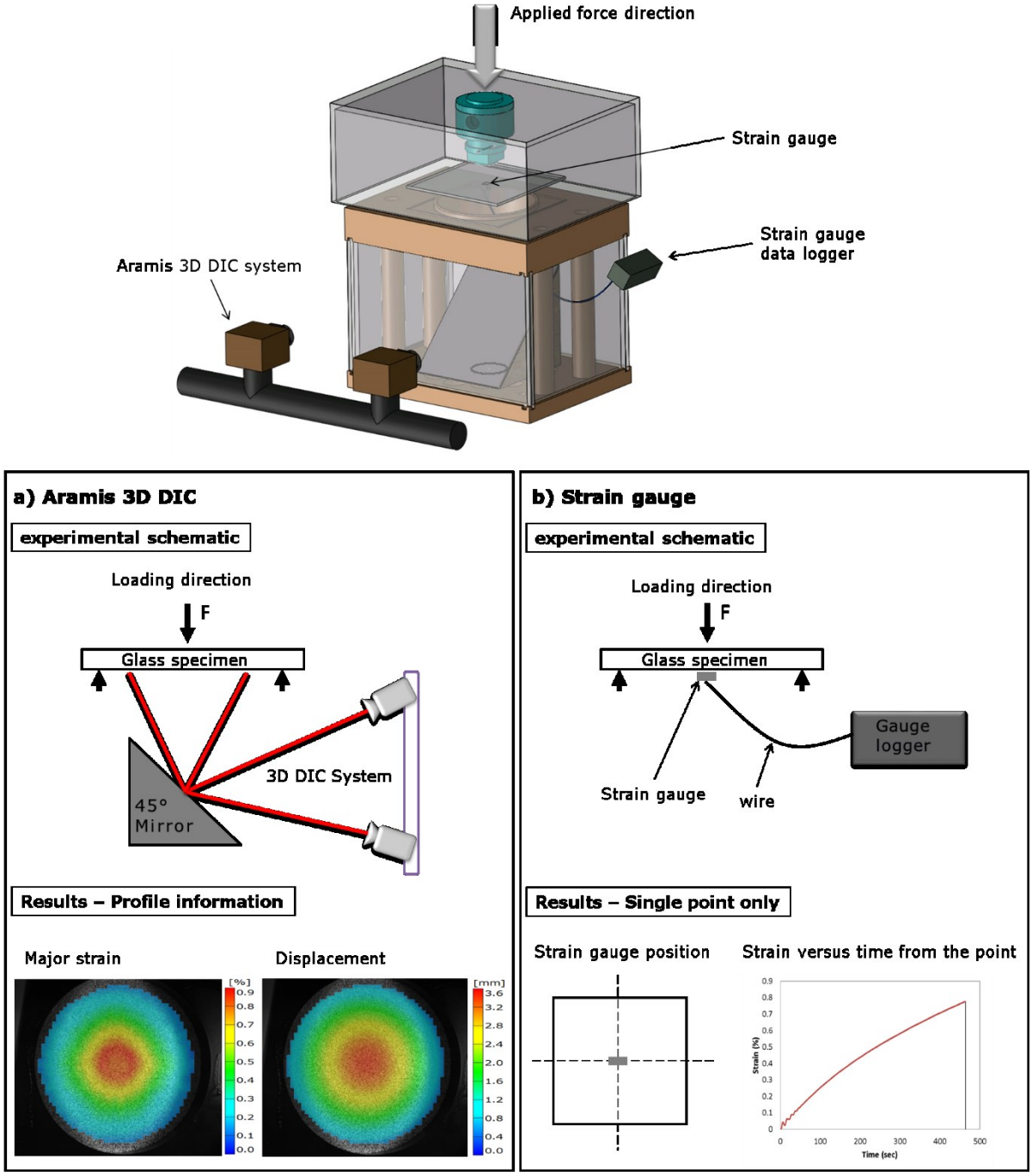

Figure 4-2. Illustration of 3D DIC system and strain gauge validation: a) schematics of 3D DIC and its output of major strain and displacement; b) schematics of strain gauge set up and its output of major strain.

In the normal strain measurement, only few millistrains will be obtained, and quantities larger than that are rarely involved. Thus, to accurately observe such small change in resistance, a voltage excitation source was applied in combination with a special resistance bridge structure called a general Wheatstone bridge, i.e., a quarter bridge circuit built inside the gauge logger

[75]. The output from the gauge logger are magnified four times. To convert into strain ε_{gauge}, a quarter bridge circuit for strain is given by the equation shown below:

$$\varepsilon_{gauge} = -\frac{4 \cdot V}{(2V + 1) \cdot GF} \qquad \textbf{Equation 4-6}$$

where GF is the gauge factor, the ratio of change in electrical resistance to the change in strain (2.1 is the GF for FLA-2-8 strain gauge) and V is the ratio of output of bridge voltage to the excitation voltage. The sampling rate is 0.1 Hz.

The 3D DIC results were checked by strain gauge for validation, then the 3D DIC strain results were used to work out biaxial bending stress. The radial stress (σrad) and tangential stress (σT) were calculated using **Equation 4-3** and **Equation 4-4**. based on validated strain results from 3D DIC. It was found that the biaxial relationship between radial stress (σrad) and tangential stress (σT) was similar for all of the monolithic glass specimens. **Equation 4-5** was be used to work out flexural bending stress (σb) for the monolithic glass.

4.1.2. Weibull modulus and glass strength statistics

Due to the existence of defects and flaws; glass strength relies on experimental strength and the state of surface flaws and defects, testing results show large scattering and a large number of testing samples are required to achieve a stable representative. Glass failure does not follow normal statistics due to flaws associated with processing. Normally, Weibull distribution shows the probability of failure and represents the statistics of glass strength and other brittle material. Weibull distribution shows the probability of the defect level, which is flaw size dependent [24,76,77].

$$P_f = 1 - exp\left[-\left(\frac{\sigma}{\sigma_0}\right)^m\right] \qquad \textbf{Equation 4-7}$$

Where Pf is the failure probability at applied stress; σ is the applied stress; σ0 is the threshold failure stress (normally at 60% - 70 %); and m is the Weibull factor/modulus, which, as noted, indicates the strength of the glass with regard to flaws [78]. In general, the strength of the glass depends on the state of flaw, the type and magnitude of stress and glass material properties [76].

4.1.3. Dynamic mechanical analysis (DMA)

Due to various temperature conditions affecting flying aircraft, this section of the tests was aimed at understanding the influence of temperature on the mechanical properties of polymers, or in other words, the material behaviour of polymer as part of the laminate at different temperature conditions.

4.1.3.1. Method and material

Dynamic mechanical analysis (DMA) is a thermal analysis used to investigate the viscoelastic behaviour of polymers under periodic stress, when they can take the form of either an elastic solid or a viscous fluid. Viscoelastic behaviour is measured by using the dynamic oscillatory tests method, whereby a sinusoidal stress is applied on the polymer specimen and a resultant strain is obtained. A TA Instruments Q800 DMA machine was used to study the viscoelastic mechanical behaviour of different types of polymers in tension mode.

The specimen measured 30 mm for valid testing initial length and 6.17 mm for valid testing initial width. Various types of polymer have different thicknesses: the thickness of TPU is 1.27 mm, the thickness of SGP is 1.52 mm and the thickness of PVB is 0.76 mm. A preload (0.01 N) was added to avoid any buckling and ensure straight positioning from the starting point of the test. Oscillating displacement (amplitude control of 20.0 μm at maximum 0.2%) was transmitted from the pushing rod to supply a periodic load, and a thermocouple detector was placed close to the tensile specimen to monitor temperature changes in the environmental chamber. The stress and strain were calculated based on the application of periodic force and the geometric dimensions of the specimen. The specimen was tested at constant 1 Hz frequency and held isothermally for 10 minutes at -100 °C, then took a ramp of 2 °C per minute until it

reached 80 °C. The procedure was repeated three times for each type of polymer to guarantee accuracy.

4.1.3.2. Glass transition

Glass transition occurs in amorphous materials or in amorphous regions within semi-crystalline materials. Despite the crystalline portion, the amorphous portion, exhibits a glass transition in which higher temperatures allow the polymer to transfer from a hard glassy material to a soft rubbery material. When the temperature is low, the amorphous part of the polymer has insufficient energy to move, which makes the polymers take on a stiff and brittle form, like glass. When the temperature rises, the amorphous part of the polymer is able to move, and the polymers become soft and flexible, making it easier to change shape. The temperature changes resulting in the transition from a glassy to rubbery state is the transition region, which identifies the mechanical behaviour changes for a polymer. The glass transition temperature is the temperature at which polymer change its mechanical behaviours.

4.1.3.3. Viscoelasticity

Viscoelasticity is a common material property whereby polymer exhibits both viscous and elastic mechanical behaviour when under deformation. Viscosity measures polymer resistance to gradual deformation by shear stress or tensile stress. Strain changes linearly with time, and elasticity gives polymer ability to return its original length after a certain amount of deformation in the elastic range. When polymer endures a sinusoidal stress over time, the mechanical behaviour at a single frequency must be specified by two independent quantities: input stress and resultant strain. Normally, the stress is not in phase with the strain, but the stress can be split into two sub-quantities, with one in phase and the other 90 degrees out of phase. Therefore, to assess tension quantity (E), will involve measurements of in phase stress (strain tension quantity) (E'), and shear quantity (G') (referring to storage modulus in tension and shear), as well as out of phase stress (E": strain tension quantity) and shear quantity (G''). The tangent of the phase angle (tanδ) is equal to the following equation:

$$\tan\delta = \frac{E''}{E'} = \frac{G''}{G'} \qquad \textbf{Equation 4-8}$$

When tanδ is zero, the polymer behaves purely elastically, as stress and strain are in phase at 0 degrees; when tanδ is one, the polymer behaviour is half viscous and half elastic, as stress and strain are 45 degrees out of phase; when the angle is increased to 90 degrees, the tanδ is not defined.

Glass transition temperature can also be determined using plots of different modulus versus temperature curves (storage modulus, loss modulus and tan tanδ): The amplitude of the stress in-phase with the strain divided by the strain amplitude is referred to as the storage modulus and is denoted by E' in tension and G' in shear. The amplitude of the stress out-of-phase with the strain divided by the strain amplitude is referred to as the loss modulus and is denoted by E'' in tension and G'' in shear. The ratio of the moduli is equal to the tangent of the phase angle shown in Equation 4-8.

4.1.4. Polymer tensile experiments

Before any types of polymers are examined as parts of the engineering structure, it is crucial to understand the mechanical properties of polymers themselves. Low strain rate tensile test was performed on screw driven test machine.

4.1.4.1. Method and material

An Instron 5800 series screw-driven machine was used to load the polymer specimens in the tensile test. The test specimen was connected through two clamps connected to the actuator and 10 kN load cell on the test machine. The test machine was driven by the screw rack, which imposes certain limits on the speed of 0.07 m s^{-1} specified by the mechanical design.

The specimen (dumbbell shaped) was prepared following ASTM D412-06a standards for polymer tensile tests: gauge length 35 mm, gauge width 6.17 mm and specimen thickness 1.25 mm. All the specimens were cut from the polymer sheets provided on the available markets.

The true strain was measured using a video extensometer from Imetrum, allowing local strain to be tracked by monitoring changes on the gauge area. Test speed was 5 mm min^{-1} (at an equivalent strain rate of 0.0024 s-1). Three repeat tests were conducted for each of the polymer types.

4.2. Results

4.2.1. Monolithic glass

Comparisons of strain gauge and 3D DIC results are summarised in **Figure 4-3**. Data sources for strain gauge and 3D DIC were at the centre of the specimen. Strain data (solid lines) correlated well with the 3D DIC results (open points) for 2.2 mm, 4.0 mm, and 6.0 mm chemically strengthened monolithic glass, proving that the strain data from 3D DIC was valid. Each thickness was repeated at least 12 times for accuracy. Despite the differences in thickness, specimens for all three thicknesses failed similar at a maximum strain of 0.8%. Strain in an average of these three thicknesses was broken around 0.8 %. As the thickness increases, the strain versus time curve changes from curved to linear. 2.2 mm, 4.0 mm, and 6.0 mm chemically strengthened monolithic glass fractured under different loading durations, whereby the 2.2 mm glass fractured after 450 seconds, the 4.0 mm fractured after 948 seconds and the 6.0 mm fractured after 2070 seconds.

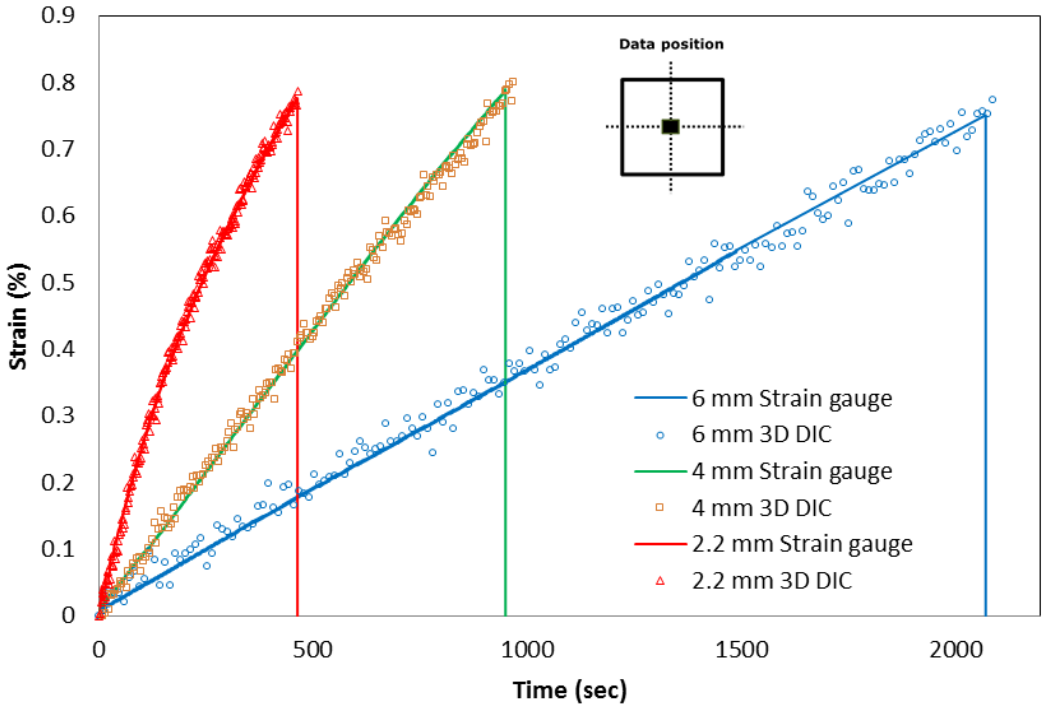

Figure 4-3. 3D DIC results (open points) match with strain results (solid lines) from the strain gauge soldered at the centre of monolithic glasses at a thickness of a) 2.2 mm (red/circle), b) 4.0 mm (orange/square), and c) 6.0 mm (blue/triangle).

After validation of the 3D DIC method was achieved, strain and displacement visualisation profiles were extracted from 2.2 mm, 4.0 mm, and 6.0 mm chemically strengthened monolithic glass, results for which are summarised in **Figure 4-4**. **Figure 4-4**.a summarises the out-of-plane displacement visualisation profiles. There were seven images selected by equal divisions of the time range of each thickness's test before fracture. All of the visualisations use the same legend scale from 0.0 mm to 3.6 mm. Gradations of colour represent the extent of displacement tested from each thickness, whereby 2.2 mm monolithic glass shows the greatest displacement, around 3.2 mm at 450 seconds, whereas 4.0 mm monolithic glass exhibits displacement around 1.9 mm at 948 seconds and 6.0 mm monolithic glass is displaced around 1.2 mm at 2070 seconds. **Figure 4-4**.b summarises major strain visualisation profiles. All of the visualisations of major strain use the same legend scale from 0.0 % to 0.9 %. Different strain contours have been observed for various thicknesses, whereby 2.2 mm monolithic glass clearly showed the highest strain concentration on the ring shape (highlighted in dark red), yet remained light red at the core. Clear multi-colour gradients were observed clearly for 2.2 mm monolithic glass before its fracture at 450 seconds. Comparing the images, the 3.2 mm displacement from 2.2 mm monolithic glass experienced a large deflection. At this stage, with the involvement of

large deflection and significant membrane force, the linear bending theory is no longer valid. This trend diminished as the thickness was increased to 6 mm, and a much vaguer colour transition was observed in the 6 mm monolithic glass.

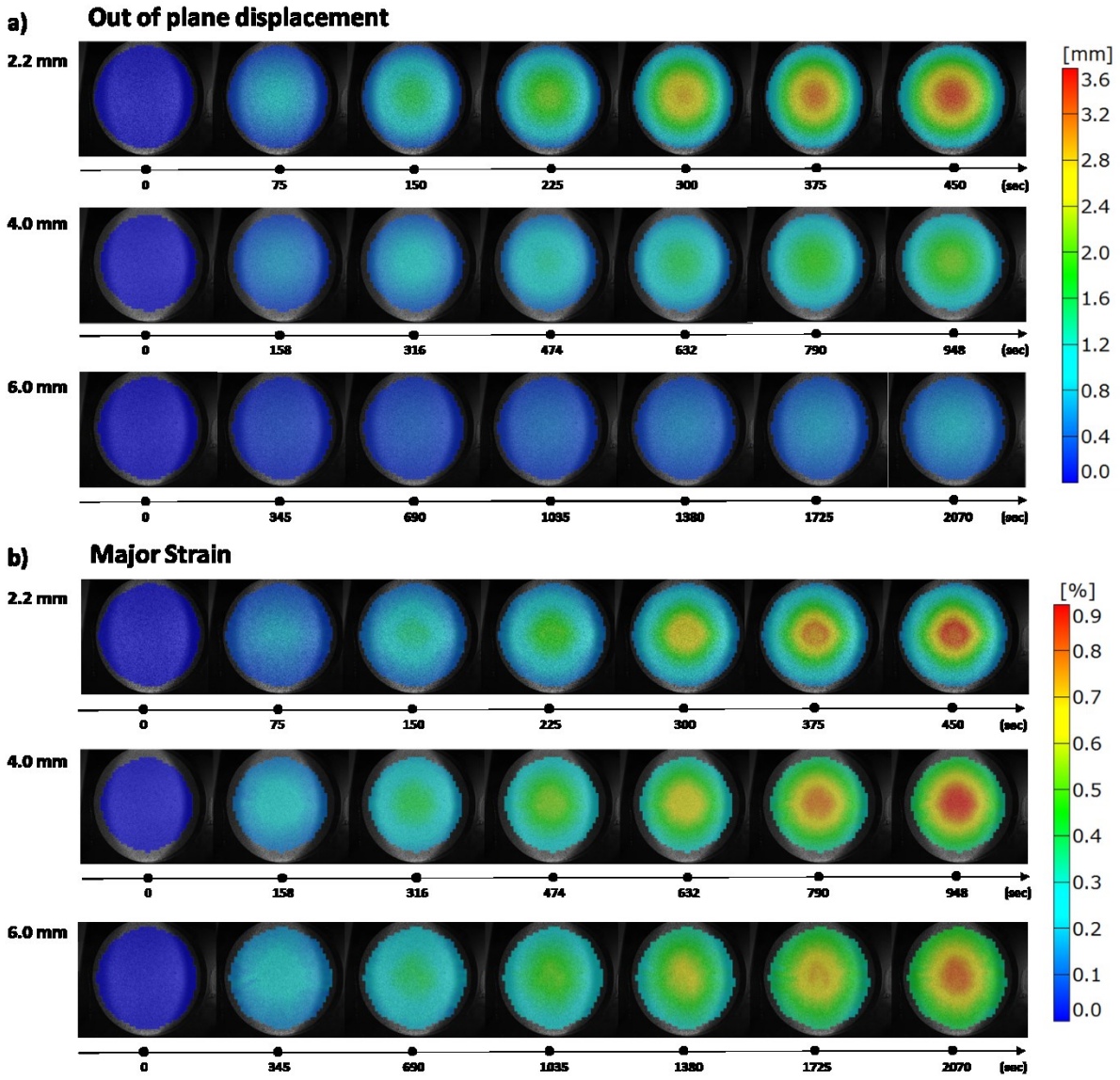

Figure 4-4 3D DIC image series of: a) out of plane displacement and b) major strain for 2.2 mm, 4 mm, and 6 mm thicknesses at quasi static loading of 10 N/sec.

Figure 4-5 depicts a summarised load versus cross-head displacement and strain versus cross head displacement to help illustrate the differences. Dashed lines represent the linear fitting calculated based on the linear bending theory by applying **Equation 4-1**. Solid lines denote the experimental results from the tests. A clear deviate can be observed from **Figure 4-5**.a whereby the load calculated from the standard was underestimated compared to the actual results from the measurement. This deviation started becoming smaller and more linear as the thickness of

the specimen increased from 4 mm to 6 mm, as seen in **Figure 4-5**.c and **Figure 4-5**.e respectively. Comparing 2mm thickness, 4 mm starts to deviate at the late stages by comparing solid and dashed lines in **Figure 4-5**.c. Comparing the solid and dashed lines (Figure 3-5 c), the 4 mm glass starts to deviate at later stages than the 2.2 monolithic glass. By virtue of chemical strengthening method, 2.2 mm monolithic glass followed non-linear behaviour and exhibited a large amount of deflection. This non-linear behaviour, indicated in **Figure 4-5**.a as a curved solid line above the linear dashed line derived from theory at 2.2 mm thickness, diminished as the thickness of the glass plate increased, as seen by the reduced deviation of the non-linear solid line from the dotted line at 4 mm in **Figure 4-5**.c, and finally a match between the experimental and linear fittings at 6 mm (**Figure 4-5**.e). Only the 6 mm glass plate obeyed linear bending theory and correlated with the theoretical linear fitting curve derived from the theory.

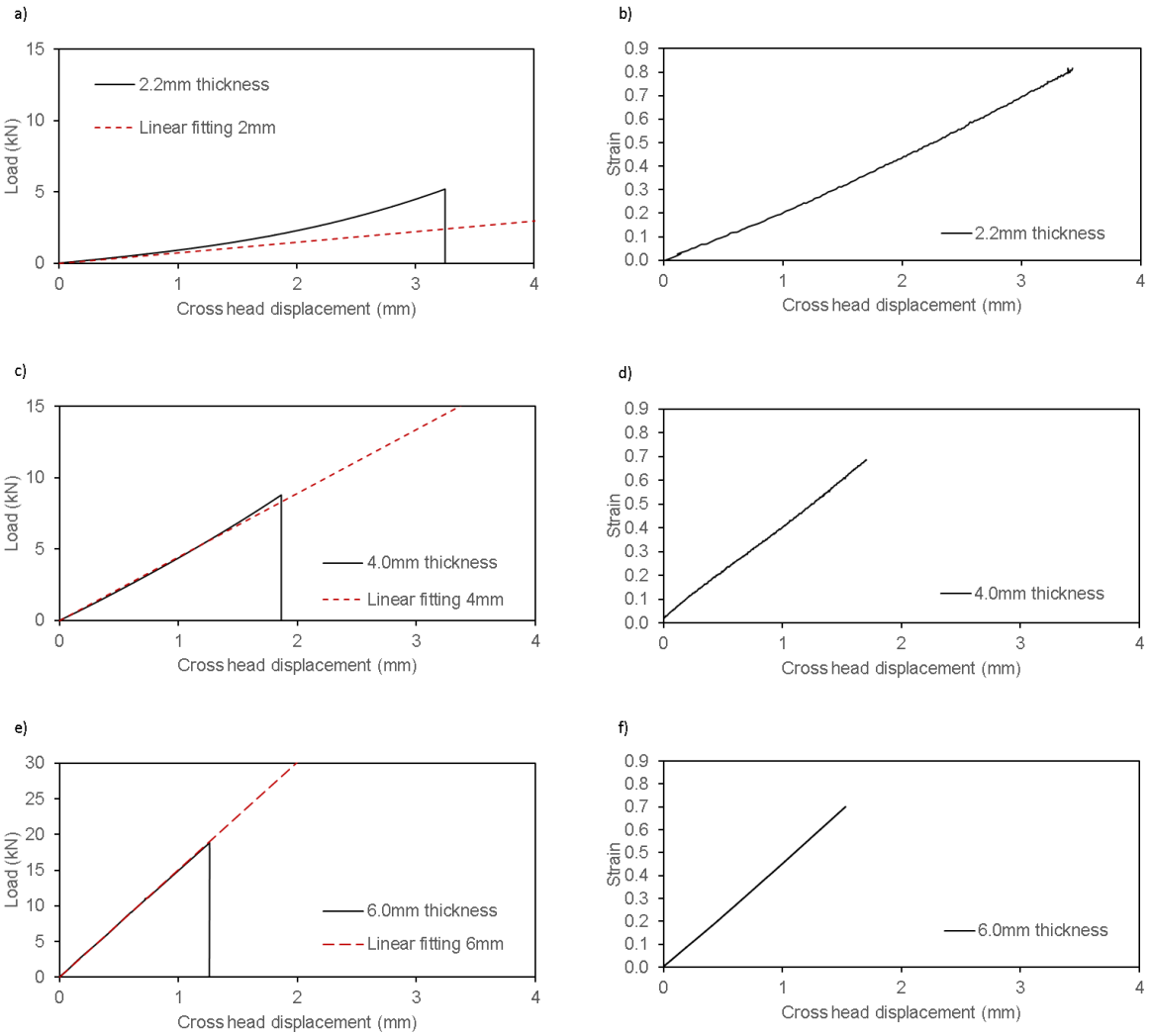

Figure 4-5 Comparison between experimental results from testing machine (black, solid lines) and linear elasticity theory fitting of monolithic glasses (red, dashed lines): a) load versus cross head displacement and b) strain from strain gauge versus cross head displacement of 2.2 mm, c) load versus cross head displacement.

Taking a close look at the 2.2 mm load versus cross head displacement from **Figure 4-5**.a, the curve correlates with the cross plane sections extracted from 2.2 mm 3D DIC strain and displacement images from **Figure 4-4**.a and **Figure 4-4**.b. This correlation is illustrated in **Figure 4-6**. The load versus cross head displacement curve was equally divided into 8 section points in **Figure 4-6**.a. Corresponding cross plane sections of strain and displacement information were extracted from the 3D DIC and summarised in **Figure 4-6**.b and **Figure 4-6**.c, respectively. As mentioned above, in the linear calculation from the standards of flexural bending stress, the membrane force was dominant when large deflection occurred, and radial stress was no longer equal to tangential stress. As a result, the maximum stress was no long uniform at the maximum, which is indicated as the concave shape strain plateau in **Figure 4-6**.b.

a)

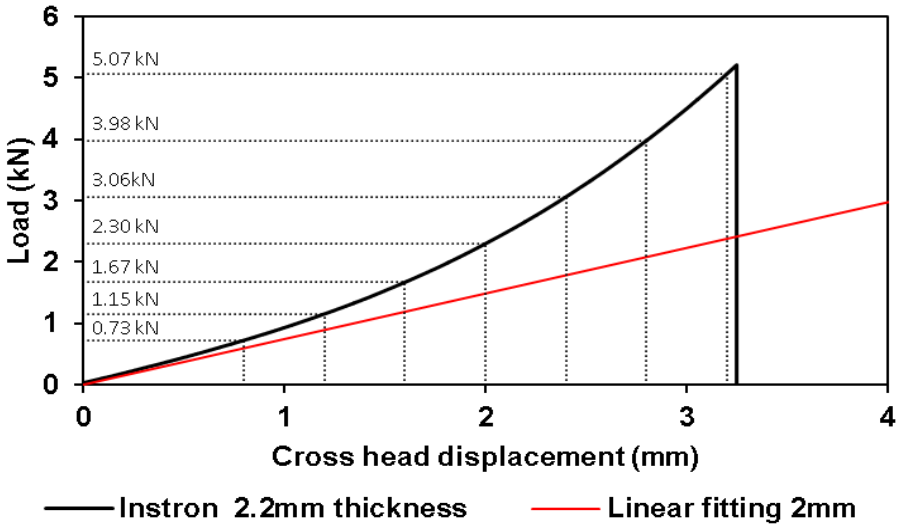

b) c)

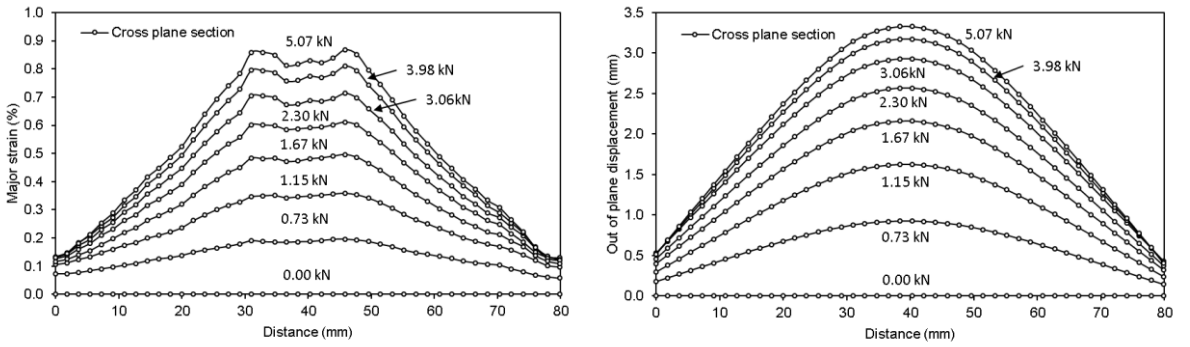

Figure 4-6 Test results of 2.2 mm monolithic glass for a) load versus cross head displacement from experiment and linear elasticity fitting; b) major strain and c) out of plane displacement contour profiles with corresponding maximum load tracing.

4.2.2. Weibull distribution

Coaxial ring bending strength data was evaluated by using the Weibull distribution parameter in combination with the two parameters of the maximum likelihood method. For brittle material in general, flexural bending strength obtained from coaxial ring compression was not a deterministic property to the final failure strength. Somehow, the strength level tested from the double rings still reflected certain degrees of intrinsic fracture toughness and distribution of the defect/cracks inside material. By analysing the Weibull parameter, glass flexural bending results could be determined through vital failures of crack propagation from material. Surface cracks are generated mainly during the manufacturing process.

Glass specimens normally yield distinct multi cracks during the loading process. Thus, glass flexural bending results contain censored data, and a statistical approach can handle multiple flaw distributions. This is the reason for using the maximum likelihood Weibull distribution technique, to develop a likelihood function based on the available data and find the values of the parameter estimates that maximise the likelihood function. A normal three parameter Weibull probability density function includes scale, shape and the location parameter [76], yet this study employed a two-parameter Weibull failure probably study, for which only scale and shape were picked. The Weibull linear plot was applied in **Figure 4-7** to demonstrate the empirical cumulative distribution function of the censored data logarithm scale of failure stress using **Equation 4-7**, rearranging the equation to give a linear standard form as:

$$\ln\left(-\ln\left(1-P_f\right)\right) = \mathrm{m}\ln\sigma - \mathrm{m}\ln\sigma_0 \qquad \textbf{Equation 4-9}$$

If $\ln\left(-\ln\left(1-P_f\right)\right) = y$, $\ln\sigma = x$ and $\ln\sigma_0 = b$, the solid shape linear plots take the form of the equation y = mx – mb to observe the qualities of the Weibull distribution in **Figure 4-6**. For each thickness, there was 15 repeated tests. Strength distributions were plotted for 2.2 mm, 4.0 mm, and 6.0 mm chemically strengthened monolithic glass. The shape and scale for 2.2 mm thickness are m = 47.6 and σ_0=727.5 MPa; m = 55.7 and σ_0=764.0 MPa for 4.0 mm thickness; and m = 61.7 and σ_0=766.6 MPa for 6.0 mm thickness.

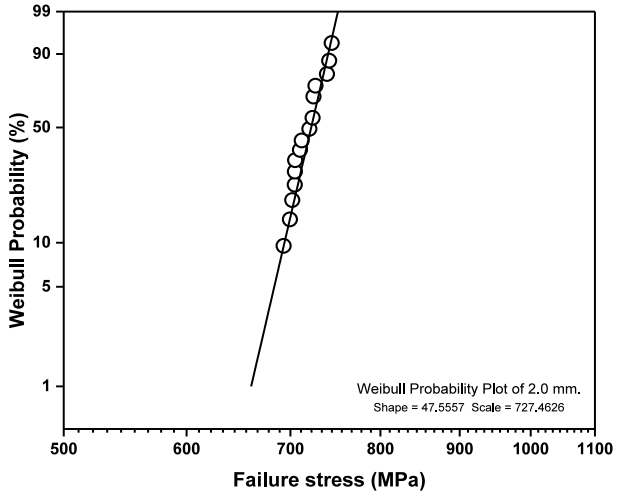

a)

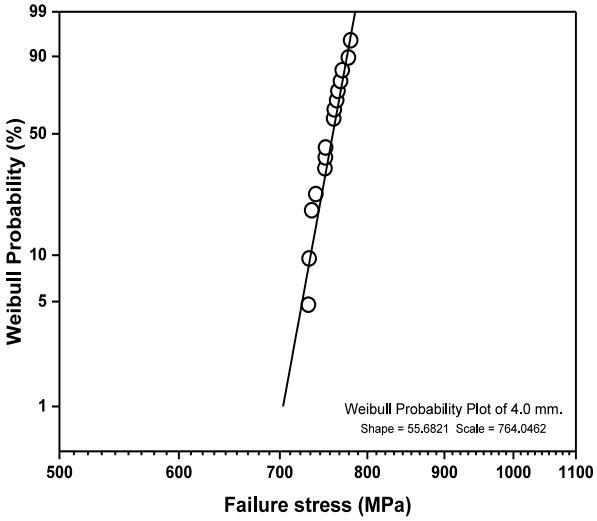

b)

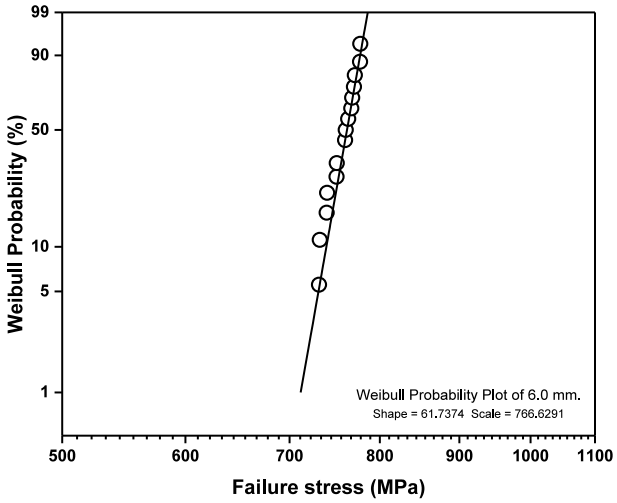

c)

Figure 4-7. Weibull probability function for ring on ring compression test of a) 2.2 mm b) 4 mm, c) 6 mm chemically strengthened monolithic glass.

4.2.3. DMA results

The glass transition temperatures of TPU, PVB and SGP were selected at temperatures at which the peak value of tanδ was obtained. **Table 4-1** shows the temperature results in three different ways. The temperature orders are all the same for each polymer type: $T_{gs} < T_{gl} < T_{gt}$.

Table 4-1. Result of glass transition temperatures from storage modulus, loss modulus and tanδ.

Glass transition temperatures from storage modulus (T_{gs})		
TPU	PVB	SGP
-60 °C	10 °C	40 °C
Glass transition temperatures from loss modulus (T_{gl})		
TPU	PVB	SGP
-50 °C	13 °C	45 °C
Glass transition temperatures from tanδ (T_{gt})		
TPU	PVB	SGP
-32 °C	27 °C	54 °C

Storage modulus, loss modulus and tanδ versus temperature curves are shown in **Figure 4-8**.a, **Figure 4-8**.b, and **Figure 4-8**.c, respectively. Glass transition regions can be seen on the storage modulus, loss modulus and tanδ curves for these three types of polymer. At temperatures below approximately -70 °C, the TPU was found to be in the glassy region and the storage modulus in **Figure 4-8**.a was in order of 1 GPa. Between -70 °C and -64°C, the modulus began to drop rapidly in magnitude as the TPU transferred to its transition region. The lost modulus in the glassy region in **Figure 4-8**.b was relatively stable, and the order was in 100 MPa. It was one tenth of the ratio of storage modulus over loss modulus (tanδ), yielding 5.7° of the phase angle (δ). The viscoelastic mechanical behaviour was more noticeable and prominent in the glass transition region. The modulus between storage and loss was similar in the transition region; thus the phase angle was approximately 45° or larger for this region. For temperatures above approximately -20 °C, TPU was in the rubbery region, and the storage modulus dropped to 1

MPa with a loss modulus at 0.1 MPa. The δ was back to approximately 5.7° for one tenth of the tanδ.

The mechanical response of PVB and SGP was similar to TPU's, but shifted to different temperature ranges. TPU had the lowest glass transition temperature region, followed by PVB, and SGP had the highest transition temperature region. The viscoelastic behaviour of PVB and SGP was pronounced in the transition region as well. After entering rubbery region, PVB had storage modulus of 1 MPa order and a loss modulus of 0.1 MPa, which yielded a similar δ approximately 5.7° from one tenth of the tanδ. However, SGP showed continuous pronounced viscoelastic behaviour by having 1 MPa order of both storage and loss modulus in the rubbery state.

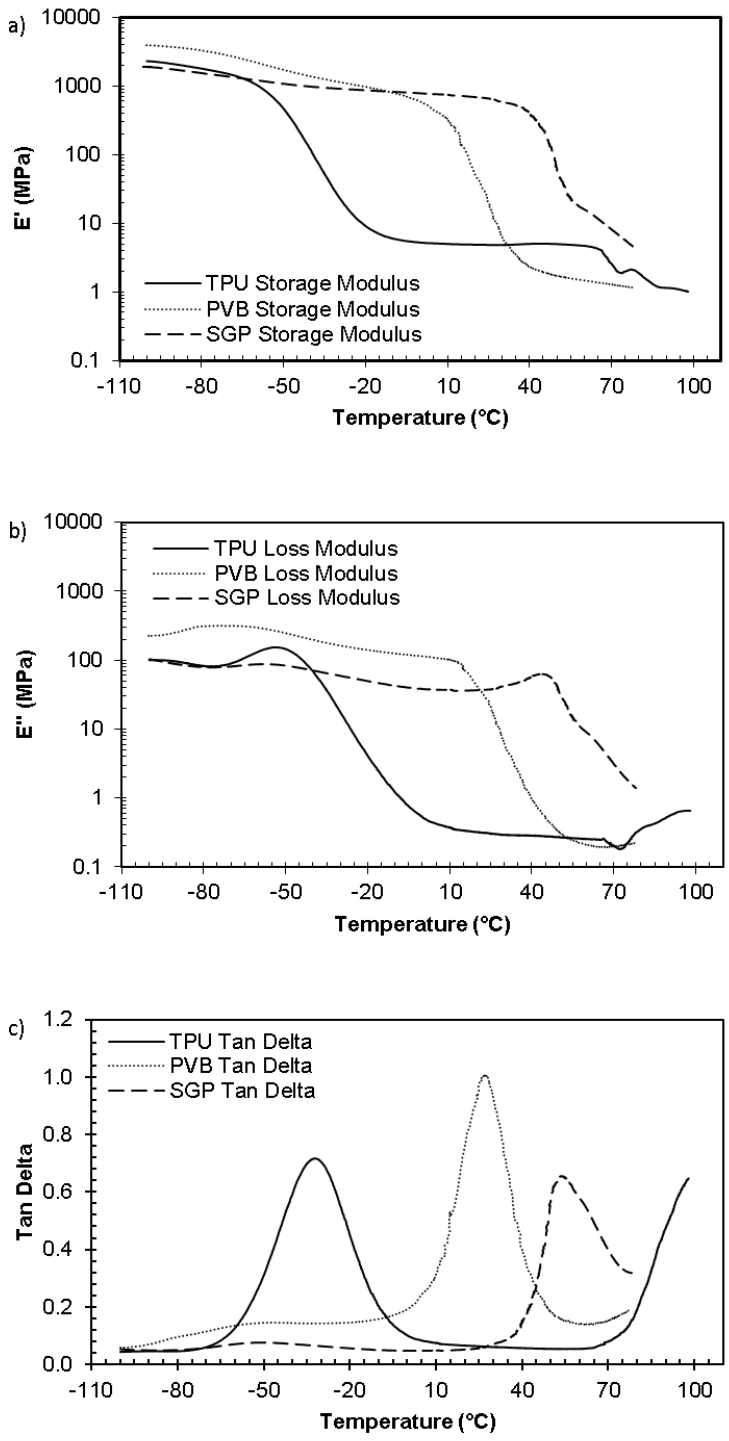

Figure 4-8. Dynamic mechanical analysis for TPU (solid lines), PVB (dotted lines), and SGP (dashed lines): a) tensile storage modulus versus temperature; b) tensile loss modulus versus temperature; c) tan delta versus temperature.

4.2.4. Tensile tests results

SGP is notable for its glassy elasto-plastic material with linear gradients. Both TPU and PVB exhibit similar rubbery viscoelastic behaviour, for which which TPU has a higher modulus. The quasi-static uni-axial tensile behaviour of these three polymer interlayers is shown in **Figure 4-9**. At room temperature, PVB and TPU are in a rubbery state, while the SGP shows a more glassy response, as its glass transition temperature is about 55 °C.

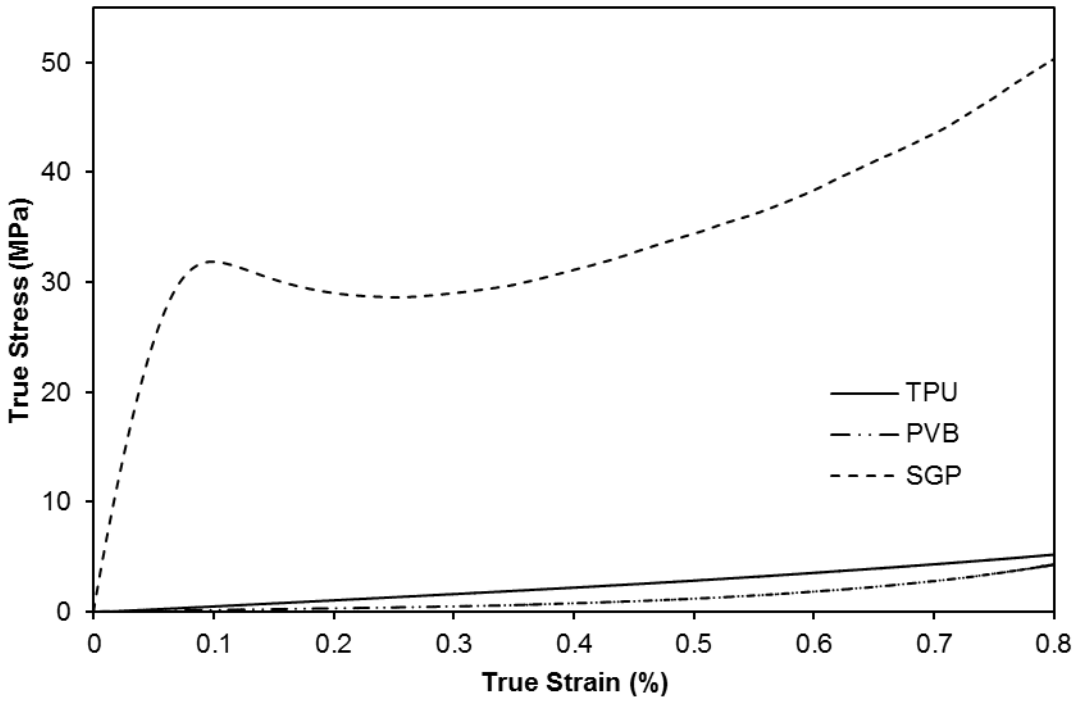

Figure 4-9. Tensile test at 0.0024 s^{-1} for TPU (solid lines), PVB (dotted lines), and SGP (dashed lines) at room temperature.

4.2.5. Result of laminated glass compression tests

Both ring loading and rubber loading were tested on laminated glasses to demonstrate different loading conditions and the consequential difference in fracture sequence as well as strain profile. Laminated glass of different configurations is shown in **Table 3-1**. The effect of polymer interlayer thickness on the impact performance is investigated through C1, C2 and C3. The effect of the type of glass for the frontal layer of 2.2 mm thick glass is investigated, comparing the performance of C3 with C4, which has a thermally rather than chemically toughened glass for its frontal layer. The type of polymer interlayer is changed in C3, C5, C6 and C7 by using TPU, SGP, PVB and multi-layered (TPU SGP/TPU), respectively. All the tested 2.2 mm glass side was on the loading side, while the 4.0 mm glass side comprised the supporting side facing the loading ring. Both ring loading and rubber loading were displacement controlled at 0.5 mm/min.

4.2.5.1. Laminated glass ring loading

Figure 4-10 shows ring on ring results for laminated glasses from curves of load versus cross head displacement and major strain versus cross head displacement to demonstrate differences in the results associated with changes of the configurations. In **Figure 4-10**.a and **Figure 4-10**.b, an increase of the polymer (TPU) interlayer thickness is seen to have caused a change in fracture sequence whereby the 4.0 mm glass side fractured firstly in C1 and C2, while in C3, the 2.2 mm glass side fractured firstly. As a result, as seen in **Figure 4-10**.b, both C1 and C2 loaded linearly up to 0.8 % of fracture on 4.0 mm glass ply, leading 3D DIC to become invalid. On the other hand, C3 fractured the 2.2 mm loading glass ply firstly, followed by the fracture of the 4.0 mm glass ply. Therefore, C3 (in blue, **Figure 4-10**.b) first reached 0.8 % and dropped due to the fracture of 2.2 mm, then reloaded up to 0.8 % due to the fracture of the 4.0 mm glass ply. **Figure 4-10**.a illustrates the corresponding load related to major strain from **Figure 4-10**.b. The maximum load of first fractures for C1, C2 and C3 were similar at around 12 kN. After the first fracture, C1 and C2 broke 2.2 mm glass ply with a much lower load of around 4 kN; in comparison, C3 fractured 4.0 mm with a much higher load of around 10 kN. By observing this difference, it is possible to compare fracture energy underneath load versus cross head

displacement curves. C3 showed a significant improvement in energy consumption before the laminate was fractured.

Figure 4-10c and **Figure 4-10d** show the effects of thermally and chemically strengthened glasses used on 2.2 mm glass side while it is experiencing ring on ring loading. As shown in the much lower maximum load and load drop in **Figure 4-10c,** 2.2 mm thermally strengthened glass proved to be weaker, as it promoted the fracture faster compared to the 2.2 mm chemically strengthened glass ply. Linking maximum load with corresponding major strain from 3D DIC in **Figure 4-10d**, we found that thermally strengthened glass broke at a much lower strain of around 0.3 %, whereas C3 broke at 0.8 %. In C3 and C4, after the 2.2 mm glass ply was broken, both exhibited similar traces starting at approximately 2.5 mm cross head displacement in the figure until final failure occurred at the similar load, displacement and strain at approximately 6.0 mm cross head displacement. Therefore, thermally strengthened glass had less energy consumption compared to the chemically strengthened glass used in C3.

Figure 4-10.e and **Figure 4-10**.f show the effect of different polymer types (stiffness of the polymer and multi-layered system) on maximum load before fracture. Two different gradients were observed when comparing C5 with C3, C6 and C7, as shown in **Figure 4-10**.e. C5, using SGP, which is rigid comparing other polymers at room temperature due to high glass transition temperature (54 °C), showed the highest maximum load of approximately 20 kN, while the others were around 12 kN. As shown in **Figure 4-10**.e an increase of the stiffness of the polymer interlayer increases the load tolerance of the laminated structure and requires a larger fracture load, but less bending in terms of the cross head displacement shown in **Figure 4-10**.f. C3 and C6 had the same fracture sequence beginning with the 2.2 mm glass side then followed by the 4.0 mm glass side. The 4.0 mm glass side fractured first for the multi-layered polymer C7.

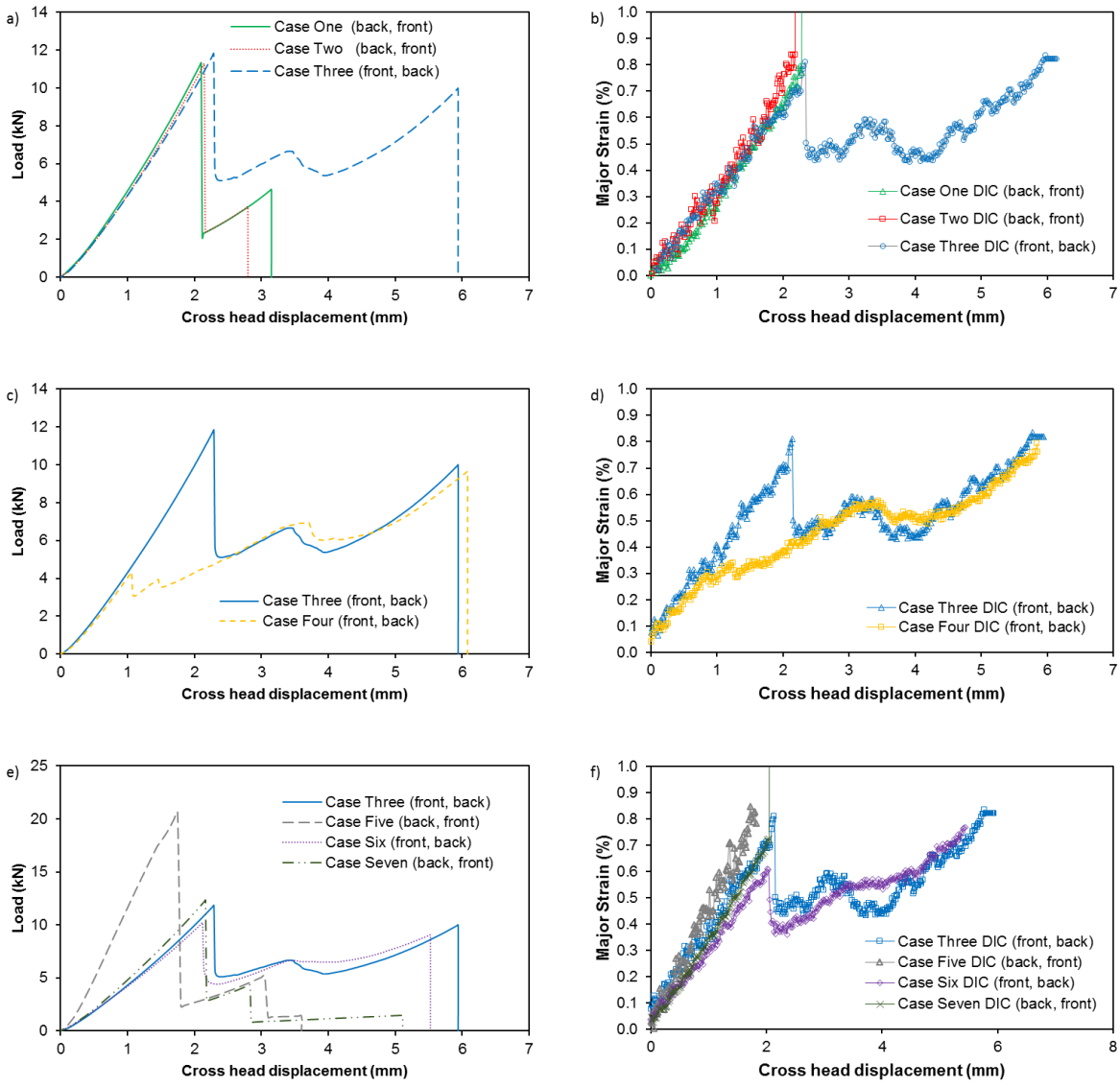

Figure 4-10. Ring on ring results for laminated glass at 0.5 mm/min displacement control. Load versus cross head displacement and major strain from 3D DIC versus cross head displacement for case one, two and three in a) and b), respectively; case three and four in c) and d), respectively; case three five, six and seven in e) and f), respectively.

4.2.5.2. Laminated glass rubber loading

Similar results were summarised for rubber loading tests as well on the same laminated glass configurations in **Figure 4-11**. Silicon rubber cord (20 mm length) was loaded on ring support to generate more uniformly distributed stress. Load versus cross head displacement, major strain versus out of plane displacement and major strain versus out of plane displacement for C1, C2 and C3 are shown in **Figure 4-11**.a and **Figure 4-11**.b respectively; C3 and C4 in

Figure 4-11.c and **Figure 4-11**.d respectively; C3, C5, C6 and C7 in **Figure 4-11**.e and **Figure 4-11**.f, respectively;

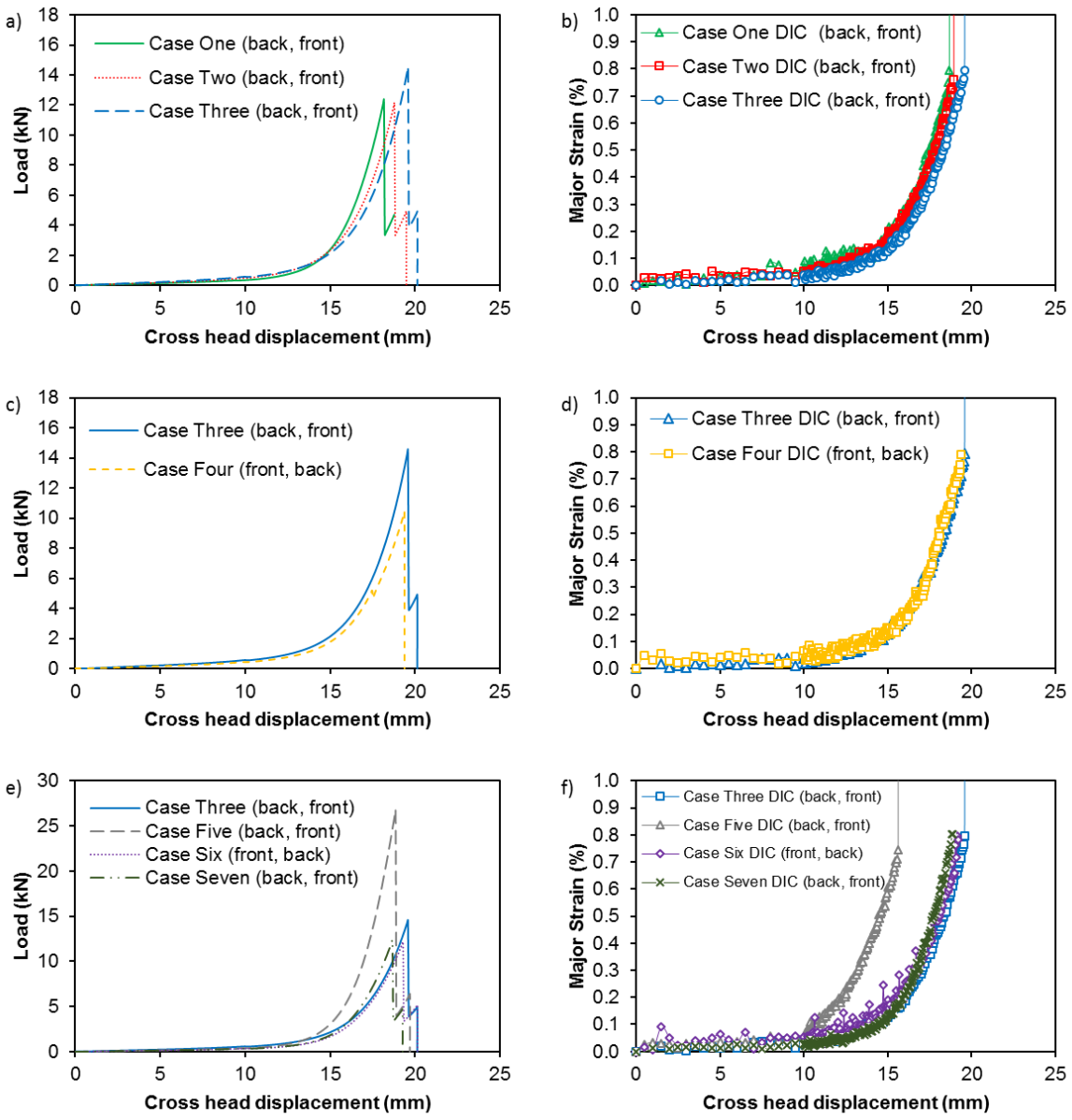

Figure 4-11. Silicon rubber cord (20 mm) on ring support compression results for laminated glass at 0.5 mm/min displacement control. Load versus cross head displacement and major strain versus out of plane displacement from 3D DIC for C1, C2 and C3 in a) and b), respectively; C3 and C4 in c) and d), respectively; C3, C5, C6 and C7 in e) and f), respectively.

In **Figure 4-11**.a and **Figure 4-11**.b, an increase of the polymer (TPU) interlayer thickness is seen to have caused a change in maximum fracture load and slightly increased cross head displacement as seen in **Figure 4-11**.a. Also, all three cases of C1, C2 and C3 fractured the 4.0 mm glass side firstly and as seen in **Figure 4-11**.b, C1, C2 and C3 loaded exponentially up to

0.8 % of fracture on 4.0 mm glass ply, leading 3D DIC to become invalid. **Figure 4-11**.a illustrates the corresponding load related to major strain from **Figure 4-11**.b, the maximum load of first fractures for C1, C2 and C3 were increased from around 12 kN.of C1 and C2 to approximate 14 kN of C3. After the first fracture, C1, C2 and C3 broke and the 2.2 mm glass ply with a much lower load of around 4 kN which was similar to that observed in rigid loading in **Figure 4-10**.a. By observing this difference in the maximum fracture load difference, it is possible to compare fracture energy underneath load versus cross head displacement curves. C3 showed an improvement in energy consumption before the laminate was fractured.

Figure 4-11.c and **Figure 4-11**.d show the effects of thermally and chemically strengthened glasses used on 2.2 mm glass side while it is experiencing rubber on ring loading. As shown in the much lower maximum load and load drop in **Figure 4-11**.c**,** 2.2 mm thermally strengthened glass proved to be weaker, as it promoted the fracture faster compared to the 2.2 mm chemically strengthened glass ply while there was no significant influence on overall energy consumption of C4 from **Figure 4-11**.c (yellow dashed line). Linking maximum load with corresponding major strain from 3D DIC in **Figure 4-11**.d, we found that both thermally and chemically strengthened glass broke at 0.8 %. Unlike what happened in rigid loading, due to the lower strength of thermally strengthened frontal glass layer, C4 broke 2.2 mm glass ply firstly during the initial loading, and then caused final failure of the 4.4 mm. Whereas C3 broke back layer firstly and then 2.2 mm in the end. Both C3 and C4 exhibited similar traces and showed final failure strain at approximate 0.8 % in **Figure 4-11**.d. However, C3 had much higher fracture load at around 14 kN comparing with C4 at around 10 kN from **Figure 4-11**.c. Therefore, thermally strengthened glass had less energy consumption compared to the chemically strengthened glass used in C3.

Figure 4-11.e and **Figure 4-11**.f show the effect of different polymer types (stiffness of the polymer and multi-layered system) on maximum load before fracture. Two different gradients were observed when comparing C5 with C3, C6 and C7, as shown in **Figure 4-11**.e. C5, using SGP, which is rigid compared to the other polymers at room temperature due to high glass transition temperature (54 °C), showed the highest maximum load of approximately 26 kN, while the others were around 14 kN. As shown in **Figure 4-11**.e an increase of the stiffness of the polymer interlayer increases the load tolerance of the laminated structure and requires a larger fracture load, but less bending in terms of the cross head displacement shown in **Figure 4-11**.f. C6 had a different fracture sequence comparing C3, C5 and C7 beginning with the 2.2 mm glass side then followed by the 4.0 mm glass side.

4.3. Discussion

4.3.1. DMA

As described previously, the calculation of glass transition temperature was made using three different methods: extrapolation from onset of sigmoidal changes in storage modulus (Tgs); temperature for peak value of loss modulus (Tgl); and temperature for peak value of tanδ modulus (Tgt). Tgs occurred at the lowest temperature amongst the three methods. Each of these temperatures happened slightly differently, but together they described the whole glass transition range. **Table 4-1** shows an example of TPU storage modulus, loss modulus and tanδ. The glass transition temperatures were indicated on the graph as well: Tgs is – 60°C; Tgl is – 49°C, Tgt is – 33°C.

The onset temperature of storage modulus (also called elastic modulus) shows a decreasing trend of the elastic modulus at the highest temperature. This indicates the start point of material physically softening, i.e., if polymer is heated up beyond this point, the mechanical property will change. The peak of the tanδ happens at the highest temperature, indicating the middle point of material transition between glassy and rubbery states. The interest of the study is focussed on the mechanical performance; thus, it would be useful to use the glass transition temperature from the storage (elastic) modulus method for all the tests. However, extrapolation from the tangent intersecting method is dependent on the curves, which means the determination of the temperature varies with error. The tanδ is the ratio of loss modulus over storage modulus, also called damping, which measures the energy dissipation of a material during the work, which in turn demonstrates how well the material, in this case, polymer, can absorb energy. Additionally, the peak value of the tanδ modulus (Tgt) was the easiest means to define temperature in general amongst the three methods. Therefore, all of the glass transition temperatures were determined from the tanδ method.

In the literature, the glass transition temperature of three different polymers are TPU at -49 °C [70], PVB at 20 deg glass [71] and SGP at 55 deg glass [42]. The literature value of TPU was reported using the middle point from differential scanning calorimetry, which met the T_{gl} result from loss modulus in **Table 4-1**. Both PVB and SGP correlated well with the glass transition temperatures obtained by peak value of the tanδ modulus (T_{gt}) method.

For aircraft windshield design, a functional heating layer will guarantee the windshield temperature from cockpit and cabin at ambient temperature (21°C). Therefore, the temperature

working range for the polymer from laminate would be 21°C, and if a variable of ± 10°C is added for different conditions, the temperature range would be from 11 °C to 31°C. The storage and loss modulus are shown in **Figure 4-8** a) and b), respectively. A clear transition range of PVB is observed in both storage and loss modulus curves. TPU is in its rubbery phase from both storage and loss modulus curves and SGP is in its glassy phase from both storage and loss modulus curves.

4.3.2. Laminated glass

At room temperature, SGP exhibits a glassy state, while TPU and PVB are in rubbery states from DMA results. Based on tensile test results, SGP shows an elasto-plastic true stress true strain relationship with the linear initial gradient. Both TPU and PVB exhibit similar viscoelastic behaviour, though TPU has a higher modulus. This variation will lead to a different structural performance of laminated glass in the ring loading and rubber loading tests. The area underneath the load versus extension curve from **Figure 4-10** has been converted into the energy consumption that is needed to break glass layers. The summary of the energy contribution to break each configuration under the ring on ring test is listed in **Figure 4-12**. Due to the cost and difficulty of getting specimens, all the configurations had been tested once only without error bar.

C1, C2 and C3 have the same glass ply configuration, but increasing polymer (TPU) thickness from 0.76 mm, 1.27 mm and up to 3.18 mm, respectively. When comparing results from C1 at 0.76 mm TPU thickness and C2 using 1.27 mm, there was not much difference. As shown in **Figure 4-12**, once the thickness was increased to 3.18 mm, the energy was more than doubled, and a significant increase was observed in the fracture energy required to break the entire structure of C3. Additionally, the increase of polymer (TPU) thickness from C1 and C2 to C3 caused a change of fracture sequence from the first fracture occurring on the 4.0 mm supporting glass side (C1 and C2) to fractures beginning on the 2.2 mm loading glass side (C3). By altering the fracture sequence observed from C3 and correlating this with 3D DIC observation in **Figure 4-10** a and b, we found that there is a polymer thickness influence on the load transfer and fracture sequence of the laminate whereby a thicker interlayer and concentrated loading condition will lead to loading side 2.2 mm glass ply breaking first, then to the fracturing of the 4.0 mm glass ply. This performance was coincident with research conducted by Bennison and

colleagues [34] on laminated glass, but this is with chemically strengthened laminated glass system.

C3 and C4 were compared using 2.2 mm chemically toughened and thermally tempered glass layers, respectively. In this scenario, a slightly improvement is seen in chemically toughened glass. The comparison of C3, C5, C6 and C7 demonstrate the differences in the structural performance of various polymer types. C3 used TPU, C5 used SGP, C6 used PVB and C7 used a multi-layered interlayer combination of TPU and SGP with similar thickness for all cases (despite small variations in the market availability of polymer thicknesses). Cases using TPU and PVB demonstrated better performance than SGP and multi layered cases in terms of energy absorption and fracture pattern. For C5 using SGP, the high rigidity of SGP made shear stress easier to transfer between the loading glass ply to the supporting glass ply, but also made the whole lamination harder to bend, with less benefits taken from bending energy absorption. Moreover, from the observation of fractured laminated glass after the compression test, C5 was the only case in which catastrophic fracturing caused a complete rupture through the interlayer, ripping off both glass plies as well as the interlayer and fracturing into large completely broken pieces; i.e., the merits of using polymer holding fragment at post-breakage stage were eliminated.

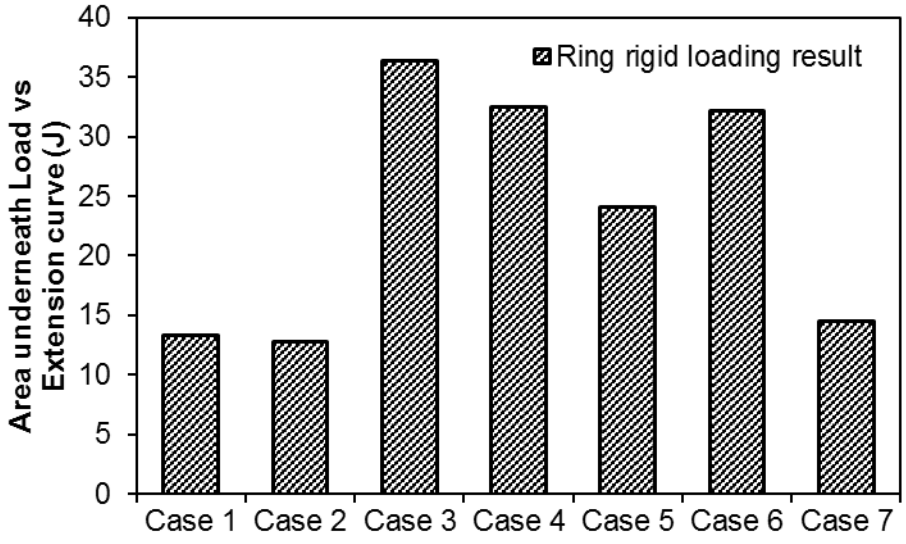

Figure 4-12. Ring on ring energy contribution to break each configuration from load versus extension curve.

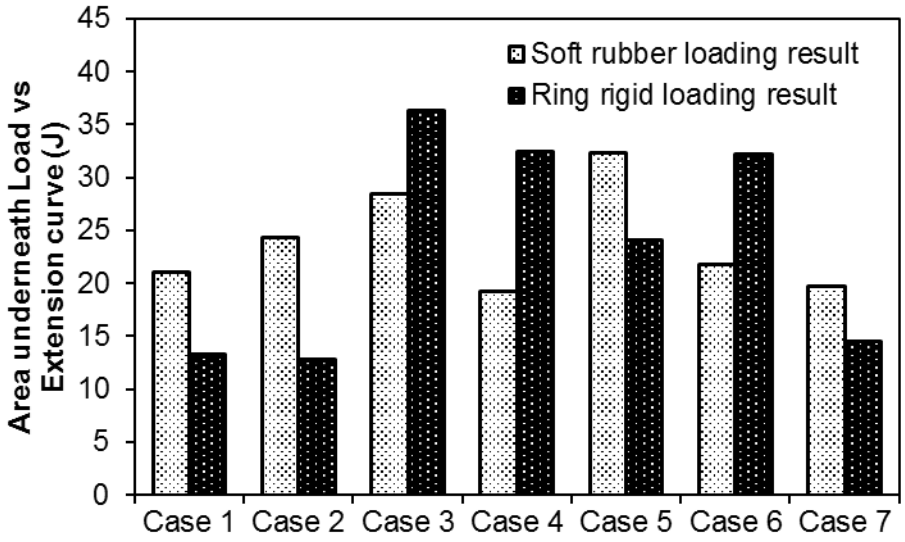

Figure 4-13. Comparison of the energy contribution to break each configuration from load versus extension curve of soft loading and ring loading**.**

Both load versus displacement curves from **Figure 4-12** and **Figure 4-13** clearly showed that two distinguished stages of fracture occurred at a time delayed on breaking front loading 2.2 mm glass ply and back supporting 4.0 mm glass ply with different sequences for both ring loading and rubber loading. The difference between these two loading conditions is that the rigid ring applying concentrated force along the metallic ring with specimen and soft rubber provides more uniformed force from rubber deformation. Due to different loading conditions, a more linear loading relation was observed in the ring loading condition shown in **Figure 4-10** a, c and e indicating a lower peak load before the first fracture occurred. An interesting difference was observed by comparing **Figure 4-10** a, c, e and **Figure 4-11** a, d, g after the first glass ply fractured. For the rubber loading scenario, two sharp drops indicates two breakages of two glass plies in **Figure 4-11** a, d and g. However, if 2.2 mm glass ply broke first, more distinguishable and higher second peak loads were observed for some of the cases.

A comparison of ring loading and rubber loading is summarised in **Figure 4-13**. For C1, C2 and C3, with increased TPU thickness, the energy absorption becomes larger in general. In both the ring loading and rubber loading tests, C1 and C2 fractured first at the back supporting side and then at the loading side. A significant change observed in C3 was that the first fracture happened at the loading side during ring loading, while during rubber loading, the first fracture

happened at the supporting side. Another significant change was that once the loading condition changed to rubber, C5 using rigid SGP could absorb more energy than all the other cases. In terms of the effects of glass strengthening on structural performance, C3 always showed better performance in terms of larger energy absorption compared to C4, using 2.0 mm thermally strengthened loading glass for both ring loading and rubber loading tests. Comparing polymer types, because of higher tensile modulus from true stress strain curve, under the same geometric conditions, laminated glass using TPU (C3) as an interlayer showed better performance than the laminated glass using PVB (C6) in terms of energy absorption for both the ring loading and rubber loading tests. For C3, during the ring loading tests, failure in laminated glass occurred first at the 2.2 mm glass side, whereas the rubber loading test changes the fracture sequence to begin at the 4.0 mm supporting side due to more uniform stress distribution on the loading contact.

In general, glass is a homogeneous, isotropic material that behaves like linear elastic for conventional glass but takes on properties of non-linear elastic for chemically strengthened glass in a maximum biaxial bending strength regime. The assessment of mechanical strength of monolithic glass used in laminated glass requires an accurate flexural bending strength measurement. Normal glass fractures at strain between 0.03 % to 0.5 % [79]. However, chemically strengthened glass exhibits reinforced compressive layers, and the central deflection of the glass plate is greater than half of the specimen's thickness [23]. This makes chemically strengthened glass stronger and more flexible compared to conventional glass. From the experimental results, the strain level needed to break both the chemically strengthened monolithic glass plate and the supporting side of glass ply from laminated glass were all around 0.8 % for both the ring loading and rubber loading tests.

4.4.Conclusion

This paper studied the flexural bending strength of chemically strengthened monolithic glass at the back supporting side using direct strain measurement via the 3D DIC technique. This technique has also been used to study structural performance of laminated glass with different configurations. The following points describe the major conclusions from this study:

- 3D DIC strain measurement copes with coaxial ring on ring compression test is a valid measuring method and can be a test protocol to visualise the strain and displacement changes in a specimen's supporting glass side. This makes calculation of flexural bending stress of monolithic glass more direct. The method is also applicable to laminated glass and other flat specimens.
- 3D DIC results of the comparison between monolithic glass of 2.2 mm, 4.0 mm and 6.0 mm thickness shows a transition from flexural nonlinear bending in 2.0 mm and 4.0 mm thickness to linear bending in 6.0 mm thickness. The calculated flexural bending strength is presented by a two parameter Weibull distribution.
- Laminated glass using SGP shows catastrophic fracture similar to glass of equivalent thickness whereby the interlayer could not hold much fragments after the test.
- Increasing TPU interlayer thickness will cause a change of the fracture sequence of laminated glass from the 2.2 mm loading glass side to the 4.0 mm supporting glass side on ring loading tests.
- Based on the results of both ring loading and rubber loading tests, in terms of energy absorption, the 2.2 mm loading glass side with chemically strengthened conditions shows better performance than that strengthened thermally.
- Multi-layered interlayering has not demonstrated significant improvement of structural performance in either the quasi-static ring or rubber loading tests.
- Under the same geometric conditions, laminated glass using TPU showed better structural performance in than the lamination using PVB.
- In C3, which used TPU as the interlayer, more uniform stress distribution from the rubber loading test leads to the first fracturing occurring at the 4.0 mm supporting glass side, whereas the ring loading test breaks the 2.2 mm glass side first.
- The strain level needed to break both the monolithic glass plate and the supporting glass side from laminated glass are all around 0.8 % for chemically strengthened glasses.

- In comparisons of ring loading methods, rubber loading can provide a higher peak load before the second fracture if the 2.2 mm glass ply breaks first.

5. Impact performance of laminated glass at low velocity

A drop weight tower was used for measuring impact performance of targeting structural performance at low velocity. A systematic study of different laminated glass on soft-rubber impact from a drop weight tower was performed. By interpreting the mechanical response of different laminated configurations at this velocity range, their structural performance on soft-rubber low-velocity impact is compared and studied.

5.1. Method

5.1.1. Experimental setup for drop weight test on laminated glass

The drop weight test was conducted via an essential drop tower testing machine using 60 shore silicone rubber cords of 14 mm in diameter and 37 mm in length. Roughly 17 mm of the rubber cord was secured inside a metallic impactor, leaving 20 mm of rubber cord free for impact contact. The experimental setup consisted of two parts:

1. Two high speed video cameras [80] were placed at two positions: one camera filming from the top of the specimen was used to capture deformation of the soft-body impactor (silicone rubber) and deformation and fractography of the specimen's impacting surface; the other camera was placed at the bottom, filming through a 45° mirror, to monitor back-face deformation and fractography during the lamination mechanical response under impact. Both cameras were triggered and controlled by a laptop for video records. The sampling rate of the test was 11,000 frames per second. The time interval between frames was 90.89 us. The resolution was 512 x 512 pixels. A halogen lamp from the top provided enough light for filming. White acrylic paint was sprayed on the impact surface to help visualization from the high-speed camera videos.
2. An oscilloscope was used to record force from a piezo electronic load cell (PCB 224C, maximum 100 kN load capacity, by PCB Piezoelectric Company). Both impact force and time profile were extracted. The drop weight tower was connected to closed-circuit alarm system for safety issues

By fixing drop height and weight from the drop tower test, three kinds of information were generated:

a. Force and time trace from the load cell.
b. Impact video captured from high-speed cameras.
c. Fracture pattern photo taken after the test.

For the drop tower test, the drop weight was fixed at 16.9 kg for all tests, as shown in **Figure 5-1**. Each of the cases was tested in two steps: the first drop height started at 10 cm and was increased by 5 cm increments until the laminated glass broke. Three repeat tests were conducted for each glass configuration.

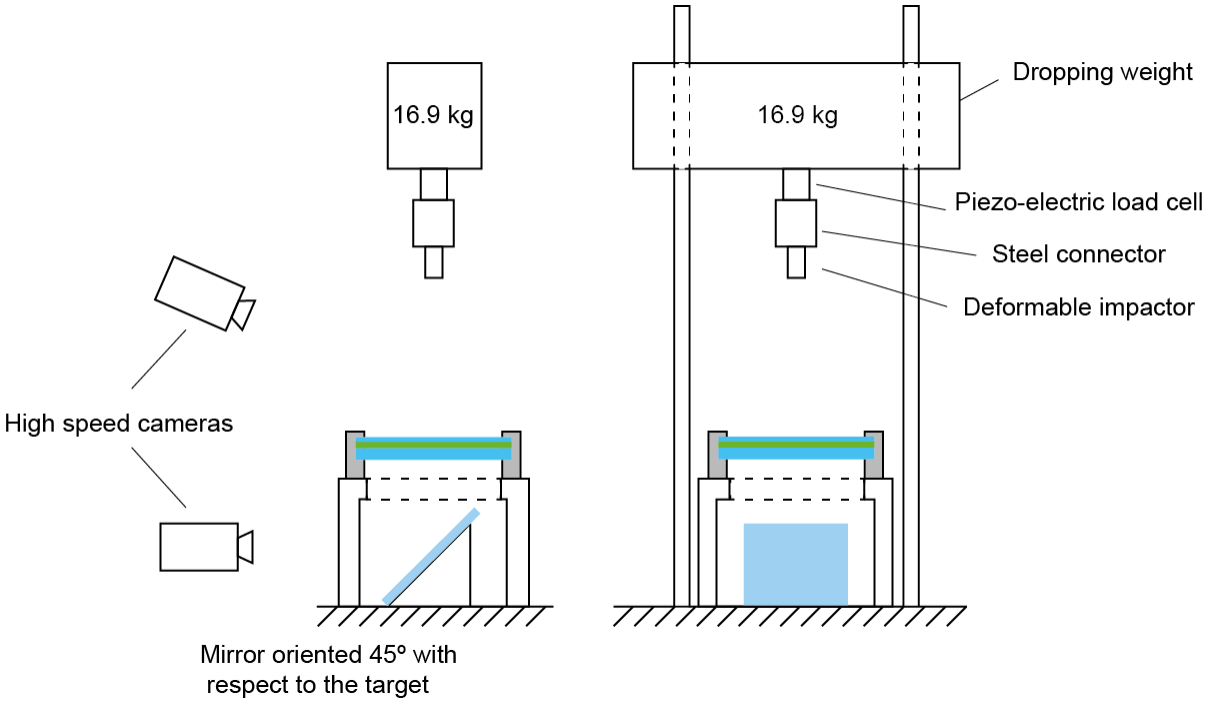

Figure 5-1. Schematic drawing of drop weight test set up.

To achieve the best performance and restrict unexpected variables, the specimen was held tightly enough to avoid vibration during the test. To achieve quantitative control of the compression force applied to the specimen, a metallic spacer and silicone rubber gasket were designed, as shown in **Figure 5-2**. As seen in the schematic drawing below, a metallic spacer 15 mm thick was applied. By controlling the silicone rubber's compression extent, subtracting from the original thickness, the compression force applied on the target laminated specimen was controlled as well. As demonstrated in **Figure 5-2**.b, the 10 mm thickness of the target

laminated specimen plus the 4 mm thickness of the silicone rubber gaskets on each side results in a total of 18 mm thickness from free bound. The 18 mm thickness was clamped in between metallic clampers with a confined metallic spacer 15 mm thick. Due to the thickness of the metallic spacer, the bolt could only be tightened to 15 mm. Rubber gaskets from both sides experienced a total of 3 mm deformation and distributed uniform compressive force along the periphery of the contacting interface between the specimen and clampers. The deformation from rubber was roughly 37.5% and related equivalent force applied onto the laminated glass. The silicone rubber sheet was 40 shore and had a Young's modulus of 70 MPa [81]. By varying the thickness of the metallic spacer, the related equivalent force could be controlled by percentage of deformation from the rubber gasket.

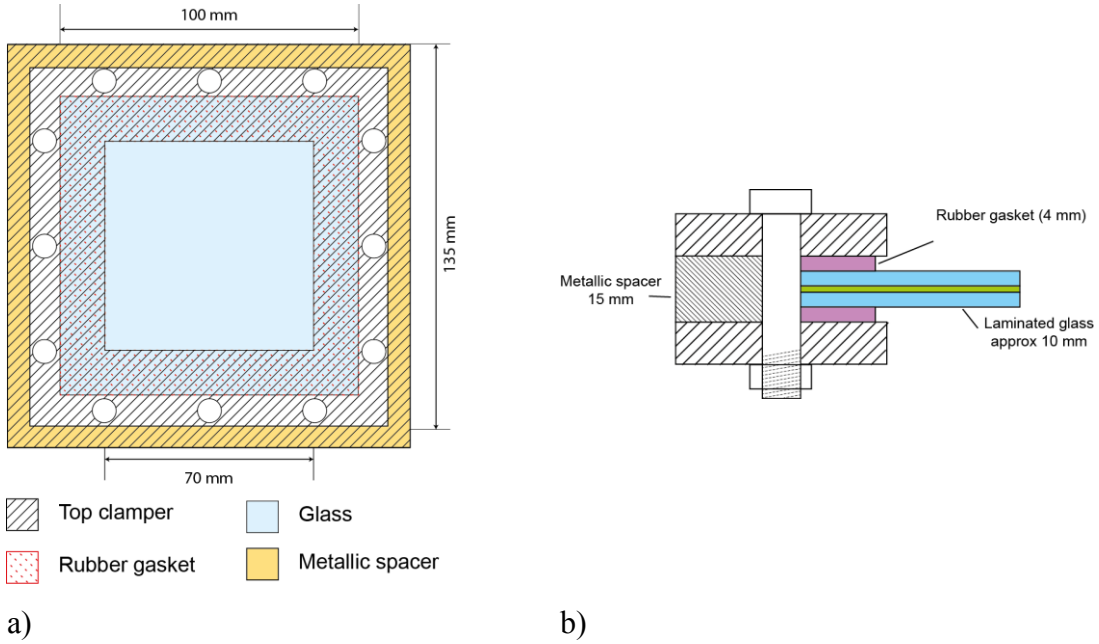

Figure 5-2. Clamping system for drop weight specimen: a) clamper design front view and b) clamper cross section view.

5.1.2. Uniaxial tensile setup for polymer interlayer at various strain rates

After glass plies have been broken, polymer interlayers can be still intact and act as the main bridging ligament against post-breakage impact. Polymer as a part of the laminated structure plays an important role in the overall mechanical response. However, from the point of view of design and safety, the backing glass ply should not be broken. Still, the understanding of this dynamic response at a large strain is necessary for the study of the ultimate bird strike and will provide materials for the later finite element simulation study in this project. The test conducted was between 0.00008 m s^{-1} and 8.33 m s^{-1}. For accuracy of the testing machine, the test was split into two parts: one test was conducted on a screw-driven machine between 0.00008 m s^{-1} and 0.008 m s^{-1}, and the other was conducted on a servo-hydraulic machine between 0.0833 m s^{-1} and 8.33 m s^{-1}.

5.1.2.1. Polymer tensile specimens for tensile tests

The specimen (dumbbell-shaped) was prepared following the ASTM D412-06a standard for polymer tensile tests [82]: gauge length 35 mm, gauge width 6.17 mm and specimen thickness 1.25 mm, as shown in **Figure 5-3**. All the specimens were cut from the polymer sheets provided on the available markets. The black parallel lines were used to track local strain inside the valid gauge length to get an accurate measurement from the specimen during the tensile test. The black parallel lines were 10 mm apart and made by black permanent marker pen marked inside the gauge length.

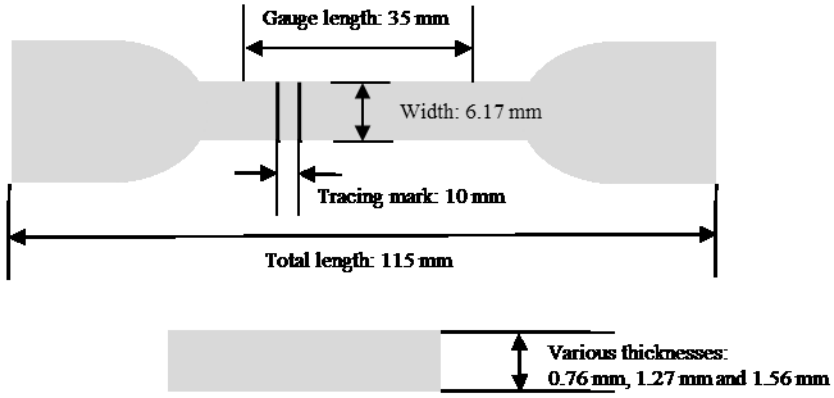

Figure 5-3. Configuration and dimensions of dumbbell PVB specimen.

5.1.2.2. Tensile test using screw-driven test machine

An Instron 5800 series screw-driven machine was used to load the polymer specimens in the tensile test. The test specimen was connected through two clamps connected to the actuator and 10 kN load cell on the Instron. The test machine was driven by a screw rack, which, by mechanical design, has a speed limit of 0.07 m s^{-1}.

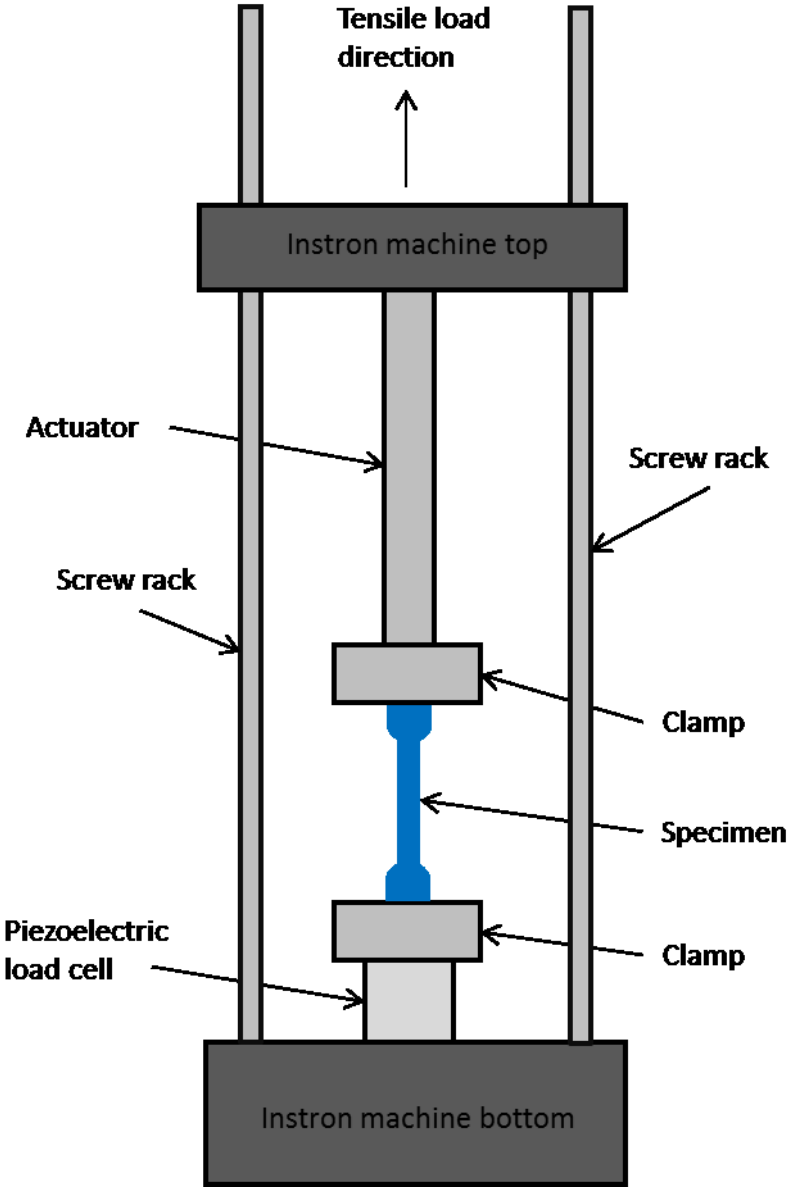

Figure 5-4. Polymer tensile test setup of screw driven test machine.

The specimen was connected to the Instron test machine by two clamps. Due to the load limit of the machine, the 250 kN capacity test machine has low sensitivity and a large fluctuation in

accuracy when measuring small loads. The maximum test load on the hardest specimen of SGP was approximately 350 N only. To improve the accuracy of the test results, the 250 kN load cell was replaced by a 10 kN load cell. This was the lowest load cell for the screw-driven test machine in the laboratory.

Table 5-1. Test speed, strain rate and number of polymer specimens at medium strain rate.

Test rate		Number of specimen		
Test speed (m s^{-1})	Equivalent initial strain rate (1/s)	TPU	PVB	SGP
0.0000833	0.00238	3	3	3
0.000833	0.0238	3	3	3
0.00833	0.238	3	3	3

The test for the screw-driven machine is listed in **Table 5-1**. The speeds tested were 0.00833 m s^{-1}, 0.000833 m s^{-1} and 0.0000833 m s^{-1}, three different speeds for PVB, SGP and TPU. Equivalent strain rate was converted for each test speed by dividing the valid gauge length of 35 mm (indicated in **Figure 5-3**). Three repeat tests were conducted for each of the polymer types.

5.1.2.3. Tensile test using servo-hydraulic test machine

An Instron VHS 8800 high-strain servo-hydraulic machine was used to load polymer specimens for the tensile test. The test specimen was connected through two clamps connected to the actuator and piezoelectric load cell (PCB 222B, 25 kN maximum load capacity, by PCB Piezoelectric Company) onto the Instron. The test machine has a working range of speeds between 0.07 m/s and 10 m/s.

The top part of the specimen was connected with a lost motion rod to the actuator on the Instron. The lost motion rod was used to guarantee the actual test happened at the correct speed chosen. This rod enabled the machine to accelerate before pull up specimen. Thin rubber washers were used in between the contact regions to dampen vibration from the impact and protect rigid-rigid damage to the test machine. The test temperature was controlled at 23 °C ± 5 °C due to the large open area in the testing lab.

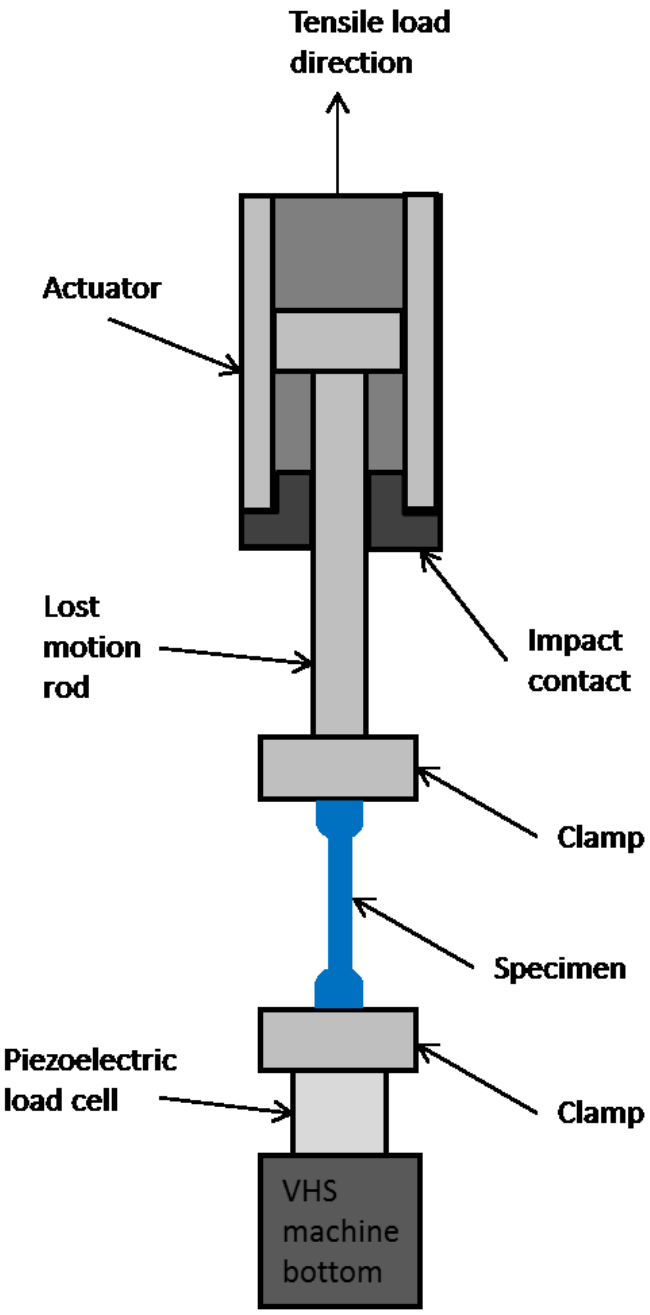

Figure 5-5. Polymer tensile test setup of servo-hydraulic driven test machine with lost motion rod.

The test for high strain rates is listed in **Table 5-2**. The speeds were tested at 0.0833 m s^{-1}, 0.833 m s^{-1} and 8.33 m s^{-1}, three different speeds for PVB, SGP and TPU. Equivalent strain rate was converted from the test speed by dividing the valid gauge length of 35 mm (indicated in **Figure 5-3**). Three repeat tests were conducted for each of the polymer types.

Table 5-2. Test speed, strain rate and number of polymer specimens at high strain rate.

Test rate		Number of specimens		
Test speed (m s^{-1})	Equivalent strain rate (1/s)	TPU	PVB	SGP
0.0833	2.38	3	3	3
0.833	23.8	3	3	3
8.33	238	3	3	3

5.1.2.4. Calibrated strain results using image correlation techniques for various tensile experiments

In the real scenarios, the dumbbell-shaped specimen was not permanently held tight by clamps while it experienced large tension from pulling. As the tests proceeded, the specimens slipped from the clamps differently depending on the extent of clamp force and test conditions. In some cases, the slippage would happen and affect the accuracy of strain measurements from the test machine. To minimize uncertainty from strain measurement, two methods were tried. One method was to use a pair of strong grips to improve the clamping. Two mechanical wedge-shaped grips were used on the screw-driven test machine. This type of grips gave optimum clamping force for the wedge-shaped holders. However, some of the soft polymer specimens were too thin to be tightly clamped with the grips, so extra folded soft polymer was added in between the griping gaps to increase thickness and maximize clamping force. Secondly, because of the slippage and potential operational errors (e.g., tightness of the clamping force applied on the clamps, specimen loading direction and clamping positions, temperature and environmental factors) from the test machine and operator, all the strain data was measured externally using a non-contact line tracking technique. The technique used to capture local strain changes is from Imetrum video gauge software; it allows local strain to be tracked by monitoring changes to the parallel lines drawn 10 mm apart on the polymer specimens, as shown in **Figure 5-6**. The accuracy of the strain measured was compared to a calibrated strain gauge (valid reference) by Imetrum. The differences in the results from these two methods were within 0.5% [83].

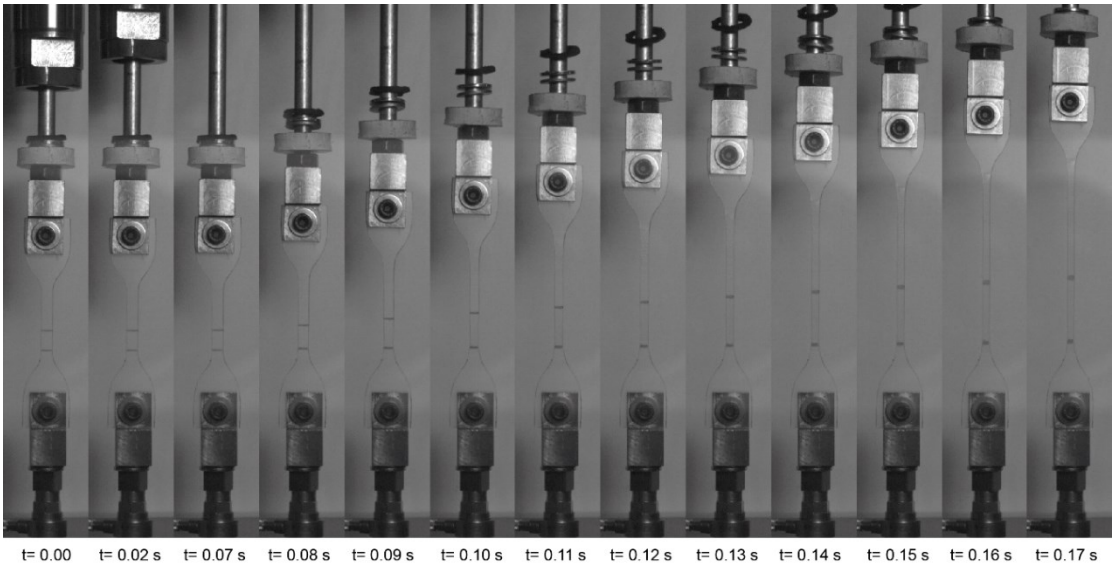

Figure 5-6. Example of servo-hydraulic test for polymer tensile test using video extensometer and high-speed camera.

Data acquisition of non-contact strain measurements for the hydraulic and screw-driven tensile tests were slightly different. For screw-driven tests, a non-contact video extensometer with a maximum of 15 frames per second was sufficient for the test requirement. For the high strain rate test, a larger number of frames per second was needed (roughly 1000 frames per second). Thus, a high-speed camera was used to capture videos, and non-contact video extensometer software was used for video and data analysis.

5.2. Result and discussion

5.2.1. Various strain tensile results for PVB, SGP and TPU

Various true strain stress results for PVB, SGP and TPU were obtained from the screw-driven Instron test machine at 0.000238 s^{-1}, 0.00238 s^{-1} and 0.238 s^{-1} and the servo-hydraulic Instron test machine at 2.38 s^{-1}, 23.8 s^{-1} and 238 s^{-1}. **Figure 5-7** a, b and c show the summary of calibrated true stress versus true strain at different strain rates for PVB, TPU and SGP, respectively. A clear strain rate dependent on all three types of polymer is observed from the figures. For reasons of continuity, the results only show up to 0.8 strain.

The summary of calibrated true stress versus true strain of TPU in **Figure 5-7**.a, curves for all strain rates, clearly showing hyperplastic material behaviour with large non-linear deformation throughout the whole range until 0.8 strain.

Strain rates 0.000238 s^{-1}, 0.00238 s^{-1} and 0.238 s^{-1} from the summary of calibrated true stress versus true strain of PVB in **Figure 5-7**.b clearly show hyperplastic material behaviour with large non-linear deformation throughout the whole range until 0.8 strain. As the strain rate increased, the PVB stiffened and transferred to elastic-plastic material. Linear gradients appeared in these higher strain rates of 23.8 s^{-1} and 238 s^{-1}, in which the linear region grew with the raising of strain rates at higher rates. Viscoelastic PVB consists of elastic and viscous parts. Elastic part is instantaneous and viscous part over time period. Because of this, for low strain rates, the viscous part of the mechanical response is more pronounced (for example, at 0.000238 s^{-1}, 0.00238 s^{-1} and 0.238 s^{-1}) whereas the elastic response is noticeable once higher strain rates are performed (2.38 s^{-1}, 23.8 s^{-1} and 238 s^{-1}). This is what causes the linear gradients.

The summary of calibrated true stress versus true strain of SGP in **Figure 5-7**.c shows viscoelastic material behaviour throughout the whole strain rate under the glassy phase, which was proved in the previous section on DMA results. It has a linear elastic region for all strain rates tested and the gradient is higher than that of PVB at equivalent high strain rates as well. This proves the rigidity of this polymer type and its distinguishable functionality in the structural performance of laminated glass that has been employed.

The noticeable phenomenon is that by increasing strain rate, PVB effectively shifted from rubbery-behaviour material to viscoelastic material by having glassy elasto-plastic behaviour with the linear initial gradient. All of this happened at room temperature, which is in the glass

transition temperature range. This also reveals that the ultimate stress required to break PVB will increase with an increase in strain rate, which benefits the laminate structure at high strain rates. Due to the technique limit from image tracking, the strain range was only shown from 0.0 to 0.8. Regarding the sufficiency of strain range, assume specimen has 70 span of length with 5 mm maximum bending displacement shown in **Figure 5-9**.c. Using trigonometry, we can work out the approximate strain on that was 1 % and 1 s^{-1} for 10 ms.for example from **Figure 5-9**. The tested strain range in **Figure 5-7** covers all the strain rates needed.

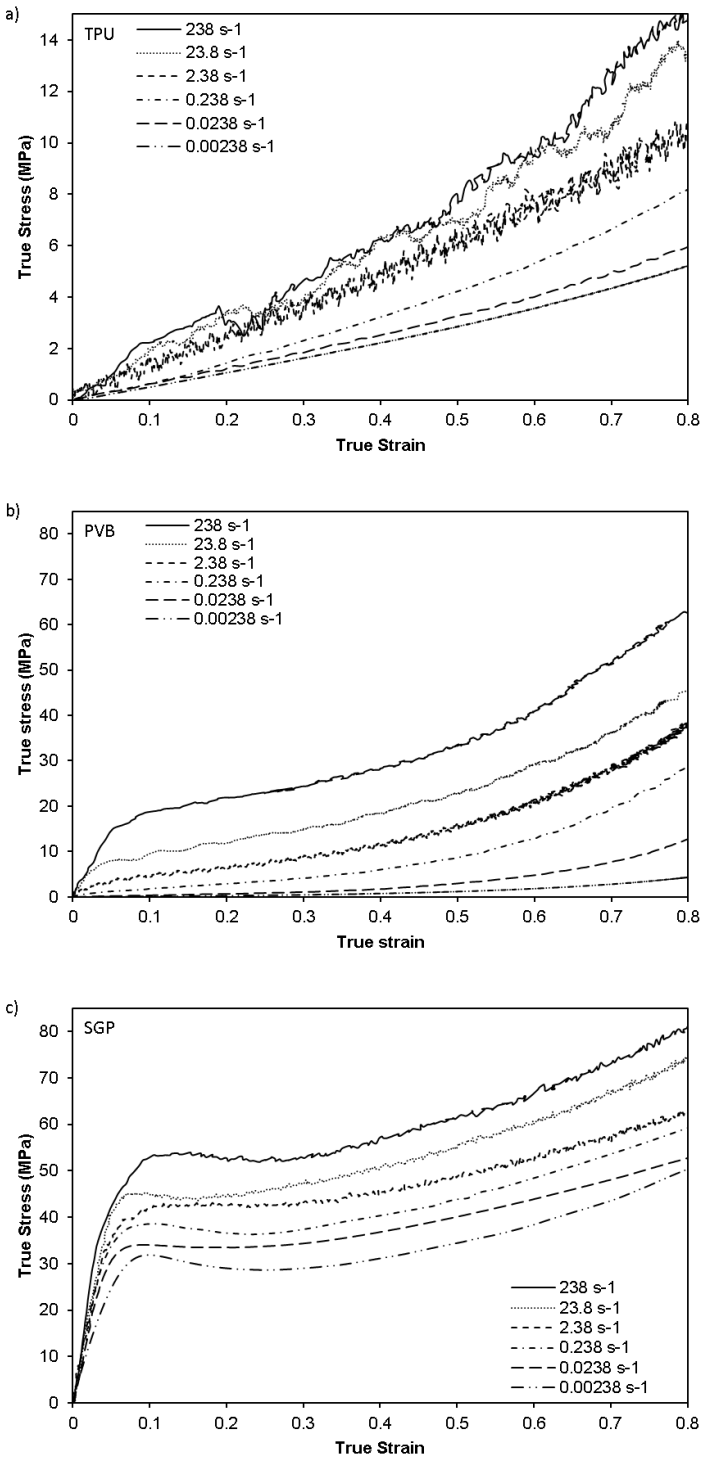

Figure 5-7. True strain stress results for PVB, SGP and TPU at 0.000238 s^{-1}, 0.00238 s^{-1} and 0.238 s^{-1}, 2.38 s^{-1}, 23.8 s^{-1} and 238 s^{-1}.

5.2.2. Drop weight results

As previously mentioned, one camera was filming from the top of the specimen and the other camera was placed at the bottom, filming through a 45° mirror to monitor laminated glass back-

face deformation and fractography under the impact. **Figure 5-8** shows an example of the image series extracted from C3. From the experimental design, the rubber impactor should impact at the centre of the specimen. A cross mark was drawn at the centre of the specimen before the test started. This was used as a reference to confirm the rubber impacted at the specimen's centre. The onset of contact between the rubber impactor and glass specimen was at t = 0 ms. One image was extracted before the start point at t = -4.54 ms to describe the mechanical behaviour of drop weight before contact. From the onset of contact (t = 0 ms), a series of seven consecutive images is shown with equal time intervals (3.64 ms) until failure of both glass sides. A clear coincidence between rubber and the cross mark was confirmed and proved that the rubber hit the centre of the specimen at t = 0 ms. During the loading process, the rubber deformed extremely due to impact momentum. Uniform and distributed load was accumulated onto the laminated glass impact glass face (2.2 mm glass side) until the specimen was broken. The facture sequence of impact glass side (2.2 mm glass side) and back glass side (4.0 mm glass side) was difficult to tell from the fracture images of the high-speed videos in **Figure 5-8**. However, from the bottom view, both radial and circumferential crack patterns were observed.

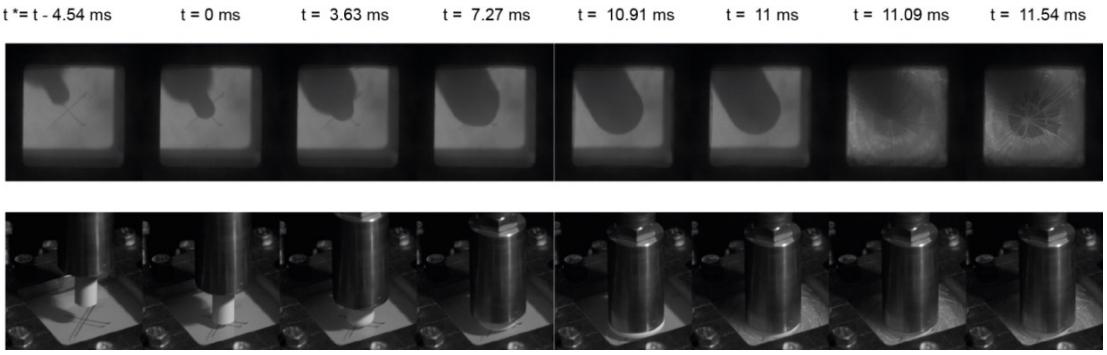

Figure 5-8. High-speed cameras' images taken from both top and bottom view of C3 (using TPU) to monitor mechanical behaviours of laminated glass and rubber.

5.2.2.1. Consecutive drops with constant increment of height for each configuration

For the drop weight test, only force versus time curves of different drop heights for laminated glass C1, C2, C3, C4, C5, C6 to C7 and C8, the 6 mm monolithic chemically toughened glass

(CG) were collected. Displacement information corresponding to the force and time is unknown. These force versus time curves at breaking height for different laminated configurations were interpreted to obtain force versus displacement in order to work out energy terms for those broken specimens. Based on the force versus time curves, velocity and displacement were calculated to help calculate the fracture energy used to break each laminated configuration.

Taking C3 with breaking height 40 cm as an example, as shown in **Figure 5-9**, the force versus time curve in **Figure 5-9**.a illustrates C3 with fracture of both impact and back glass plies. To work out fracture energy from the force versus displacement curve, velocity and displacement are needed. According to Newton's second law of motion, the total vector summation of the forces applied on the drop weight is equivalent to the mass of the drop weight (16.9 kg) multiplied by the net acceleration vector on the drop weight. Velocity (v_f) can be converted using Newton's laws and kinematic equations as follows:

$$v_f = \int a(t)\, dt + v_i \qquad \textbf{Equation 5-1}$$

where a(t) is the acceleration based on the force and time variations and v_i is the initial velocity when the drop weight makes contact with the testing specimen.

For each fixed drop height and before the impact started, v_i, as the initial velocity, is known by using the certain drop height (h) and gravity (g):

$$v_i = \sqrt{2 \times g \times h} \qquad \textbf{Equation 5-2}$$

From the integration from infinitesimal elements of the acceleration and time data according to **Equation 5-1**, a typical velocity versus time curve was obtained, as shown in **Figure 5-9**.b. Displacement (d_f) was extracted based on the obtained velocity profile using the following relations:

$$d_f = \int v_f(t)\, dt + d_i \qquad \textbf{Equation 5-3}$$

where v_f is the velocity-time profile deducted from the previous equation, d_i is the initial displacement counting from the beginning of impact in between the drop weight and the testing specimen. In this test, we consider zero displacement before any impact; thus d_i is zero. With integration from infinitesimal elements of the acceleration and time data according to **Equation 5-3**, a typical displacement versus time curve was obtained, as shown in **Figure 5-9**.c. The plot of force versus displacement for C3 at 40 cm fracture height is shown in **Figure 5-9**.d and the corresponding area underneath the curve is the fracture or impact energy used to break the specimen.

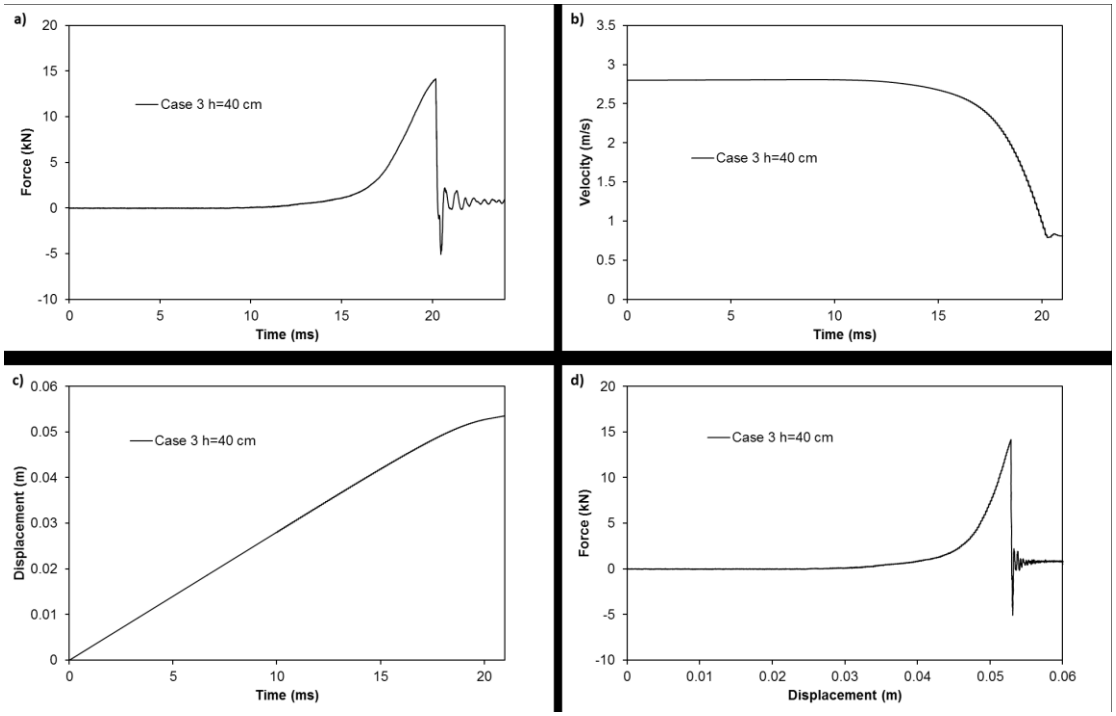

Figure 5-9. Conversion and calculations of energy required to break specimen at C breaking at 40 cm height using force versus displacement curve (area underneath the curve). a) force vs time curves; b) velocity vs time curves; c) displacement versus time curve; and d) force versus displacement curve.

5.2.2.2. 6 mm monolithic CG and laminated glass drop weight results

Tests were conducted with constant weight (16.8 kg) and started at 10 cm with 5 cm increment increases each time until the specimen broke. Below is a set of force versus time traces recorded for the 6 mm monolithic CG in **Figure 5-10**.a. The fracture height was 55 cm and both glass plies were broken. As the height increased, the peak force corresponding to each drop height was raised. Complete impact duration (contacting time) of rubber and specimen during the impact was calculated from each height from each curve. Both peak force and contact time of specimen were plotted in **Figure 5-10**.b except the contact time at 55 cm. At 55 cm, peak load was plotted but contact time was not, as the specimen fractured. The result of peak load (y) versus drop height (x) for 6 mm monolithic CG shows a linear relationship of $y = 0.4041x + 0.8269$. The result of contact time (y') versus drop height (x') for 6 mm monolithic CG shows a secondary order polynomial relationship of $y' = 0.0091x'^2 - 0.8514x' + 31.91$.

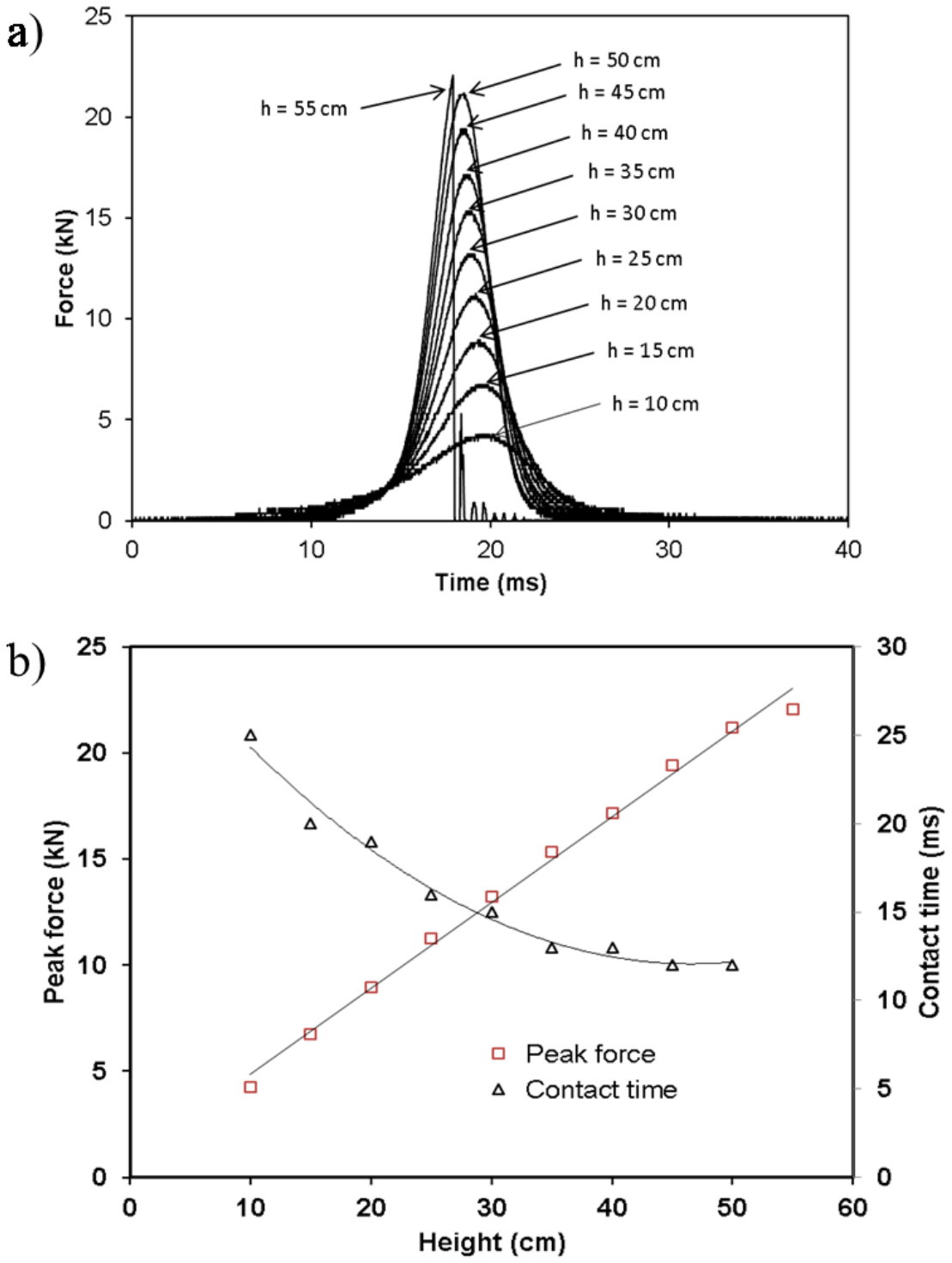

Figure 5-10. Drop weight results for 6 mm monolithic chemically toughened glass of drop weight results for 6 mm monolithic chemically toughened glass of a) accumulated force versus time curves from 10 cm with 5 cm increment until 55 cm fractured both glass plies; b) corresponding peak force and contact duration measured and summaried based on result from a).

5.2.2.3. Thermal plastic polyurethane (TPU) thickness influence on the impact performance

There was a significant influence of the thickness of TPU from the structural performance. Because of the condition of keeping all the glass geometric and physical conditions the same in C1, C2 and C3, the only variable amongst the three cases was the thickness of TPU: 0.76 mm for C1, 1.27 mm for C2 and 3.18 mm for C3. Based on the fracture heights for the three cases, the impact energy was calculated. A comparison of the impact energy versus TPU thickness is shown in **Figure 5-11**. The data in the figure correspond to the schematic drawing of C1, C2 and C3 (same glass but different TPU interlayer thicknesses). C1 fractured at 30 cm, C2 fractured at 35 cm and C3 fractured at 40 cm. Due to the scattering of mechanical performance from monolithic glass plies, deviation bars were added to assess impact energy values for C1, C2 and C3. A continuous improvement in terms of impact energy is shown in **Figure 5-11** as the TPU thickness increased to 3.18 mm. This proves that the impact resistance performance will be improved if the thickness of TPU interlayers increase. Due to the limit numbers of the test specimens, what the optimal thickness is and how to define the thickness parameters for lamination are still questions that require further study.

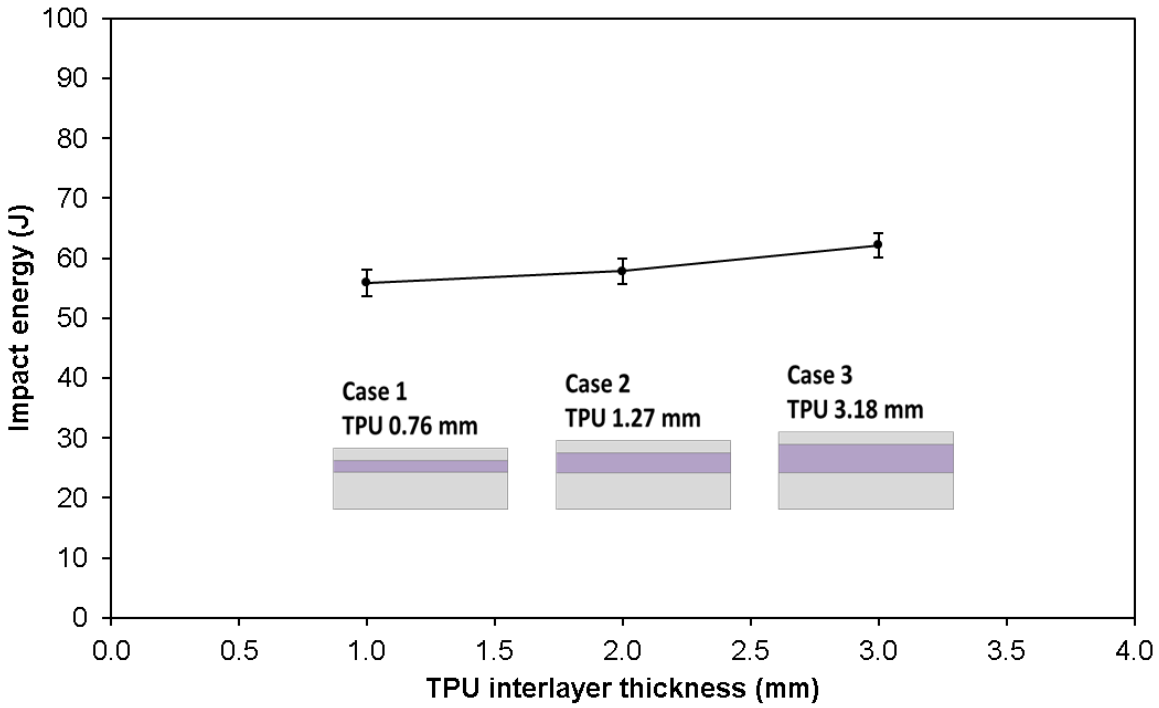

Figure 5-11. TPU interlayer thickness versus impact energy for C1, C2 and C3 with deviation bars.

5.2.2.4. Effect of polymer type on impact resistance performance

After studying the dynamic behaviour of polymer interlayers, **Figure 5-12** shows the structural performance comparison of polymer interlayer types in C3, C5, C6 and 6 mm monolithic CG. C3, C5 and C6 have the same dimensions but different polymer interlayers of TPU, SGP and PVB, respectively. An additional equivalent-thickness 6 mm monolithic glass is compared as well. From **Table 3-1**, C3 has a small variation of 3.18 mm thickness comparing with 3.04 mm for SGP and PVB in C5 and C6, due to limited commercial availability of SGP thicknesses in the market.

In general, all cases show similar fracture energy of area underneath force versus displacement curves at fracture, shown in **Figure 5-12**. a and b. However, they fractured at different heights: C3 at 40 cm, C5 at 70 cm, C6 at 45 cm and monolithic 6 mm CG at 50 cm. C5, using SGP, showed significant improvement of impact resistance against a higher drop height, compared with the lamination using PVB and TPU at a similar thickness range and monolithic 6 mm CG. A closer look at the polymer properties helps us to understand the difference. Typical polymer tensile results of SGP, PVB and TPU have been introduced in the previous section. The glass transition temperature (Tg) for different polymer interlayers is different, and this results in distinguished mechanical behaviour in corresponding operating environments (Tg is 55C for SGP, 21C for PVB and -41C for TPU). At room temperature, SGP is in its glassy state, compared with a rubbery state for both PVB and TPU. Even more, at room temperature, SGP obeys elasto-visco-plastic behaviour and acts as a solid. Thus it allows more shear force to be transferred through the rigid interlayer, making laminated glass using SGP stronger and offer a better impact resistance in performance in general. Both PVB and TPU follow hyper-elastic behaviour and operate in a rubber state.

However, the fracture patterns of C3, C5 and C6, shown in **Figure 5-12**.c indicate two different post-breakage situations: C5 using SGP shows complete rupture throughout the whole lamination, and large glass fragments peeled off; whereas cases using TPU and PVB still held most of the fragments but did not behave as strongly as C5 using SGP. Laminated glass using the SGP interlayer enhanced impact performance based on experimental results. However, it may lead to catastrophic failure after its impact limit, as shown in **Figure 4-12**.c, which tore the whole lamination apart.

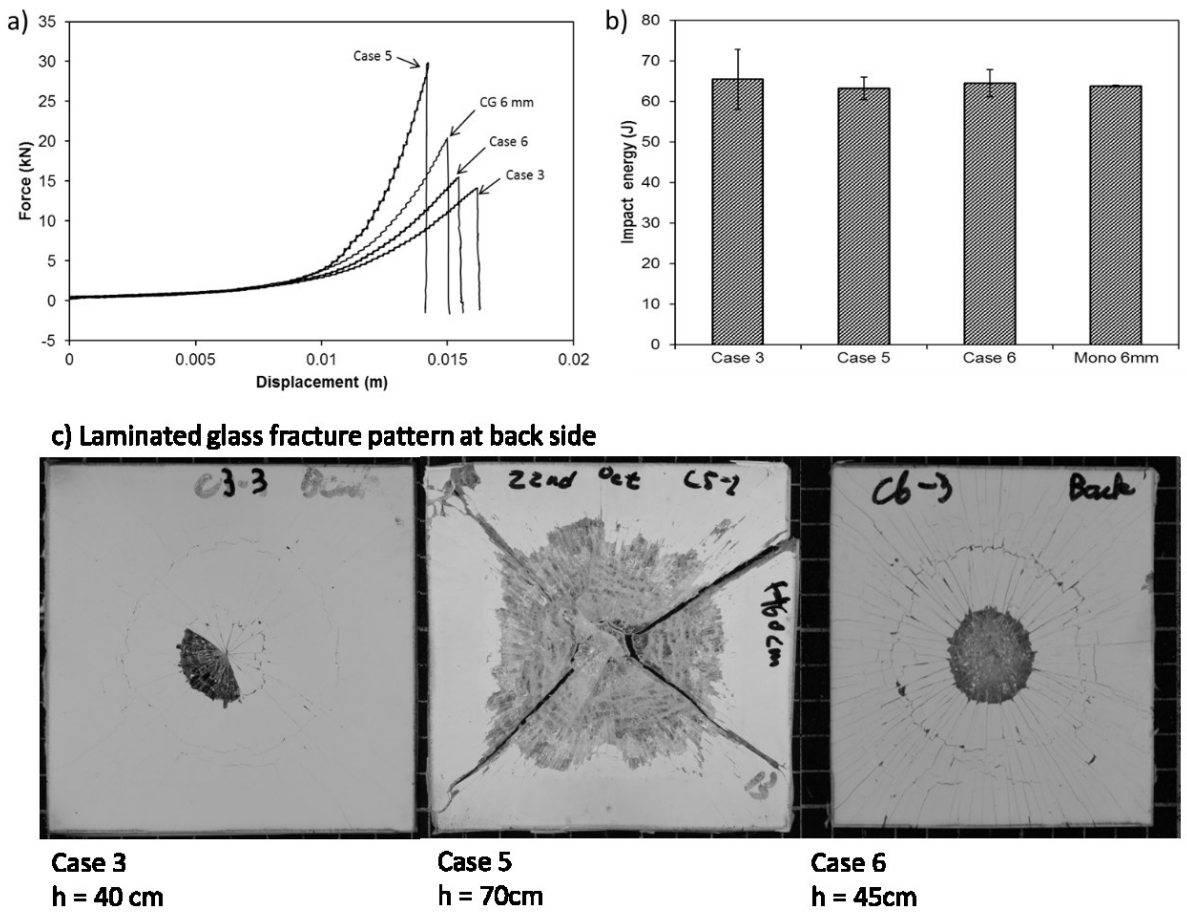

Figure 5-12. Drop weight structural performance of a) force versus displacement for C3, C5, C6 and C8 (CG 6 mm), b) impact energy comparison from the area underneath the curves and c) fracture pattern after specimen fractured.

5.2.2.5. The effect of glass type on impact resistance performance

C3 and C4 had the same laminate configurations and materials except for different strengthening treatments on the front glass ply; C3 used chemically toughened glass and C4 used thermally toughened glass. The tests were carried out in such a way that the test stopped whenever any glass ply broke. For C3, both front and bottom glass layers broke at almost the same time (the sequence was hardly distinguishable from the high-speed videos). In contrast, the thermally toughened top glass layer from C4 broke at a very early stage, but the whole structure could still carry the load and kept its functionality. Another test was carried out until the second layer of C4 broke, which is the third column in **Figure 5-13**. The energy taken to break C3 and C4 completely was comparative. Although the thermally toughened glass layer broke at an early stage, the front layer could act as a sacrificial layer and the whole structure could still be used safely.

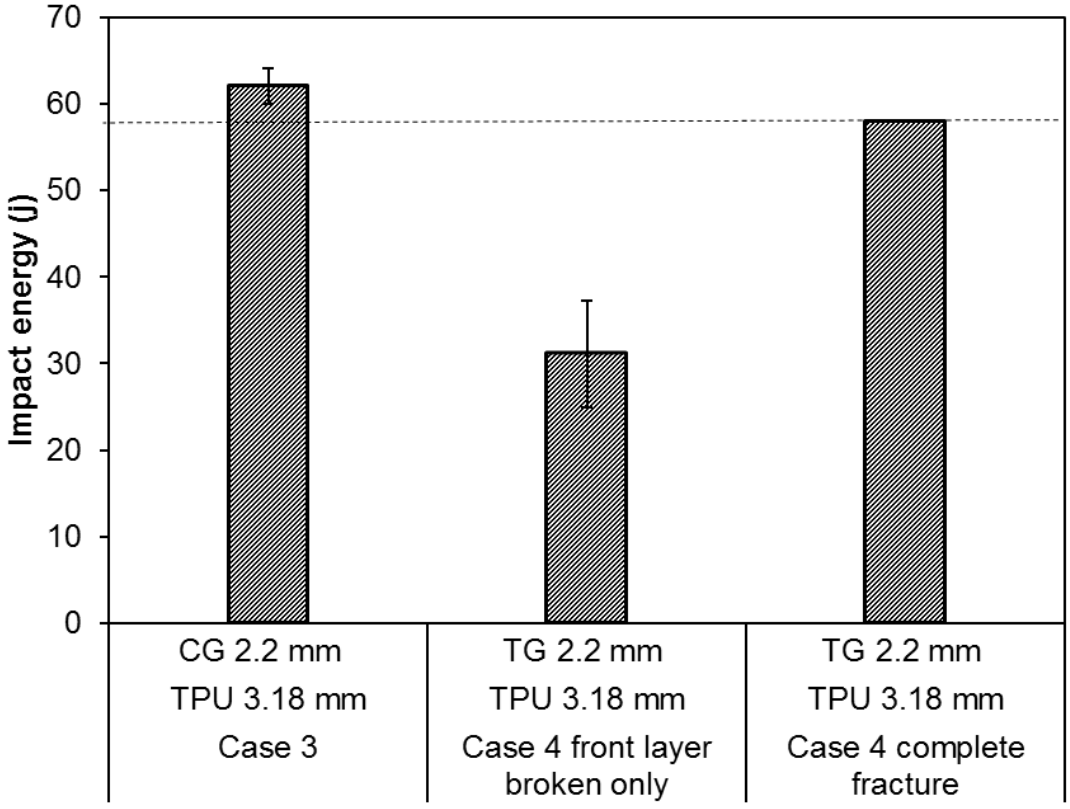

Figure 5-13. Impact resistance performance comparison for C3 and C4 (front layer broken only and complete fracture).

5.2.2.6. The effect of multi polymer interlayer on impact resistance performance

Based on the previous introduction and literature research, modern aircraft from both Boeing and Airbus are using multi-interlayer structures for part of their windshield designs, which is similar to C7 in this study, which has 2.28mm SGP for major interlayer and 0.38mm TPU as an adhesive layer between the glass and SGP. However, from ring loading and soft load results in the previous section, this structure showed normal performance amongst other cases, and there was no good explanation for using a multi-layered structure. One thing that was confirmed from the previous ring-on-ring test was that there were two clearly distinguished stages of fracture. The fractures occurred at a time delay on fracturing front-loading 2.2 mm glass ply and back-supporting 4.0 mm glass ply from previous load versus displacement curves for both ring loading and rubber loading at a quasi-static level. However, in low-velocity impact tests, this did not happen for all the configurations. Only C7 in force versus displacement curves from **Figure 5-14**.a showed two clear stages of fractures with a time delay. This was not a coincidence: it happened in all five repeat tests for C7 and not in other cases. The special feature of this multi-polymer interlayer structural design increased the chance of having a two-stage fracture mechanism at low-velocity impact. Also, in the comparison of the impact energy in **Figure 5-14**.b, the absorbed energy caused by the two-stage fracture mechanism was indeed the highest amongst all cases with the same configuration.

Additionally, comparing laminated glass with monolithic glass, 6 mm monolithic glass has impact energy equivalent to C5 but experiences complete fracture and potential further damage from glass fragments flying off post-breakage. This proves why a large laminated structure was applied in the application rather than monolithic glass. In general, a laminated glass case is essential, compared with monolithic glass, for preventing further damage from fragments flying off.

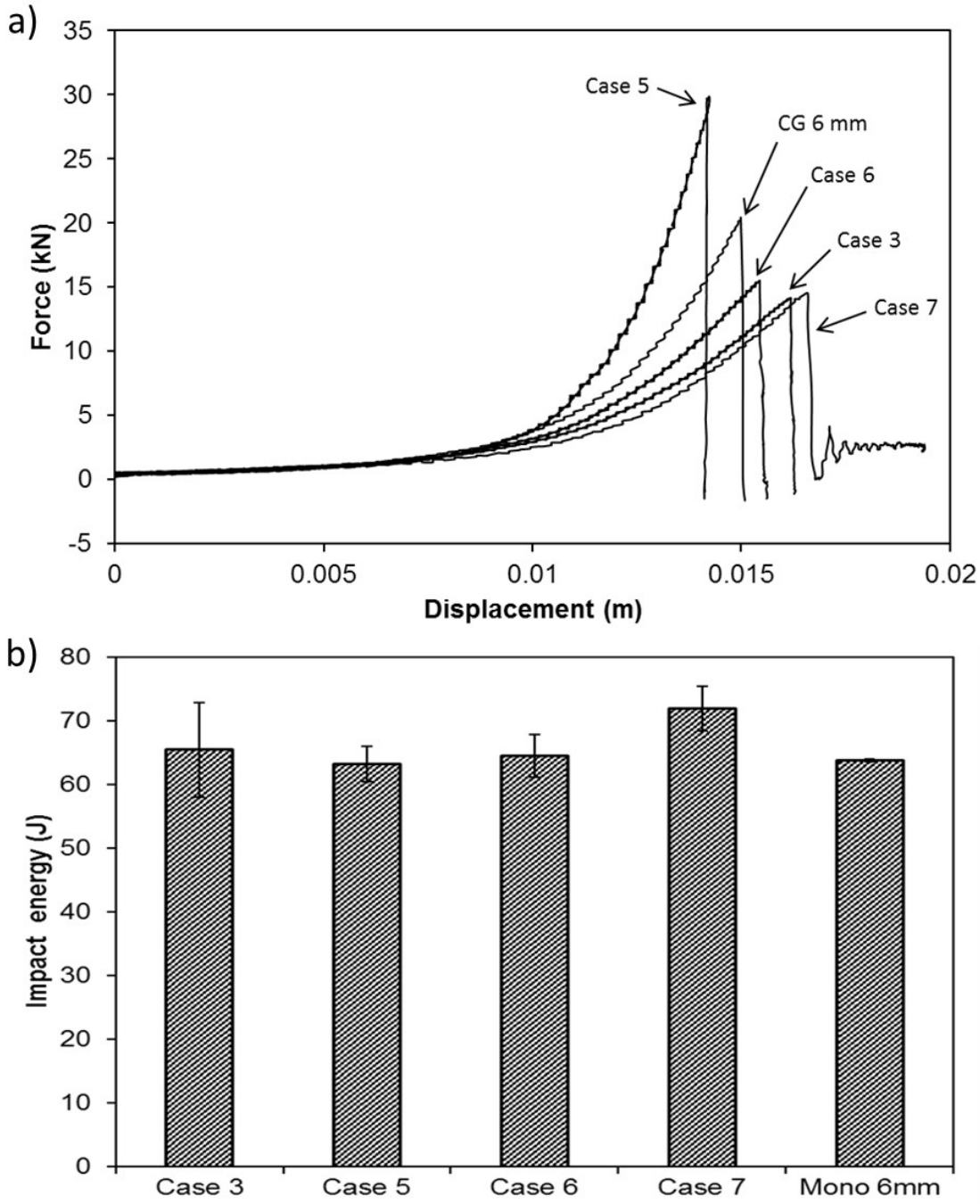

Figure 5-14. Drop weight structural performance of a) force versus displacement of one impact energy for C3, C5, C6, C7 and C8 (CG 6 mm) and b) breakage energy comparison from the area underneath the curves.

5.2.2.7. Comparison of results from drop tower and coaxial ring compression.

C1, C2 and C3 illustrate the effect of TPU polymer thickness. Both drop tower and soft rubber loading results shown in **Figure 5-15** show an increase in impact energy as the thickness of the polymer interlayer increased. For ring rigid loading, although C2 was slightly lower than C1, as the polymer thickness increased to 3.18 mm in C3, the structural performance became much better in terms of impact energy. Therefore, an increase in polymer thickness will lead to better structural performance.

C3 and C4 illustrate the effect of the glass type used on the impact side. For both low velocity and quasi-static tests, chemically strengthened glass performed better compared to thermally strengthened 2.2 mm glass from the loading/impact side.

C3, C5, C6 and C7 illustrate the effect of polymer types on structural performance in terms of impact energy from force versus displacement. For drop weight tests, as explained previously, C7 showed a different mechanical behaviour at low velocity compared to that at the quasi-static level. In contrast to C7, C3 and C5 had good performance at both quasi-static and low velocity. As previously introduced, PVB effectively shifted from behaving as a rubbery material to viscoelastic material by having glassy elasto-plastic behaviour with a linear initial gradient once the strain rate increased. C3, using PVB, can transfer more shear stress if the strain rate allows PVB behave more rigid. Fore C5, SGP has glassy behaviour at room temperature, and as previously demonstrated in the experimental proof, although the impact energy was not outstanding amongst others, all the C5 tests broke at much higher drop heights in general. The only drawback of using SGP was that it may end in catastrophic failure with no further protection post-breakage.

Comparing energy between quasi static and drop tower tests in **Figure 5-15**, more than doubled energy was consumed on drop tower test. This can due to different testing conditions: specimen sits freely on the test rig for quasi static experiments whereas a fully rubber compressed confinement was applied for drop weight experiments; testing velocity and loading condition were different. PVB is a rate dependent material and will change behaviour as strain rate increases. Boundary condition itself can be a research subject and will leave this discussion open for future study.

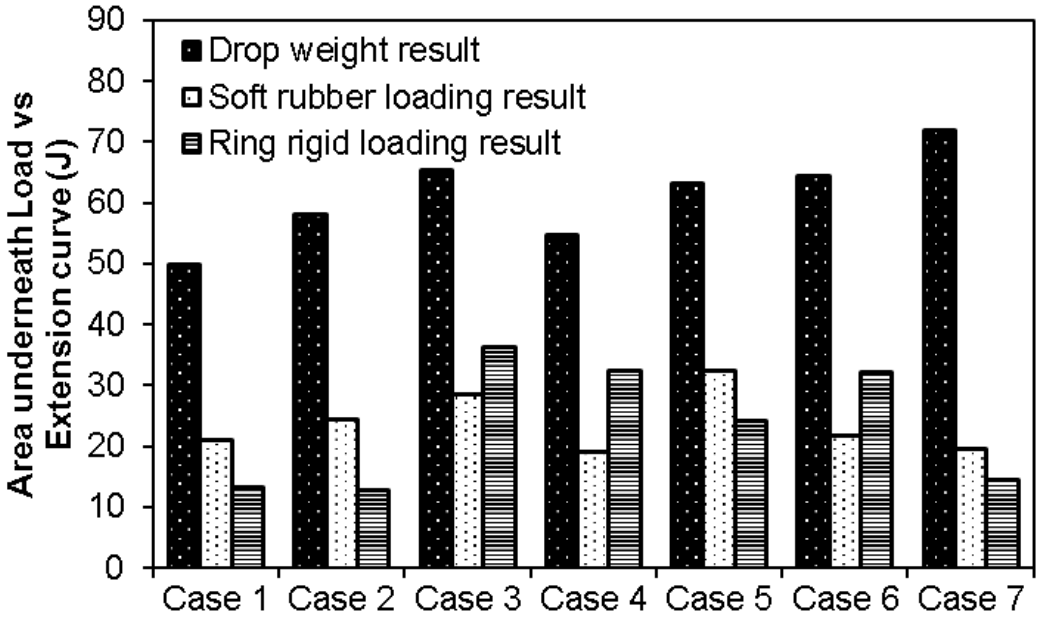

Figure 5-15. Impact energy comparison from the area underneath force versus displacemen curves of drop weight, ring loading and soft loading tests.

5.3.Conclusion

Overall, there are several conclusions can be summarized from this chapter.

- Polymer thickness has an effect on structural performance in terms of impact energy. C3, using thicker TPU, definitely has a better performance compared to thinner interlayers in C1 and C2.
- Due to different polymer mechanical behaviours from true stress strain results, C3, C5 and C6 had different structural performances in terms of fracture pattern and impact energy. C5, using SGP, survived at higher drop heights amongst all configurations due to its distinguishable viscoelastic material behaviour from the high modulus of linear elastic stress strain regions with high rigidity, compared to those from PVB and TPU. However, C5 failed at a much more catastrophic fracture pattern and could not maintain post-breakage functionality after impact. Between C3 using TPU and C6 using PVB, laminated glass using TPU had a better structural performance in terms of impact energy. However, one noticeable phenomenon was that PVB effectively shifted from rubbery behaviour material to viscoelastic material by having glassy elasto-plastic behaviour with a linear initial gradient. All this occurred at room temperature, which is in the glass transition temperature range. This also indicates that the ultimate stress required to break PVB will increase with an increase in strain rate, which benefits the laminate structure at high strain rates.
- From the results of C3 and C4 using chemically and thermally strengthened glass respectively, the 2.2 mm front impact glass ply with chemically strengthened treatment had much better structural performance.
- The performance of C7 definitely showed better structural performance with higher impact energy by applying a multi-polymer interlayer. Interestingly, two stages of breakage allowed the structure to absorb more energy before breaking.

6. Impact performance of laminated glass at high velocity

The aim of this chapter is to investigate the effect of the type of polymer interlayer on the soft impact response of laminated glass. Sabot design, experimental setup and structural performance for high-velocity impact are described in the following sections.

6.1. Method

To investigate the performance of laminated glass plates under bird strike, lab scale impact experiments were performed using a gas gun apparatus up to the velocity of 180 m s^{-1} (648 km hr^{-1}). This is a relevant velocity range, as most of the strikes occur during take-off or landing [84].

6.1.1. Design and preparation of projectile

While normally real birds are used in the industry to assess the impact performance of laminated glass windows, gelatine and rubber have also been employed as substitute materials for birds and have been demonstrated to create pressure profiles similar that of a real bird [68]. The use of these substitute materials has several advantages, including better repeatability and more control of orientation, homogeneity and isotropy of the projectile compared to using a real bird [68]. In this study RTV rubber, Mold Max ® 10T, was used, which has a density of 1.09 g/cm^3. Cylindrical projectiles, with flat faces, were made by mixing two liquid components provided by a supplier and casting them into steel moulds. The moulds were then left in the vacuum chamber for curing and de-airing. The final projectile had a diameter of 23.5 mm and length of 50 mm. This makes the aspect ratio of projectile diameter over its length greater than two, as is recommended in the literature for activating a steady-state flow regime for the impact of soft projectiles [67].

The rubber projectile is very soft and deformable and can be jammed inside the barrel if it is fired directly without any sabot or carrier. A special handmade sabot was made by wrapping two layers of rigid transparent polystyrene film around a hard cylinder so that the inside

diameter was controlled. The back was attached and sealed to 2 mm thick PMMA discs, which were laser-cut. The produced sabot was very light (4.0 g) and had very thin walls (0.6 mm). The sabot can be seen in **Figure 6-1**.a. The rubber projectile was then placed inside the sabot and both were fired together at the target. This was done with the assumption that the effect of the sabot deformation, damage and failure on the glass is negligible. The length of the projectile is slightly longer than that of the sabot, which means the projectile always comes into contact with target first. The interaction of the rubber projectile with a 5 mm aluminium plate, which is painted in black for better visualisation, is shown in **Figure 6-1.**b. During its interaction, no part of the sabot made contact with the glass (as shown in **Figure 6-1.**b). Also, before firing the projectile, three scratches were made on the sabot, which helped it open up more easily when the projectile expanded radially (**Figure 6-1.**b).

(a)

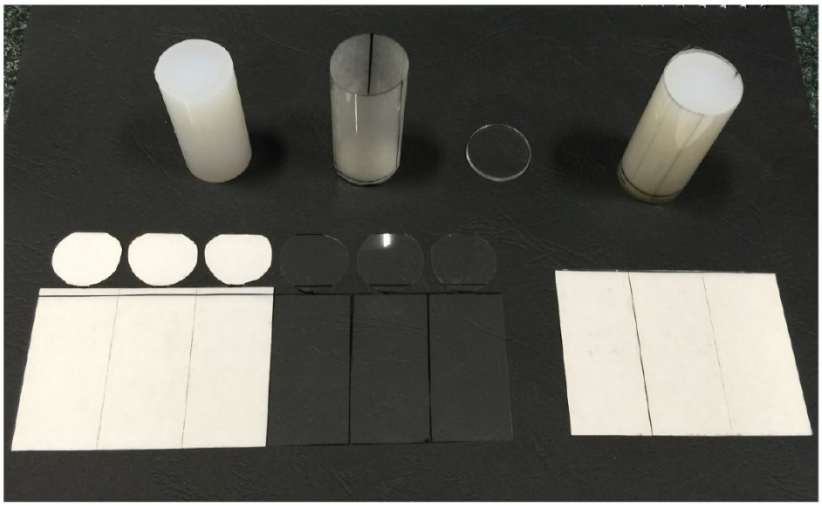

(b)

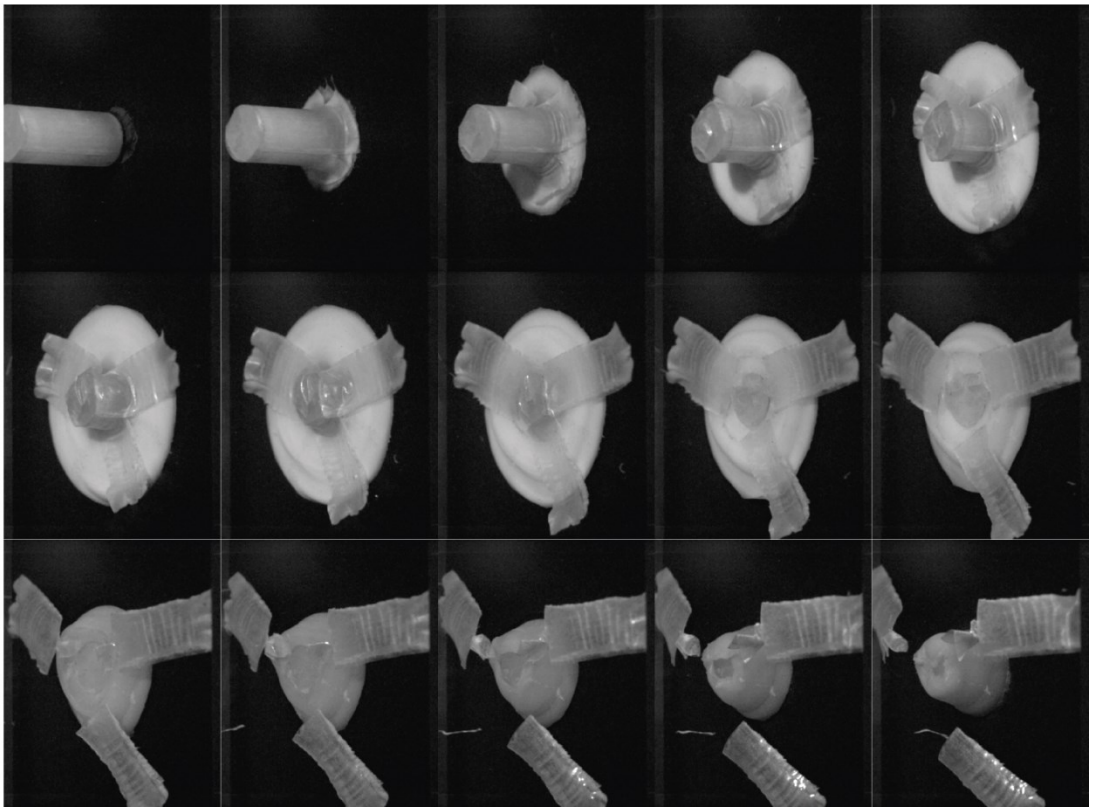

Figure 6-1. (a) Manufacturing of thin-walled, light-weight carrier for a silicon rubber projectile. (b) Interaction of the projectile and its carrier with a 5 mm Al alloy plate. The plate is painted in black to better visualise the deformation of the projectile.

6.1.2. Experimental setup

As noted earlier, a gas gun apparatus was used to achieve high-velocity impacts. Helium gas was used to feed a 4 litre cylinder to pressures up to 10 bar. The projectile was accelerated through a 3 m long barrel by opening a pneumatic valve. The velocity of the projectile was measured by two IR sensor pairs located at the end of the barrel. A series of calibration tests were performed using a high-speed camera aligned with the travel direction of the projectile. A good agreement was observed between the speeds obtained from the two methods. The target was located inside a safety chamber to protect the surrounding area from the flying fragments caused by impact. The side doors were made from thick polycarbonate panels to help with observing the impact event as well as illuminating the target. A schematic and picture of the gas gun setup is shown in **Figure 6-2**.

In order to measure the deformation of the laminated glass specimen, high-speed 3D digital image correlation (DIC) was used. Two synchronised high-speed cameras (Phantom Miro M/R/LC310) were located at the back of the target chamber (**Figure 6-2**). The cameras were recording the deformation of the target at 40,000 frames per second. A pair of identical Nikon lenses with a fixed focal length of 50 mm was used for both cameras. The two cameras were separated from each other by 410 mm and were 925 mm from the centre point of the target. This created an angle of approximately 25˚ between the two cameras. This is the best recommended angle at which to do stereo-vision measurements [85]. Another high-speed camera (Photron FASTCAM Mini UX50) was located on the impacted side of the sample and monitored the interaction of the projectile with the target. This camera was shooting at 20,000 frames per second, half the speed of the back cameras. The signal generated by the IR sensors, as a result of cutting the light beams by projectile, was used to trigger all three cameras. Halogen lamps were used to illuminate the target chamber area. To prevent any heating effect from the halogen lamps on the samples, the lights were turned on just a few seconds before the test.

(a)

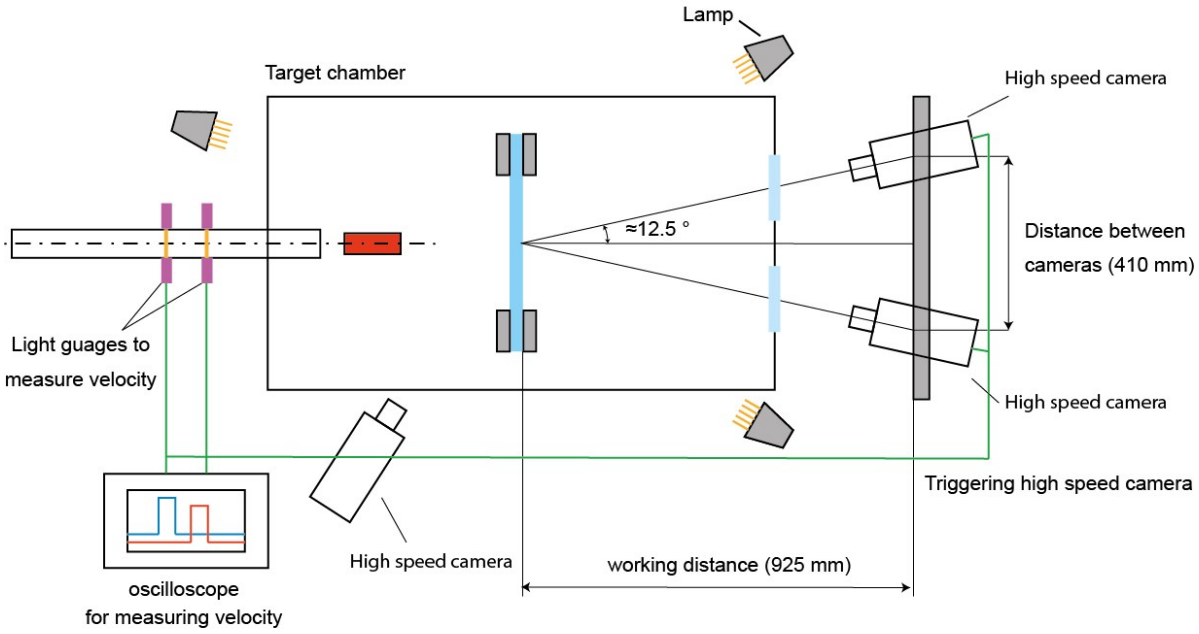

(b)

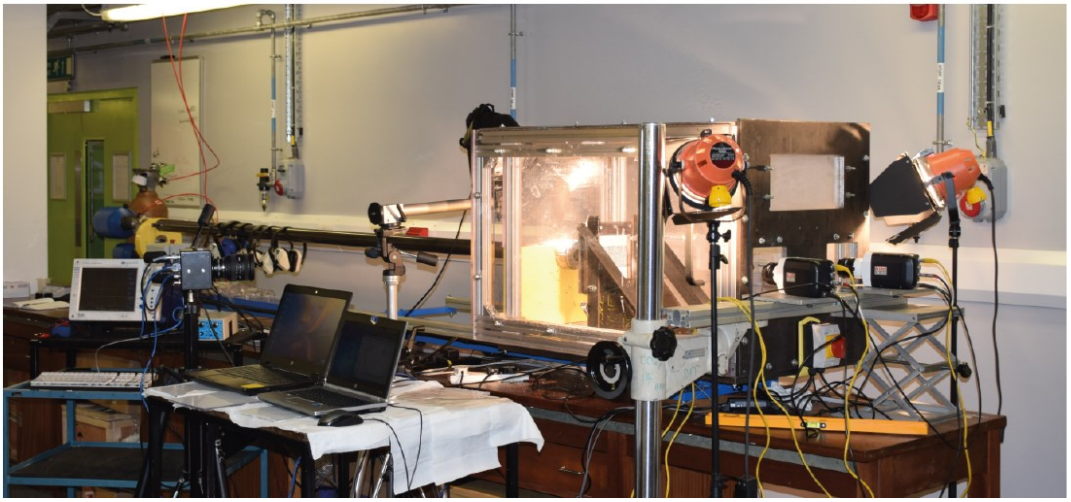

Figure 6-2. Gas gun and 3D DIC set up (a) schematic and (b) photo taken from the site.

6.1.3. Test sample preparation and boundary condition

Test samples, laminated glass samples size 180×180 mm, were clamped around the edge to a metallic fixture by using twelve M8 bolts. The clamper was made of steel and had an opening of 150×150 mm. To avoid any direct contact between the glass and metallic clamper, which can lead to stress concentration at the clamper edge and ultimately premature failure of the glass, rubber gaskets were used. A schematic of plate size and boundary conditions is shown in **Figure 6-3**. The rubber gaskets were compressed between the glass plates and the clamper by tightening the bolts. The amount of the compression, however, was controlled by the thickness of the metallic spacer, shown in **Figure 6-3**c. For all plates, rubber gaskets with a thickness of 4.1 mm were used. The size of the metallic spacer, however, varied between different configurations. For each configuration, the thickness of the metallic spacer was chosen such that there was only a small amount of compression in the gaskets. This means that the plates can be considered to be simply supported on an elastic foundation.

In order to measure the deformation of the target by the digital image correlation technique, at first a random speckle pattern was applied to the surface of the specimen. The algorithm then calculated the deformation by tracking each point through a pair of image sequences captured by the two high-speed cameras. The back surface of the specimen was initially painted in white with acrylic paint and then hand-painted using black markers to generate the maximum contrast. The recommended size of the black speckles is between 3-5 pixels for the software to recognise them [74]. For the current experimental setup, the optimum size of the speckles is between 0.7 to 1.0 mm, which can be best achieved by hand painting. To prevent any shadow from the projectile affecting the DIC calculation of the back face, the frontal layer of the glass was also painted in black.

To maximise the amount of information that could be obtained from DIC, the speckle pattern was only applied to the areas of the plate that are of more interest. Two configurations were chosen: **Figure 6-3**.a and **Figure 6-3.**b. In configuration 1 (**Figure 6-3**a), only the centre part of the specimen, with an area of 70×70 mm, was monitored. In configuration 2 (**Figure 6-3**b), the length of the observation area was expanded to the whole length of the free span of the plate (150 mm), but the width was narrowed to 33 mm, which gives a similar total area as configuration 1. In both configurations, two strain gauges were used. The strain gauge, FLA2-8 from Techni Measure Ltd, has a 2 mm linear gauge that was designed for glass and ceramics.

The surface of the glass was cleaned before attaching the strain gauge to it using Cynaoacrylate adhesive. In configuration 1, one strain gauge was located on the frontal glass layer, while the other one was located exactly at the same position but on the back face. Both of the gauges were located 30 mm from the centre and measured the strain along the y axis (**Figure 6-3**a and **Figure 6-3**b). For configuration 2, both of the strain gauges were placed on the back side: one at the centre and the other one 30 mm off-centre. It should be noted that the strain gauges were attached to the glass first and then the sample was painted, also covering the gauge itself.

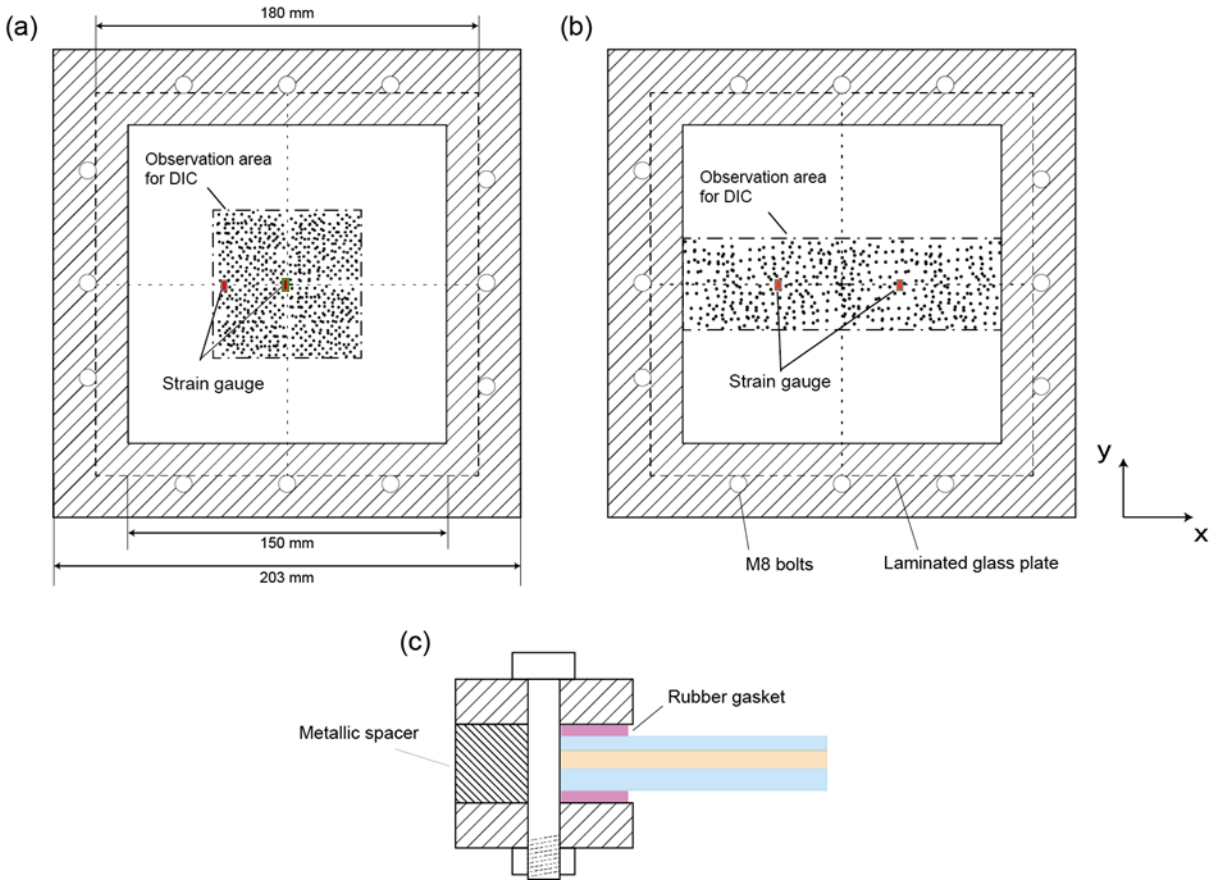

Figure 6-3. Schematic of (a and b) two types of sample preparation and (c) the boundary condition used for gas gun experiments.

6.2. Results and discussion

In this chapter, first the deformation and failure mechanisms of the laminated glass window impacted by a soft projectile is investigated. Second, the effect of different design parameters on the performance of the laminated glass windows, including the polymer type and thickness, is investigated.

6.2.1. Deformation and failure mechanisms

An example of the results is shown in **Figure 6-4**, for laminated glass (C4) impacted at a velocity of 170 m s^{-1}. The top row displays the deformation of the projectile with the target. As can be seen, the duration of the contact is very short (less than 1 ms), the projectile flows radially as expected and no part of the sabot hit the glass during its deformation. At this velocity only the frontal glass layer broke, and the back glass layer was still intact. The middle row shows the out-of-plane displacement of the target calculated by DIC. The centre of the plate was moved out by about 5.0 mm. This maximum deflection of the plate was aligned by the time the projectile completely lost its momentum and came to rest, around 450 μs. After this point the projectile, which had nearly become flat (**Figure 6-4**), began rebounding back. As noted earlier, the speed of the cameras used for DIC was twice as fast as the one used for monitoring the deformation of the projectile. Hence, for each image in the top row, two images exist for DIC calculation.

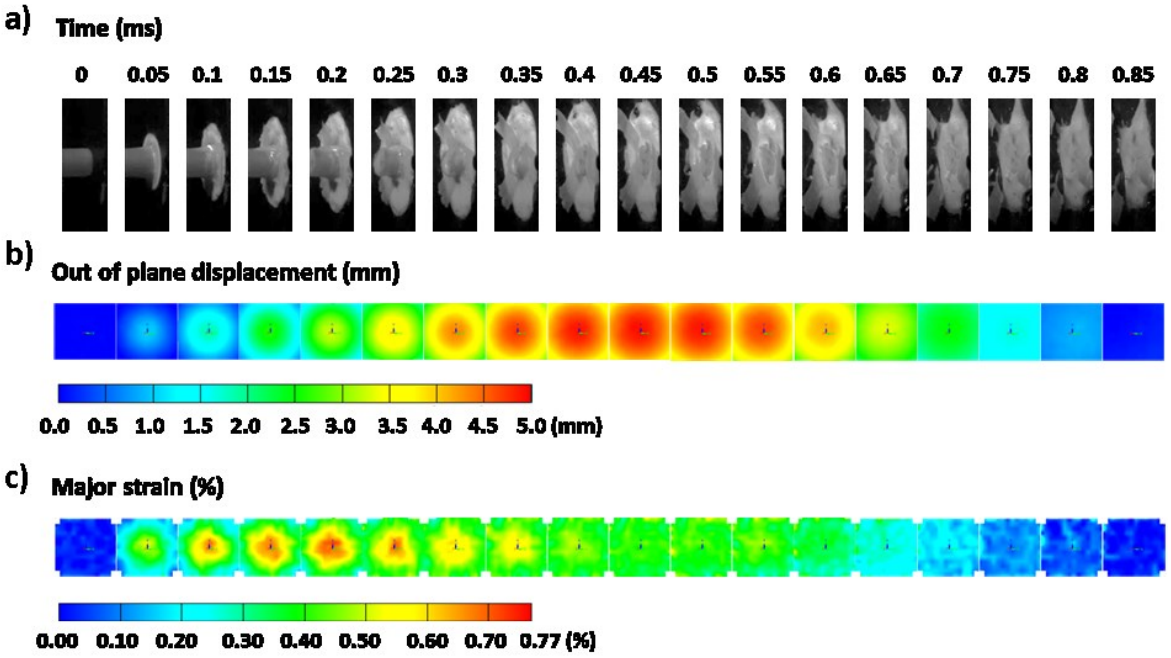

Figure 6-4. Laminated glass specimen (C4) impacted at a velocity of 170 m s^{-1}. (a) shows the deformation of the projectile, and (b) and (c) display the contours for out-of-plane displacement and major strain for the observation area (configuration 1) respectively, calculated by DIC.

The major strain calculated by DIC can be found in the bottom row of **Figure 6-4**. The maximum strain in the sample reached about 0.77%. This value is very close to the failure strain measured for this type of chemically toughened glass. The maximum strain, however, occurred around the time of 200 μs, which is not aligned with the maximum deflection in the plate. To investigate this more, the test was repeated, this time using sample configuration 2. This configuration allowed observation of the deformation over the whole span of the plate and the effect of boundary condition on the deformation of the plate. The results are shown in **Figure 6-5**. The images shown in **Figure 6-5**a and **Figure 6-5**b are rotated images based on geometric schematics shown in **Figure 6-3.**b.

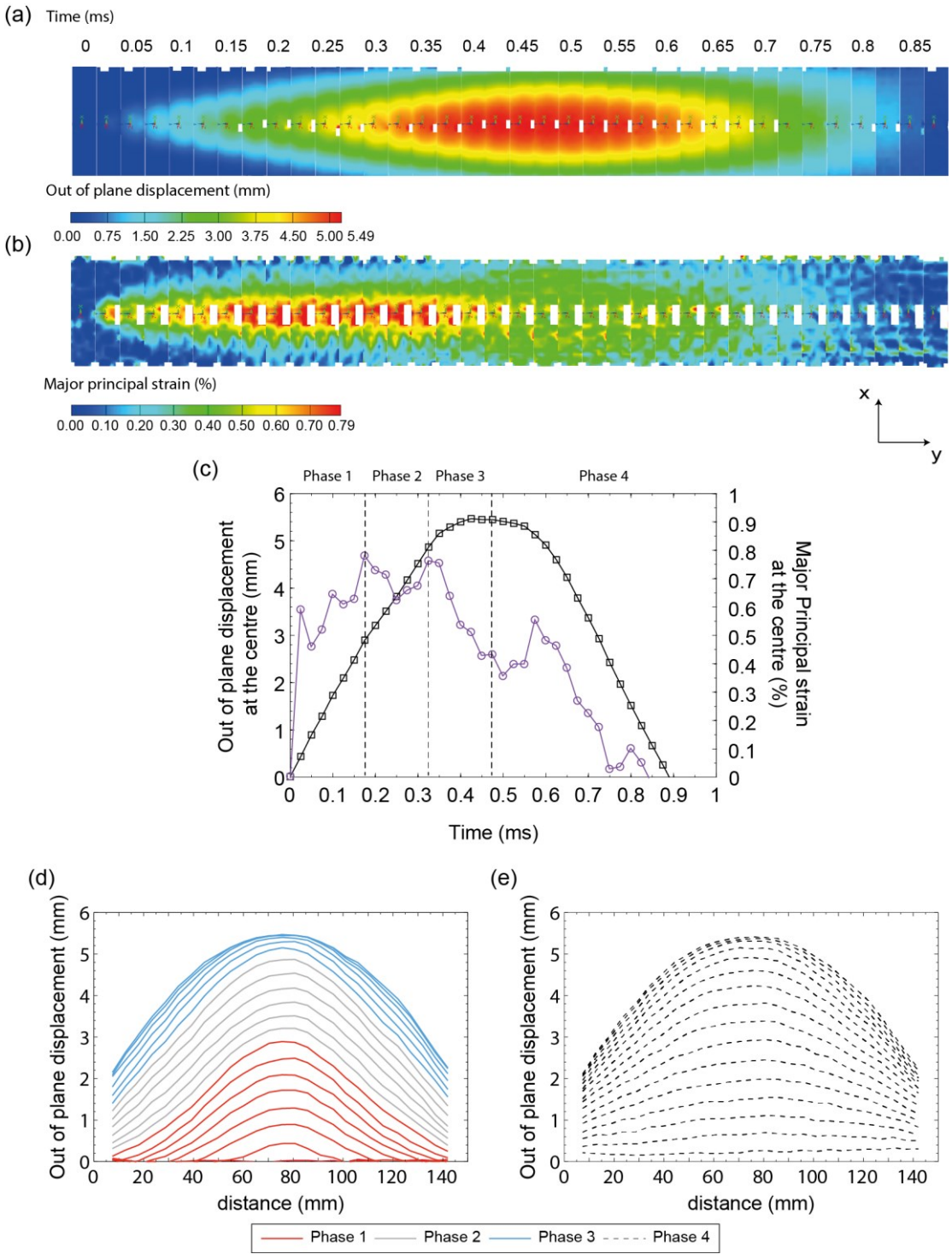

Figure 6-5. Laminated glass specimen (C4) impacted at a velocity of 174 m s^{-1}. (a) and (b) display the contours for out-of-plane displacement and major strain for the observation area (configuration 2) respectively. (c) shows the out-of-plane displacement and major strain history for the centre of the plate. (d) and (e) show the profile of the plate during the impact event for phases 1-3 and phase 4 respectively. Each individual counter in (a) and (b) corresponds to each data point in (c) and each profile in (d) and (e).

Similar to **Figure 6-4**, the out-of-plane displacement and major principal strain contours are plotted for the observed area. The maximum deflection at the centre of the plate reaches 5.49 mm and the major strain of 0.79%, as the impact speed was slightly higher than the previous test (174 m s^{-1}). The history for out-of-plane displacement and major strain is plotted in **Figure 6-5**c for the centre point of the plate. Each data point here corresponds to one of the images in **Figure 6-5**a and **Figure 6-5**b. While there is a gradual increase in out-of-plane displacement until it reaches the maximum around 475 μs, a more sudden change in the major strain can be seen, starting in the very early stages of the deformation and meaning that the maximum deflection and strain in the plate did not occur at the same time. The explanation can be found in **Figure 6-5**d and **Figure 6-5**e, where the out-of-plane displacement profile over the whole span of the plate is plotted for loading and unloading respectively. Again, the profile corresponds to one of the images in **Figure 6-5**a. The deformation of the plate can be divided into four phases, defined by a dashed line in **Figure 6-5**c and by different colours in **Figure 6-5**d and **Figure 6-5**e.

At the early stage of the deformation, phase 1, the deformation was highly localised under the point of impact and the boundaries were still not activated. By the end of phase 1, which lasted around 175 μs, the flexural elastic waves reached the boundary of the plate. During phase 2, there was little change in the shape of the deformation profile, and this meant the level of strain at the centre of the plate did not change significantly. The out-of-plane displacement of the centre, however, was still increasing. It can be noticed in **Figure 6-5**d that the amount of displacement at the boundaries is not zero. This means the rubber gasket was compressed and can account for a part of the out-of-plane displacement. In phase 3, the plate started unloading, as indicated by a significant drop in the major strain at the centre of the plate. The profile of the plate in this phase was also different from that of phase 2. The rubber gasket was still compressing in this phase and was responsible for a further increase in the out-of-plane displacement. At the end of phase 3, the gasket, which had an original thickness of 4.1 mm, was compressed by around 50%. Both out-of-plane displacement and major strain were decreasing in phase 4. The profile of the plate in this phase is plotted in **Figure 6-5**e.

6.2.2. Validation of 3D DIC results

The in-plane strain (strain in *y* direction in **Figure 6-3**) calculated by DIC is compared in **Figure 6-6** with the results of the two strain gauges mounted at the back surface of the plate for the specimen with configuration 2. As mentioned earlier, the top surface of the strain gauges were painted and speckled; therefore the deformation of the gauge could be monitored during the impact event. Overall, there is a good agreement between the two methods.

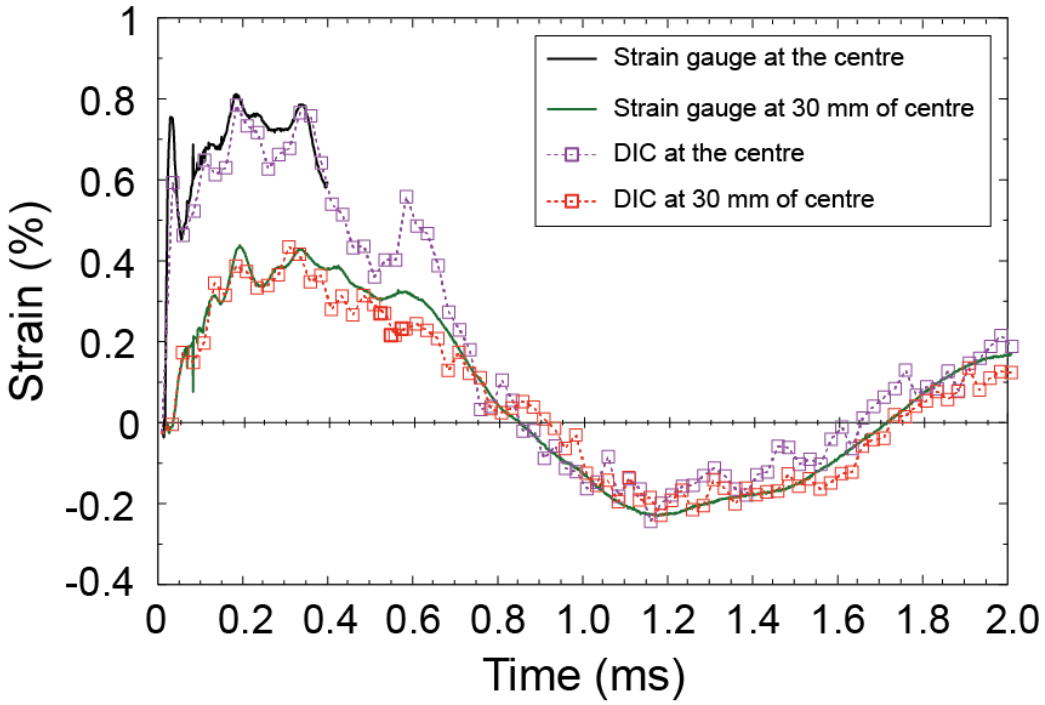

Figure 6-6. Comparison between the strain history obtained from two strain gauges and that calculated by DIC for laminated glass specimen (C4) impacted at a velocity of 174 m s^{-1}.

The strain gauge at the centre only measured the strain up to 0.4 ms from the start of the loading, as the terminals of the gauges had been peeled off while the gauge itself was still attached to the surface of the glass. This problem was observed for most of the strain gauges placed at the centre of the plate, as the out-of-plane displacement is largest at this point. The gauges recorded an initial high raise in the strain in the very first stage of the deformation, also recognised with the DIC but with a lower value. The strain in the centre of the sample reached the maximum

value of 0.8% around 0.2ms, as found by both both the strain gauge and DIC. This value is very close to the failure strain of this type of glass (0.8-1%) measured quasi-statically using a ring on ring experiment. The second gauge started recording the strain with a delay of approximately 20 μs, which is the time it takes for the flexural wave to travel 30 mm from the centre of the plate.

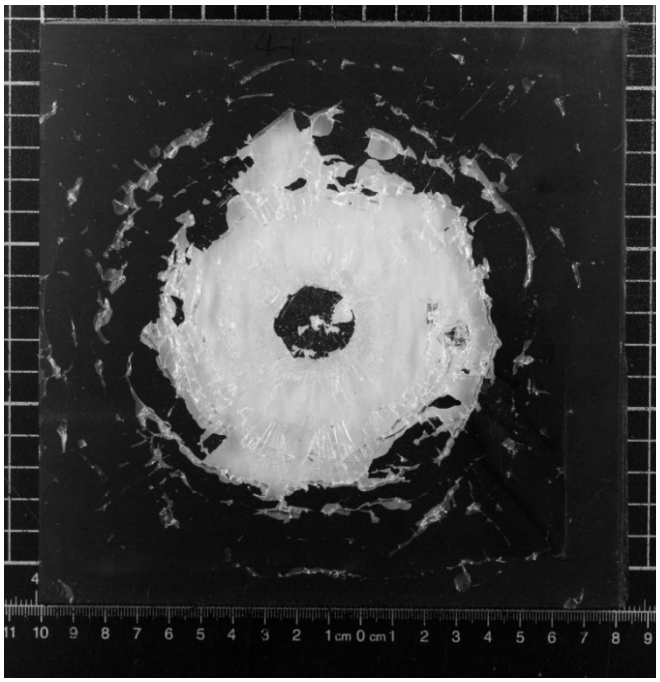

Figure 6-7. Photograph of the laminated glass (C4) impacted at the velocity of 174 m s^{-1}. The photo displays the frontal (impacted) side of the sample.

A photograph of the failed sample is shown in **Figure 6-7**. As mentioned earlier, at this speed only the frontal layer breaks while the back layer is still intact. The photograph from the impacted side of the plate (**Figure 6-7**) shows areas of black and white. As noted earlier, the impacted side of the glass was painted in black prior to the experiment, so the white area in **Figure 6-7** is an indicator of the regions where the glass fragments detached from the polymer interlayer. There is a black circular area, with a diameter equal to that of the projectile, at the centre of the plate where the glass fragments are still attached to the polymer. It is apparent from the high-speed photos that while the fracture in the frontal glass occurred during the loading phase of the deformation, the glass fragments detached only when the plate was rebounded back. The type of failure observed here is very similar to that reported for liquid jet erosion in solids.

6.2.3. Un-painted transparent LG clear shots

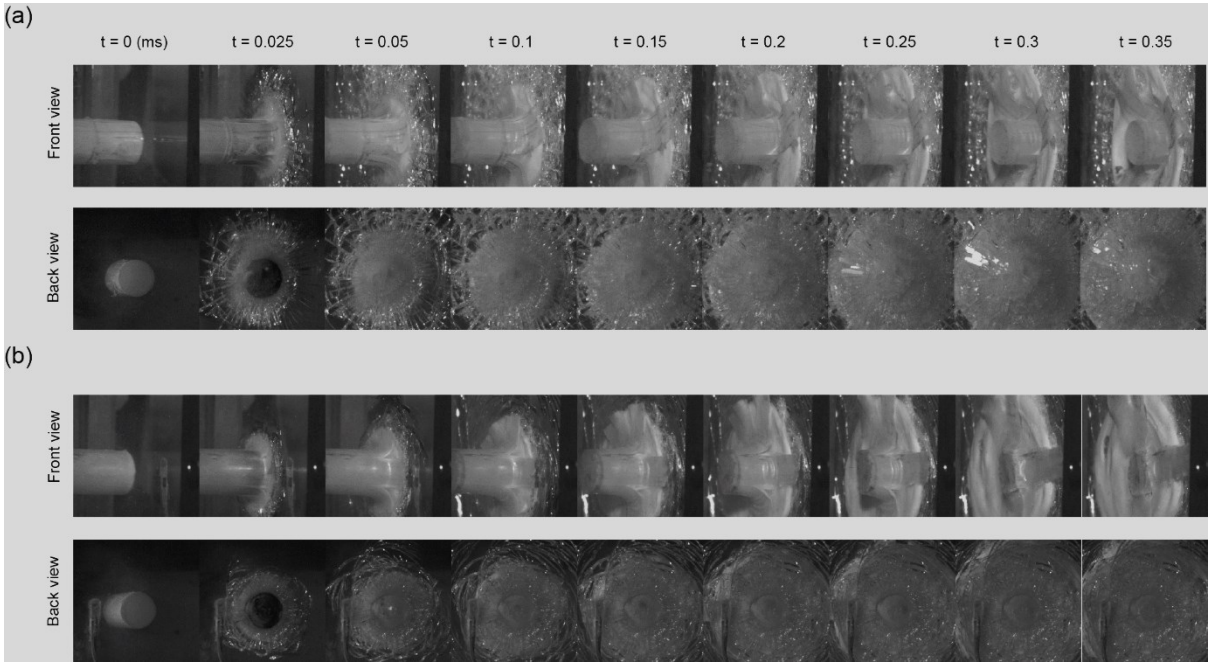

Figure 6-8. Image sequences for a 6.0 mm thick monolithic impacted at a velocity of 144 m s^{-1} ((a) front and (b) back view) and a laminated glass window impacted at a velocity of 160 m s^{-1} ((c) front and (d) back view).

Due to the black painting, the onset of the failure of the glass frontal layer is difficult to identify in high-speed photos (**Figure 6-4**a). Additionally, the strain gauge signal attached to the frontal layer was not very useful in determining when exactly the fracture was initiated. However, from the signal it can be inferred that the fracture started very early in the deformation. To further investigate this, a separate series of experiments were performed using clear glass (i.e., no painting on any sides of the glass). Two high-speed cameras were used: one observing the impacted side and the other monitoring the back side of the glass. The high-speed image sequences are shown in **Figure 6-8** for monolithic and laminated glass plates impacted at a velocity of 144 m s^{-1} and 160 m s^{-1} respectively. In **Figure 6-8**a, the monolithic glass plate was completely broken and the projectile penetrated through, while in the laminated glass plate in **Figure 6-8b**, which was impacted at a higher speed, only the frontal layer was broken. By looking more closely at the high-speed photos, it can be seen that the fracture was initiated as

soon as the projectile came into contact with the plate: the damage is apparent in the second image, which is only 25 µs after contact.

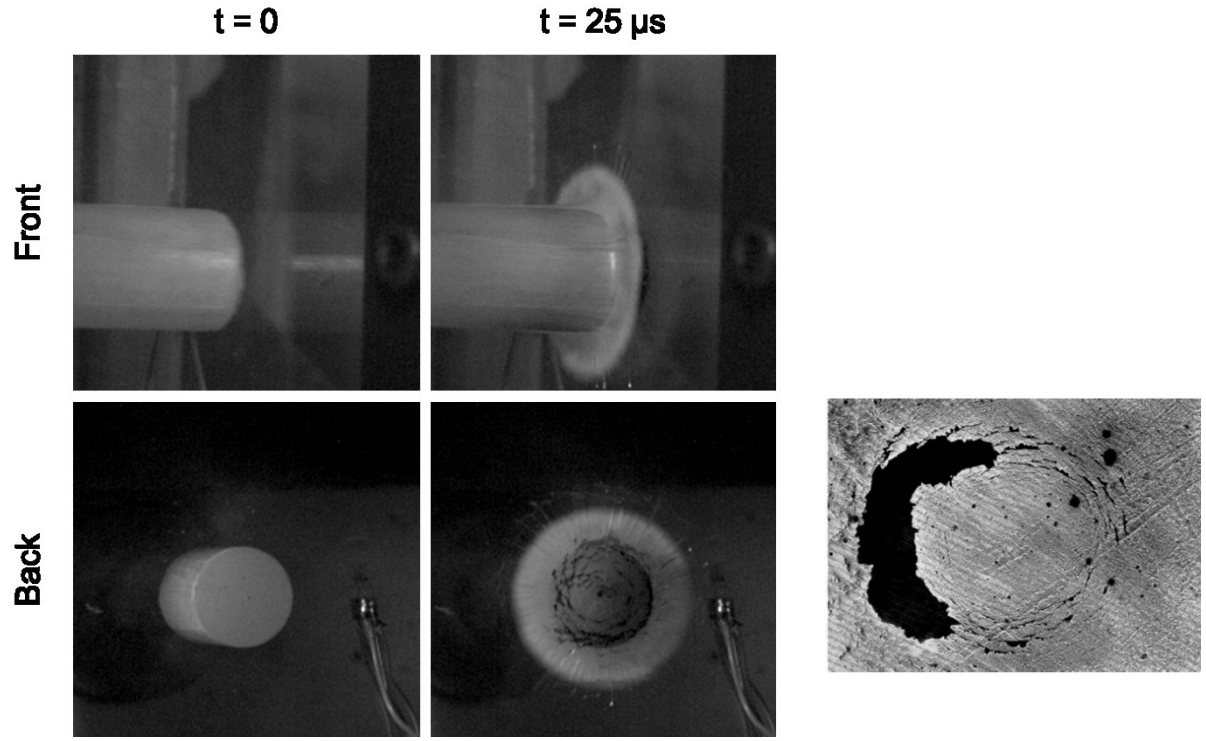

Figure 6-9. (a) High-speed photos of a laminated glass plate impacted at a velocity of 171 m s^{-1}. (b) Erosion of a glass ceramic by the impact of a liquid jet at a velocity of 720 m s^{-1} [86].

The damage initiation can be seen more clearly in **Figure 6-9,** where a laminated glass plate was impacted at a velocity of 171 m s^{-1}. It again confirms that the damage was initiated in the first 25 µs after the impact (it could have been initiated earlier). A large number of small circumferential cracks can be observed in **Figure 6-9**, which forms a ring with the diameter equal to the initial diameter of the projectile. This type of damage pattern is very similar to what was observed for the liquid jet impact shown in [86].

6.2.4. Hydrodynamic pressure profile by rubber impact

The schematic in **Figure 6-10** will help in better explaining the deformation and failure mechanism of laminated glass windows under high-velocity soft impact. A combination of the low strength of the rubber projectile compared to that of the glass and the high-velocity nature of the impact incident caused the loading to have a hydrodynamic nature in which the projectile material behaved similar to fluids.

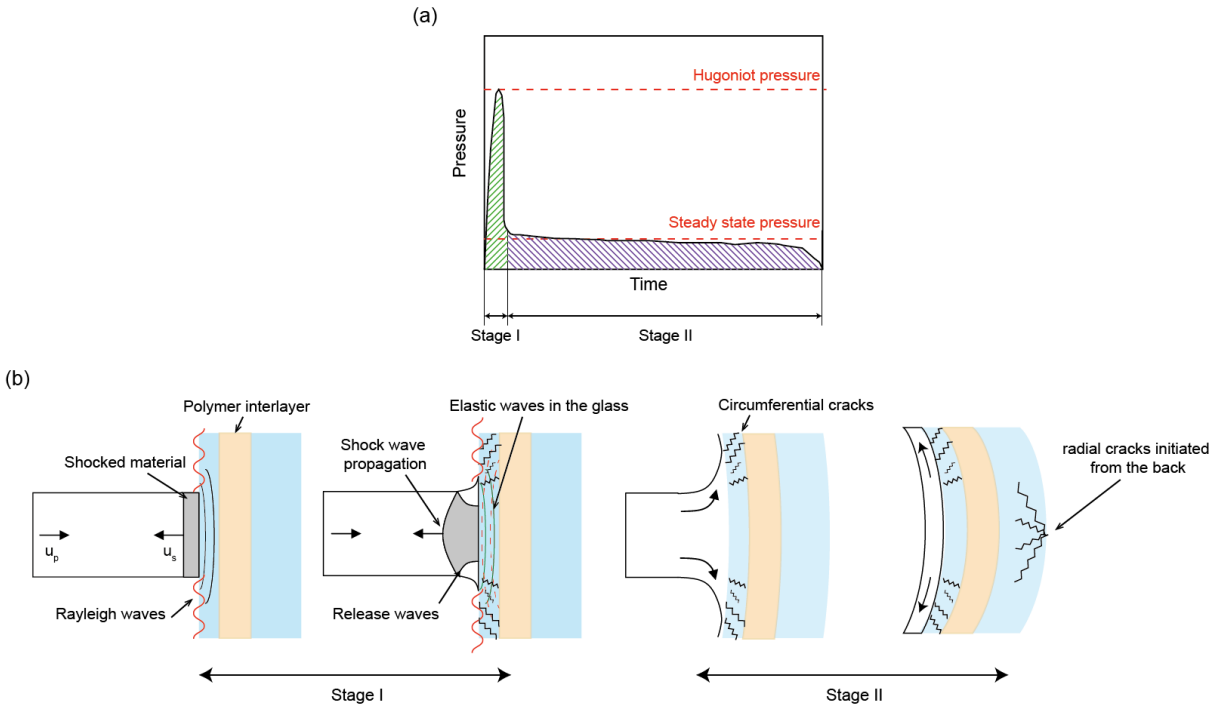

Figure 6-10. A schematic of (a) a typical pressure profile for a hydrodynamic impact event and (b) deformation and failure mechanism of a laminated glass plate subjected to an impact with a soft projectile.

In a hydrodynamic impact, the loading consists of two stages. In stage 1, as soon as the projectile comes into contact with the target (here the frontal glass layer), a shock wave is generated in the projectile propagating toward the end of the projectile (**Figure 6-10**a). The pressure generated behind the shock wave in the projectile, called "Hugoniot pressure" P_H, depends on the initial density (ρ_0) and velocity of the projectile (V_0) as well as the shock wave speed in the projectile (V_s), with the following relationship:

$$P_H = \rho_0 V_0 V_s \qquad \textbf{Equation 6-1}$$

At the time of the incident, two types of stress waves are also generated in the target: surface waves, called "Rayleigh waves", and compression waves (**Figure 6-10**b). Due to equilibrium in the loading direction at the projectile-target interface, the pressure inside the front glass layer should be equal to that of **Equation 6-1** in stage 1 [67]. Soon after the initial phase of the contact, the release waves were generated at the edges of the projectile, causing the formation of high-velocity jets. These release waves started propagating inside the shocked area, which led to a significant drop in the pressure inside this region. The duration of stage 1 depends on how fast these waves can reach the centre of the projectile, which itself is a function of speed of sound in the shocked material and the radius of the projectile [67]. For example, for a cylinder of water, depending on the velocity (which varies between 0 to 300 m s^{-1}) and radius (which varies between 10 to 30 mm), the duration of stage 1 is reported to be between 5 to 20 µs) [67]. During this period, the compressive elastic waves reached the boundary between the glass and polymer interlayer. As there is a mismatch between the acoustic properties of the glass and polymer layers, most the initial compressive wave turned to tensile and reflected back from the interface. According to the speed of sound in glass (5640 m s^{-1}), the time it takes for the wave to reach the surface as tensile wave is less than 1 µs. Similar to what has been reported for liquid jet impact on thin glasses [86]; a combination of Rayleigh and reflected tensile waves is believed to be responsible for the fracture of the frontal glass layer. The fact that the damage in the frontal glass layer occurred early in the deformation also supports this argument.

In the second stage of the deformation, known as "steady state", the projectile flows radially and the pressure can be estimated using the Bernoulli equation:

$$P_s = \frac{1}{2}\rho_0 {V_0}^2 \qquad \textbf{Equation 6-2}$$

The duration of this stage can be estimated by the time the projectile needs to travel over its length. However, this can be considered an upper limit, as the projectile might slow down during its interaction with the target. During stage 2, the frontal glass layer was already broken

and assumed not to contribute significantly to carrying the load. The time scale in stage 2 was sufficient for the development of flexural waves, which were initiated from the centre of the plate and moved toward the boundary (**Figure 6-5**d). If the momentum of the projectile is enough, the glass backing layer will normally break at the centre of the plate, where the flexural stress is maximum.

6.2.5. Effect of design parameters on the impact performance

In this section, the effect of various design parameters on the impact performance of laminated glass windows is investigated, using C3, laminated glass with two layers of chemically toughened glass and 3.18 mm TPU as polymer interlayer, as the reference case. Impact tests at different velocities were performed on this configuration. The results are shown in **Figure 6-11**. **Figure 6-11**a displays the photos taken from the frontal side of the laminated glass windows impacted at five different velocities. At a velocity of 131 m s^{-1}, no damage was observed in any of the glass layers. The threshold at which the frontal glass layer breaks, at 146 m s^{-1}, shown in **Figure 6-11**a, depends on the intensity of the waves produced in the first stage. The level of Hugoniot pressure (**Equation 6-1**) is strongly dependant on the projectile initial velocity: both directly V_0 and indirectly V_s, normally Hugoniot pressure is a quadratic function of projectile initial velocity. At a lower velocity (e.g. 131 m s^{-1}), the intensity of the stress waves in stage 1 might not be high enough to fracture the glass, despite its hydrodynamic nature. The level of Hugoniot pressure rises steeply with an increase in the projectile initial velocity and becomes sufficient to break the glass frontal layer at impact velocities of 146, 157, 165 and 179 m s^{-1}, shown in **Figure 6-11**a. In all of these cases only the frontal layer is damaged, and the back layer is still intact. When the momentum of the projectile is enough (i.e. increasing the velocity to 179 m s^{-1}), the back layer will be broken. The high-speed photos confirm that at this velocity, again the frontal layer fails first.

The maximum strain at two different locations against projectile initial velocity is plotted in **Figure 6-11**b. The hollow symbols indicate the maximum strain at the point 30 mm off-centre of the plate (**Figure 6-3**a and **Figure 6-3**b), obtained from the strain gauge. The solid symbols, which have higher values, are the maximum strain at the centre of the plate, obtained from DIC. Two linear curves are fitted through the data. A good fit is observed for the data obtained from the strain gauge. A slight deviation from the linear fit for solid symbols is due to uncertainty in

obtaining the maximum strain using DIC as a result of lack of resolution. These curves will be used as reference in the following sections to assess the effect of each isolated design parameter on impact performance.

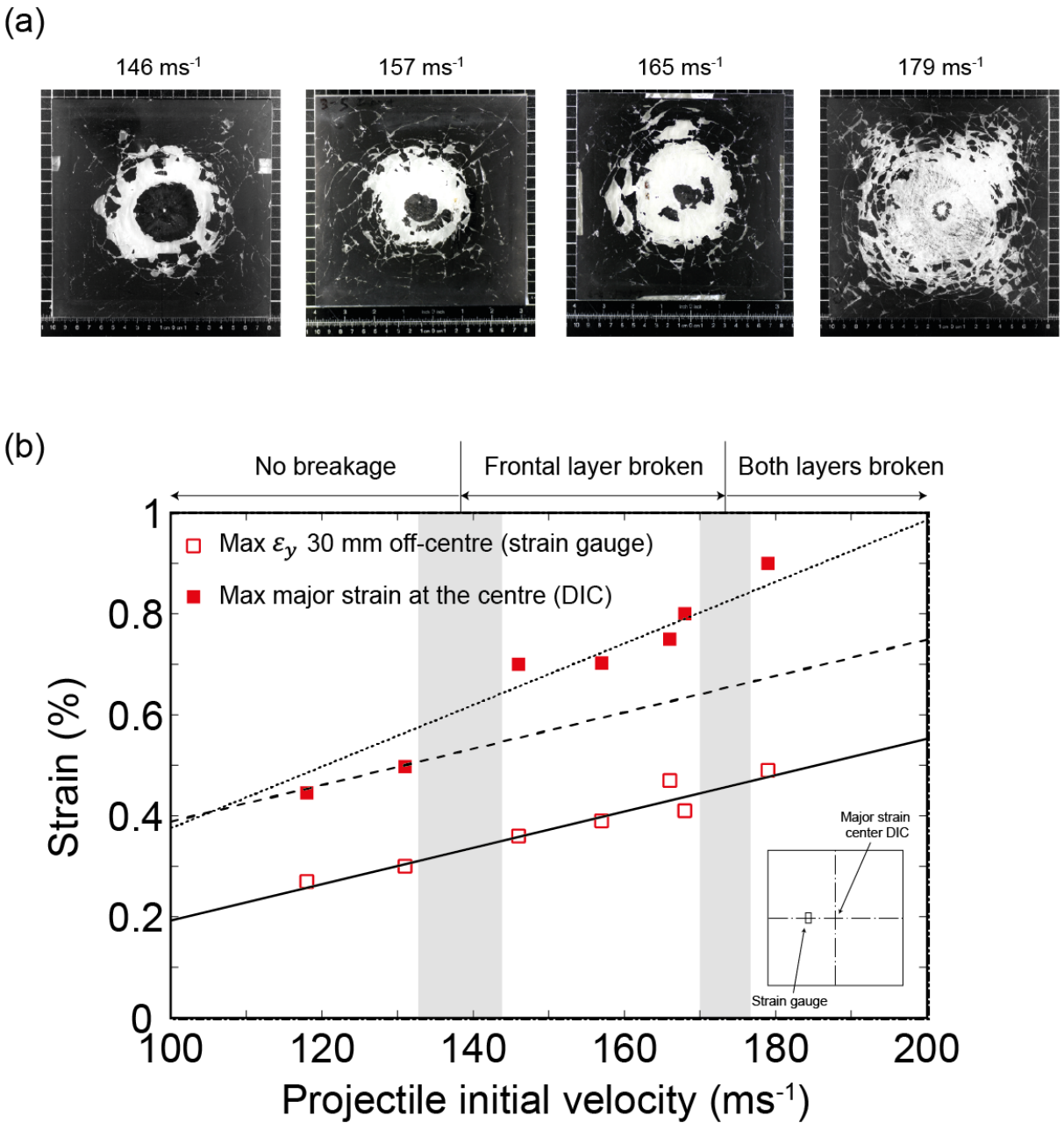

Figure 6-11. (a) Photo of the impacted laminated glass plates (C3) at five various velocities and (b) maximum strain at two locations versus impact initial velocity for laminated glass (C3).

6.2.6. Effect of polymer interlayer type at different impact velocities

In this section, the effect of using a more rigid interlayer will be investigated by comparing the performance of C3 (TPU interlayer) and C5 (SGP interlayer). As stated earlier, at room temperature SGP is lower than its glass transition temperature (T_g= 55 ˚C). As a result, its behaviour is more glassy and its elastic mechanical properties (e.g. stiffness) is two orders of magnitude greater than that of TPU, which is well above its glass transition (T_g= -34 ˚C) at room temperature. The photos taken from the failed sample with SGP and TPU interlayers are shown in **Figure 6-12** for two impact velocities, 165 and 179 m s^{-1}.

Figure 6-12 shows both the front and back sides of the samples. At a velocity of 165 m s^{-1}, for both cases only the frontal layer was broken. It is believed that the failure mechanism described in **Figure 6-10** is still responsible for the damage observed in both cases. The only difference can be the amount of the compression wave that reflected to the tensile wave at the interface between the glass and polymer interlayer. The density of SGP ($\rho \approx 0.95 kgm^{-3}$) is similar to that of TPU and still is nearly one third of glass ($\rho \approx 2500 kgm^{-3}$). However, the elastic modulus of SGP is two orders of magnitude greater than TPU, and as a result SGP has closer acoustic properties to that of the glass. Therefore, a smaller portion of a compression wave will be reflected and turned to a tensile wave at the interface of frontal glass and polymer interlayer, compared to the case of TPU.

At a velocity of 179 m s^{-1}, the momentum of the projectile was sufficient to break the glass backing layer of the laminated glass window with TPU interlayer. However, for laminated glass with SGP, only the frontal glass layer broke and the backing layer was still intact. One notable difference between the damage patterns in frontal glass layers for the two laminates is the number of glass fragment that detached from the interlayer (demonstrated by the white area in the photo taken from the front impacted side of the specimen, as shown in **Figure 6-12**). This is probably due to lower adhesion properties between the glass and the SGP interlayer.

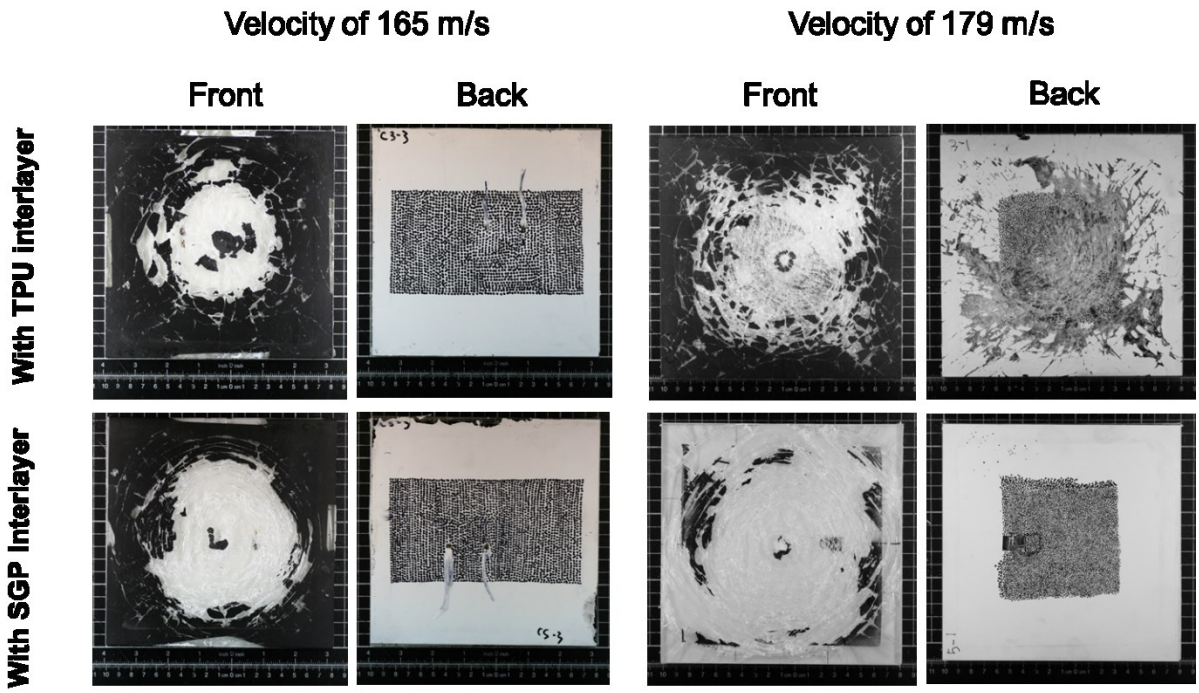

Figure 6-12. Photos of damaged laminated glass samples with two types of polymer interlayer, soft (TPU) and rigid (SGP), impacted at velocities of 165 and 179 m/s.

The performance of the laminated glass samples with two types of polymer interlayer, soft (TPU) and rigid (SGP), is compared in **Figure 6-13** for different impact velocities. The maximum strain at the glass backing layer at two different positions is used for comparison: centre (solid) and 30 mm apart from centre horizontally (hollow). The maximum strain for the laminated with SGP interlayer does not following the linear trend, similar to what has been observed for the laminate with TPU interlayer, and scattering is larger. In general, the level of maximum strain is lower for the case of laminate with SGP, as proves by the maximum strain comparison of both centre and 30 mm apart data groups.

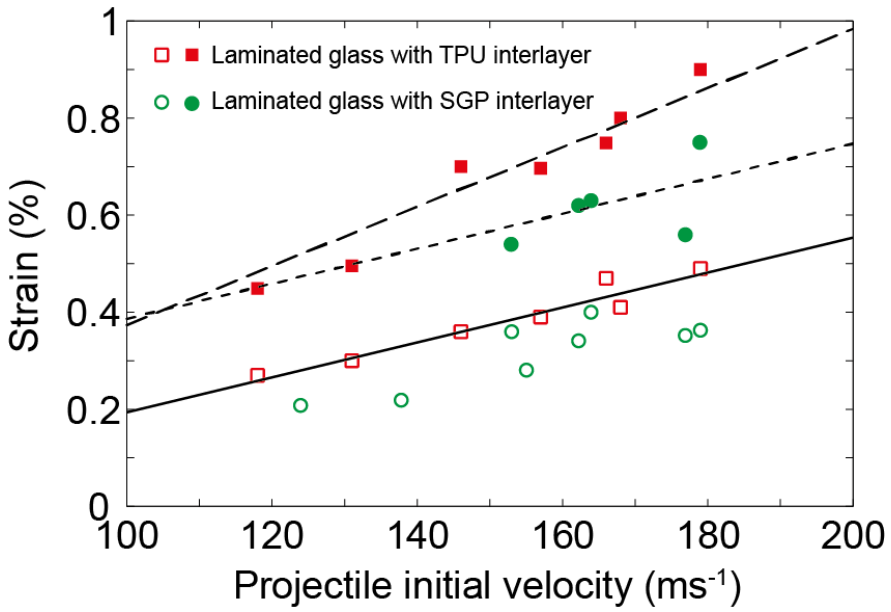

Figure 6-13. Maximum strain at the glass backing layer for laminated glass sample with two types of polymer interlayer: soft (TPU) and rigid (SGP) at centre (solid) and 30 mm apart from centre horizontally (hollow).

Effect of polymer interlayer type at 165 m s^{-1}

An example of strain traces for the two laminates is shown in **Figure 6-14** at a velocity of 165 m s^{-1}. For the laminate with SGP (red solid, diamond), the strain gauge only recorded the value up to 400 μs before the terminals of the strain gauges were broken in **Figure 6-14**a. It can also be inferred that the main difference between the strain traces of the two laminates occurred at the early stage of the deformation, in the first 200 μs of the impact. For a better understanding of the difference, the out-of-plane displacement profile of a cross-section from the plate during deformation, the history of out-of-plane displacement and major strain from the centre of the plates are compared in **Figure 6-15**. Similar to **Figure 6-4**, the deformation is subdivided into four phases. From the high-speed videos, it is known that the front glass layer broke in the first few microseconds after the initial contact (less than 25 μs), and it did not significantly contribute to carrying the load for the rest of the event. Therefore, for the rest of the impact event, we are dealing with a bi-layer plate consisting of one layer of polymer and one layer of glass. Although the polymer layer lost its shear transferring functionality between the two glass layers, where the more rigid interlayer increased the stiffness in the laminated configuration, it still had a significant effect on the duration of the contact, maximum deflection and development of strain in the sample. It is obvious from both the out-of-plane displacement and

the major strain history at the centre of the plate that for a more rigid interlayer, the duration of the contact is shorter for the laminated glass with SGP, as shown in **Figure 6-15**c and **Figure 6-15**d. This means a more rigid polymer (SGP) can reinforce the whole structure to be stiffer. The high rigidity of SGP also had a direct influence on the strain development in the glass backing layer, especially in the first two phases of the deformation. In the phase 1, where the deformation is highly localised and the boundaries are not activated yet, the level of strain in the sample for the laminate with TPU rose sharply, as shown in **Figure 6-15**a and **Figure 6-15**c. The duration of phase 1 depends on how fast the flexural waves can reach the boundary of the plate. These flexural waves took only about 100 μs for the laminate with SGP, compared to 175 μs for the case with the TPU interlayer. A comparison between **Figure 6-15**c and **Figure 6-15**d clearly shows that SGP had a smoother profile in phase 1 before 175 μs. In phase 2, the strain for laminated glass using TPU remained nearly constant (between 175 μs to 350 μs), whereas the strain continued rising in the SGP case (between 100 μs to 280 μs). At the end of phase 2, both laminates reached a similar level of strain.

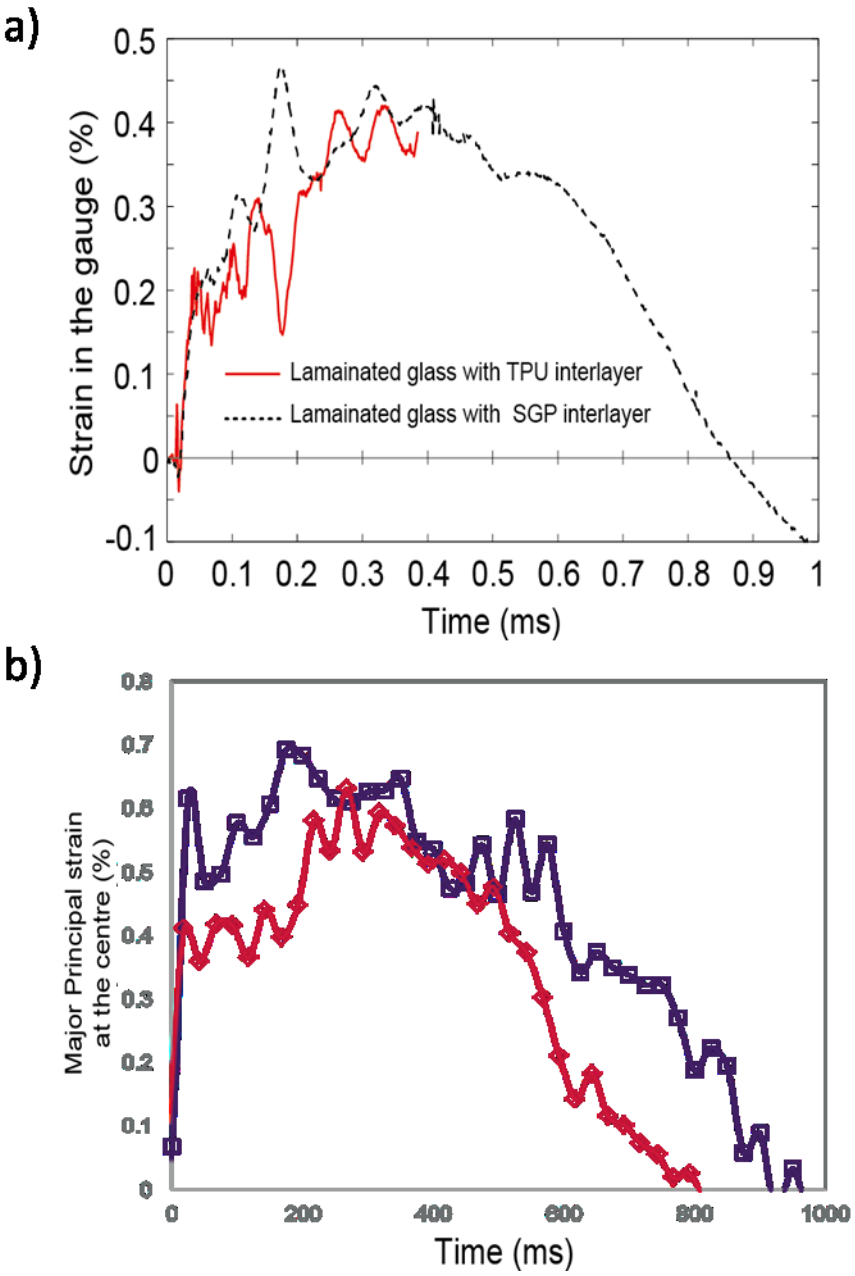

Figure 6-14. Comparison between the strain history of laminated glass windows with TPU (blue dashed, square) and SGP (red solid, diamond) interlayers impacted at a velocity of 165 m s^{-1} for (a) strain gauge 30 mm off centre and (b) major strain at the centre of the specimen, calculated by DIC.

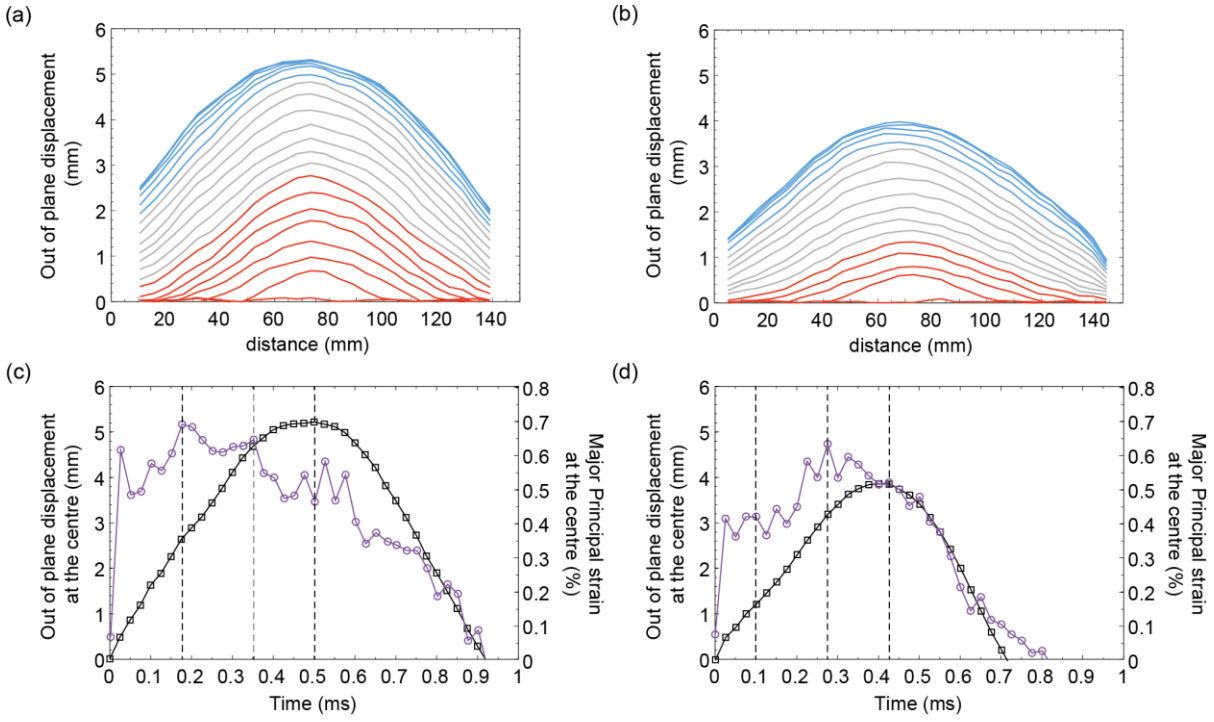

Figure 6-15. (a) and (b) are the out-of-plane displacement profiles for laminated glass with TPU and SGP interlayers impacted at a velocity of 165 m s^{-1} respectively. (c) and (d) are out-of-plane displacement and major strain history at the centre of the laminate with TPU and SGP respectively.

6.2.7. The effect of polymer interlayer thickness

The performance of the laminated glass sample using TPU with two thicknesses, 3.18 mm (red) and 5.09 mm (green), is compared in **Figure 6-16**a for different impact velocities. The maximum strain on the glass backing layer at two different positions is used for comparison: centre (solid) and 30 mm apart from centre horizontally (hollow). In general, the levels of maximum strain at each velocity are lower for 5.09 mm TPU, as proved by the maximum strain comparison of both centre and 30 mm apart data groups. Due to variation and noise, the strain information collected from 3D DIC may be not as stable as the strain gauge information, but in general, both strain gauge and 3D DIC give reasonable coincidence that the strain level for the thicker TPU interlayer helps to reduce the back glass ply's strain level for all the velocities tested.

An example of strain traces for the two laminates is shown in **Figure 6-16**b for the velocity of roughly 165 m s^{-1}. The laminate using TPU with two thicknesses, 3.18 mm (black dashed line) and 5.09 mm (red solid line), shows similar strain profiles but with different scales of the strain level. Although laminated glass for both thicknesses were not broken, the difference in the

strain level is clearly seen—increasing the thickness means lowering the strain in the backing glass ply of laminated glass.

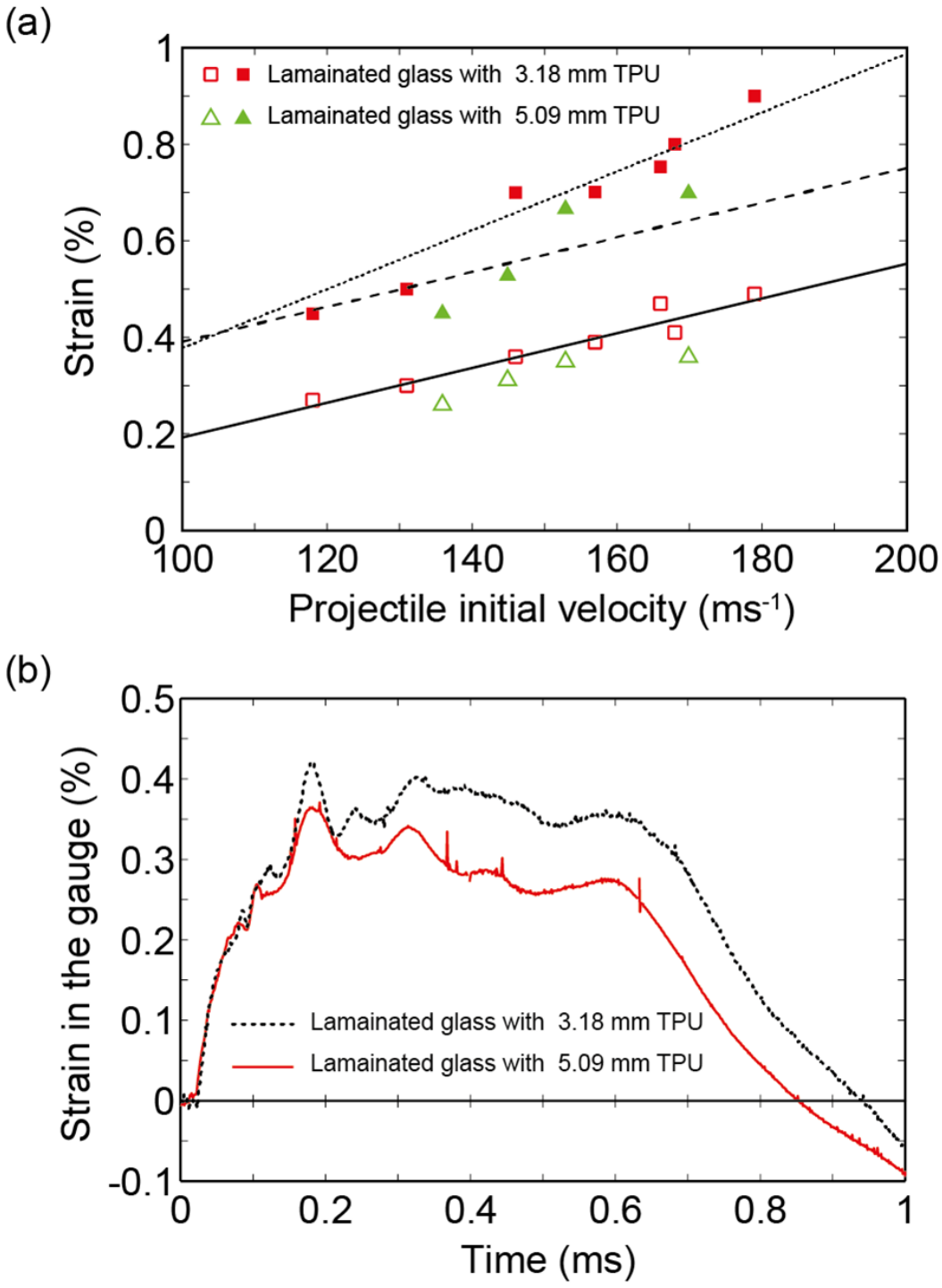

Figure 6-16. a) Maximum strain at the glass backing layer for laminated glass sample using TPU with two thicknesses, 3.18 mm (red) and 5.09 mm (green), at centre (solid) and 30 mm apart from centre horizontally (hollow). b) Comparison between the strain histories of laminated glass windows using TPU with two thicknesses, 3.18 mm (black dashed line) and 5.09 mm (red solid line), impacted at a velocity of 165 m s^{-1} for strain gauge 30 mm off centre.

6.2.8. The effect of multi-layered polymer interlayer:

The performances of the laminated glass sample using TPU (red), SGP (green) and multi-layered (orange) polymer interlayers at the centre (solid) are compared in **Figure 6-17**a for different impact velocities. The maximum strains at the glass backing layer of both TPU and SGP laminated glass have been introduced previously. In general, the level of maximum strains at each velocity for multi-layered structures are lower in comparison to TPU and similar to what has been observed with SGP, as proved by the maximum strain comparison of both centre and 30 mm apart data groups. Due to variation and noise, the strain information collected from 3D DIC may be not as stable as the strain gauge information, but in general, both strain gauge and 3D DIC provide reasonable coincidence on what has been seen. This behaviour is mainly due to the fact that the material used in a multi-layered interlayer structure is still a major structural SGP interlayer with a minor adhesive interlayer to adhere between the glass and SGP to prevent the delamination obverted previously using only SGP.

An example is shown in **Figure 6-17**b of strain traces of laminated glass windows using TPU (black dashed line) and multi-layered (red solid line) polymer interlayers impacted at a velocity of 168 m s^{-1} and 170 m s^{-1}, respectively, from strain gauge 30 mm off centre. Ignoring the small variation from velocity difference, the laminate multi-layered polymer interlayer shows similar strain profiles but with a smaller scale of the strain level. Laminated glass for both thicknesses were broken; the frontal glass ply fracture pattern of multi-interlayer structures after impact at 170 m s^{-1}, as shown in **Figure 6-17**c, shows much better glass fragments attachment compared to the large peeling-off phenomenon observed in **Figure 6-12** for SGP. The information from this effect is that a multi-interlayered structure lowers the strain in the backing layer as well as prevents the peeling off of large glass fragments.

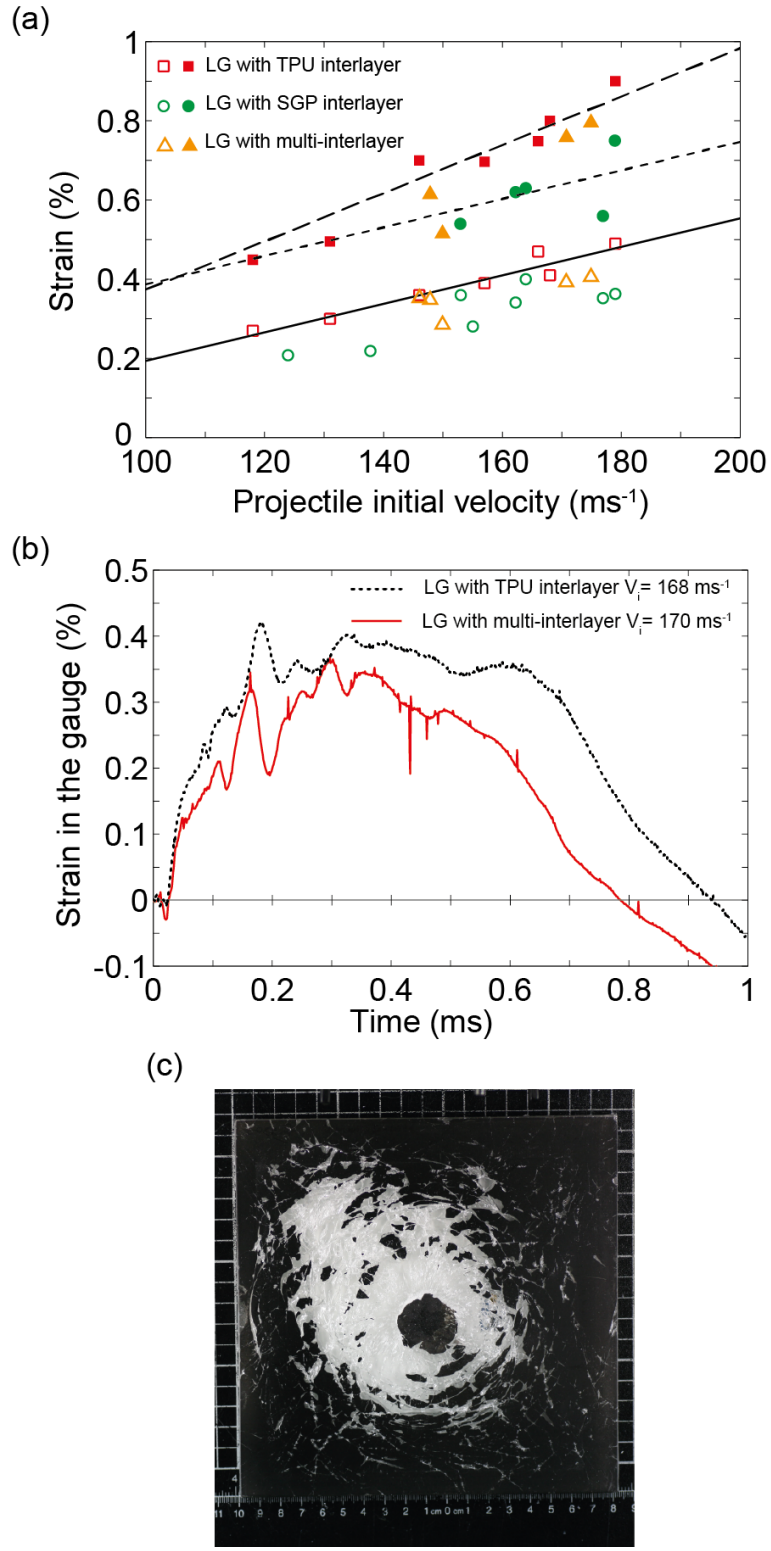

Figure 6-17. a) Maximum strain at the glass backing layer for laminated glass sample using TPU (red), SGP (green) and multi-layered (orange) polymer interlayer at centre (solid) and 30 mm apart from centre horizontally (hollow). b) Comparison between the strain histories of laminated glass windows using TPU (black dashed line) and multi-layered (red solid line) polymer interlayer impacted at a velocity of 168 m s^{-1} and 170 m s^{-1} for strain gauge 30 mm off centre respectively. c) Frontal glass ply fracture pattern of multi-interlayer structure after impacted at 170 m s^{-1}.

6.3.Conclusion

The summary of this chapter is the following:

- Laminated glass structural performance with different interlayer conditions has been studied in high-velocity impact experiments. The experiments use both strain gauge and 3D DIC to validate experimental results and interpret performances from different velocities to help design better laminated glass structures to prevent damage from bird strikes.
- A typical hydrodynamic pressure profile impacted by a soft projectile consists of two stages: surface waves (called Rayleigh waves) and compression waves are generated in the first stage due to Hugoniot pressure. During this period, the shock wave will create high-velocity jets and cause release waves to propagate inside the shocked area of the laminated glass frontal glass ply. A combination of Rayleigh and reflected tensile waves is responsible for the fracture of the frontal glass layer. In the second stage, the projectile flows radially and the glass backing layer will break, normally at the centre of the plate where the flexural stress is maximum.
- Increasing the thickness of TPU from laminated glass will lower the strain in the backing glass ply from the laminated glass system.
- The level of maximum strain is lower from laminate with SGP, as seen in the maximum strain comparison of both centre and 30 mm apart data groups. More rigid polymer (SGP) can reinforce the whole structure to be stiffer.
- A multi-interlayered structure lowers the strain in the backing layer as well as prevents large glass fragments from peeling off.
- For monolithic glass under high-velocity soft impact, the fracture is initiated from the impacted side of monolithic glass, which then propagates through the thickness and leads to the total failure of the structure. In the laminated glass, however, the failure in the frontal glass layer is isolated and cannot propagate through the interlayer.

7. Conclusion

Chemically strengthened monolithic glass was examined under a quasi-static ring supporting configuration with two loading conditions: rigid ring and soft rubber. The experiment provides informative out-of-plane displacement and major strain measurements to understand material performance at quasi-static levels. The performance of laminated glass windows consisting of two layers of chemically strengthened glass and different interlayers is evaluated under quasi-static, low- and high-velocity soft impacts. A 3D DIC technique validated by a strain gauge was used to achieve these measurements and evaluation. Seven laminated glass cases were designed to incorporate the influence of glass treatment types, polymer types and relative thickness on laminated glass structural performance. The laminated glass consisted of glass ply from loading/impact side (2.2 mm), different configurations of polymer interlayer (TPU, PVB and SGP) and glass ply from supporting side (4.0 mm).

7.1. Mechanical performance of monolithic and laminated glass at quasi-static levels

To assess the structural performance of laminated glass at quasi static level, conventional coaxial double ring compression was adapted to determine the flexural bending strengthen of monolithic glass with help from the strain acquisition technique of digital image correlation (3D DIC) at the specimen's back side. The strain acquisition method has been validated by strain gauge and provides a more straightforward strain measurement by comparing other measurements from the literature using analytical and numerical methods. The flexural bending strength of 2.2, 4.0 and 6.0 mm monolithic glasses were measured by applying the 3D DIC method on coaxial double ring compression. 6.0 mm monolithic glass had highest modulus based on Weibull distribution statistics. Two types of loading conditions were studied to simulate rigid (concentrated) contact and soft (distributed) contact: ring loading and rubber loading. More uniform stress distribution was observed from rubber loading 3D DIC experimental results, which led first to fracture in the glass ply at the supporting side of the laminated glass, followed by breaks in the glass ply at the loading side, then finally the failure of the entire laminated structure. In contrast, more concentrated stress distribution near the loading ring area was observed from the rigid ring loading 3D DIC experimental results and

the fracture sequence began with glass ply at the loading side, followed by glass ply on the supporting side. Comparing the experimental loading conditions of rigid ring and soft rubber loadings indicated that rubber loading can provide a higher peak load before the second fracture if the glass ply at the loading side breaks first. Laminated glass using SGP showed catastrophic fracture similar to that of equivalent thickness glass, because in both ring and rubber loading conditions, the SGP interlayer could not hold many fragments after the test. During ring loading tests, an increased TPU interlayer thickness caused a change of the laminated glass fracture sequence from the 2.2 mm glass ply of the loading side to the 4.0 mm glass ply of the supporting glass side. An effect on polymer thickness to structural performance was observed in terms of impact energy whereby laminated glass using a thicker TPU interlayer definitely has better performance compared to laminated glass using a thinner TPU interlayer. Multi-layered interlayers did not show significant improvement of structural performance in either the quasi-static ring or the rubber loading tests. Based on the results of both the ring loading and rubber loading tests, in terms of fracture energy absorption, the 2.2 mm loading glass side using chemical strengthening showed better performance compared to using thermally strengthened glass ply. Under the same geometric condition, laminated glass using TPU showed better structural performance compared to lamination using PVB for both loading conditions. The strain level needed to break both the monolithic glass plate and the supporting glass side from laminated glass are around 0.8 % for chemically strengthened glasses.

7.2. Mechanical performance of laminated glass at low velocity

To assess the structural performance of laminated glass at low velocity impact range, a light weight drop tower was applied. The effect of polymer thickness on structural performance was studied in terms of impact energy and laminated glass using thicker TPU showed better performance compared to thinner interlayers in thinner laminated glasses. Due to different polymer mechanical behaviour from true stress strain results, laminated glass with same polymer thickness but different polymer types demonstrated different structural performance in terms of fracture pattern and impact energy. Amongst all configurations, laminated glass using SGP survived at higher drop heights due to its distinguishable viscoelastic material behaviour from high modulus of linear elastic stress strain region with high rigidity compared to those from PVB and TPU. However, this configuration failed with a much more catastrophic

fracture pattern and could not maintain post breakage functionality after impact. Laminated glass using TPU has better structural performance in terms of impact energy than that using PVB; however, one noticeable phenomenon was that PVB effectively shifted from rubbery behaviour material to viscoelastic material by having glassy elasto-plastic behaviour with a linear initial gradient. All of this happened at room temperature which is in the glass transition temperature range. This indicates that the ultimate stress required to break PVB will be increased with an increase of strain rate which benefits the laminate structure at high strain rates. Based on the results from laminated glass using chemically and thermally strengthened glass respectively, 2.2 mm front impact glass ply with chemically strengthened treatment had a much better structural performance. When applying multi polymer interlayers, the performance of multi layered interlayers definitely showed better structural performance with higher impact energy. Interestingly, two stages of breakage allows the structure to absorb more energy before fracture.

7.3. Mechanical performance of laminated glass at high velocity

A light gas gun was used to assess the structural performance of laminated glass at high velocity impact range. The structural performance of laminated glass with different interlayer conditions was studied in a high velocity impact experiment using both strain gauge and 3D DIC to validate experimental results and interpret performance from different velocities in order to help design a better laminated glass structure to prevent fractures from bird strike. A typical hydrodynamic pressure profile impacted by soft projectile consists of two stages. Surface waves (or Rayleigh waves) and compression waves are generated from the first stage due to Hugoniot pressure. During this period, the shock wave will create high velocity jets and cause release wave propagating inside the shocked area of laminated glass frontal glass ply. A combination of Rayleigh and reflected tensile wave is responsible for the fracture of the frontal glass layer. In the second stage, the projectile flows radially, and the glass backing layer will break normally at the centre of the plate where the flexural stress is maximum. Increasing the thickness of TPU from laminated glass will lower the strain in the backing glass ply from the laminated glass system. A maximum strain comparison of both the centre and 30 mm apart data groups indicated that the level of maximum strain is lower from laminate with SGP by proof as a more rigid polymer (SGP) can reinforce stiffness in the entire structure. Stress wave

propagation in the presence of more rigid interlayers was compared to that with softer interlayers. The multiple interlayered structure lowers the strain in the backing layer as well as preventing the peeling of large glass fragments. The monolithic glass is showed a better structural performance than laminated glass, however, under high velocity soft impact, the fracture is initiated from the impacted side of monolithic glass, which then propagates through the thickness and leads to the total failure of the structure while in the laminated glass, the failure in the frontal glass layer is isolated and cannot propagate through the interlayer.

7.4. Overall summary

Overall, seven laminated glass cases have been studied at three velocity ranges (quasi static, low velocity and high velocity). Comparison of mechanical and structural performances of glass type, polymer interlayer thickness, polymer interlayer type and multi layered interlayer have been studied to investigate the effect of the performance of laminated glass. The strain level needed to break both the monolithic glass plate and the supporting glass side from laminated glass are around 0.8 % for chemically strengthened glasses. This can be used as a failure criterion on actual windshield design for this particular type of chemically strengthened glass from the sponsor.

At different speed ranges, an increase of TPU polymer thickness has caused different structural responses from the laminated glasses. For quasi static range, by increasing TPU thickness, the fracture sequence changed from the supporting 4.0 mm glass breaking first, to a fracture of the frontal 2.2 mm glass first. As a result, this increased the energy consumption calculated from the area underneath the load versus cross head displacement curves. In the low velocity range, the same fracture sequence was observed as in quasi static rigid ring compression. In general, experimental results from the low velocity demonstrated an increase of the energy consumption as calculated from the area underneath the load versus cross head displacement curves with an increase of the TPU polymer thickness. In the high velocity range, for a thicker TPU interlayer, the load and deformation imposed by the projectile on the frontal glass layer can spread over a wider area on the glass breaking layer and consequently lower the strain values, which improves the ability of impact resistance. To sum up, a thicker polymer interlayer (TPU in this case) can reinforce laminated structure by either enhanced energy tolerance in the quasi static and low velocity ranges or lowered strain at the supporting face of the laminate during the contact in the high velocity range.

For the effect of frontal glass types used in the laminated structure, it was proven that in both quasi static and low velocity ranges, there was more energy absorbed from laminated glass using chemically strengthened frontal glass comparing that of thermally strengthened. Due to specimen shortage, high velocity experiments will be left for future research.

For the effect of polymer interlayer types, one noticeable phenomenon was that PVB effectively shifted from rubbery behaviour material to viscoelastic material by having a glassy elasto-plastic behaviour with a linear initial gradient as the strain rate increased in the low velocity range. All this occurred at room temperature, which is in the glass transition temperature range. This also indicates that the ultimate stress required to break PVB will increase with an increase in strain rate, which benefits the laminate structure at high strain rates. However, from the gas gun results those have been described previously, SGP was more applicable for high velocity purposes. The density of SGP ($\rho \approx 0.95 kgm^{-3}$) is similar to that of TPU and PVB and still is nearly one third of glass ($\rho \approx 2500 kgm^{-3}$). But, the elastic modulus of SGP is two orders of magnitude greater than TPU or PVB, and as a result SGP has closer acoustic properties to that of the glass. This makes SGP a better candidate in lowering the supporting layer strain. However, the experimental evidence showed poor adhesion properties of SGP and glass. TPU is considered as a better adhesive agent between SGP and glass comparing to PVB. This leads to a further design of a multi layered interlayer system using TPU as the adhesive interlayer and SGP as the major structural interlayer. This has been further proven by results from the gas gun that a multi-interlayered structure lowers the strain on the supporting glass layer (by using SGP as structural interlayer) as well as prevents the peeling off of large glass fragments (by using TPU as adhesive interlayer).

Due to the capacity limit in the laboratory, the laminated samples used in the experiments had only two layers of monolithic glasses whereas a three-glass-layered system is usually applied in the real scenario for airplanes in order to prevent bird strike. Therefore, a structural recommendation for the three-glass-layered system would be: a multi layered interlayer system using structural layer of SGP and adhesive layer of TPU in a combination for both lowering the strain in the supporting layer and preventing the peeling off of large glass fragments. In addition, an extra layer of thick TPU can be attached behind the multi layered structure with a final layer of monolithic glass at the back facing control cabin in order to guarantee the safety and further spread concentrated stress and lower the strain on the final monolithic glass layer.

8. Suggestions for future works

Parts of this study could be enhanced by future research. Suggestions for future work are summarized below.

8.1. Mechanical performance of monolithic and laminated glass at quasi static level

For ring on ring compression tests at the quasi-static level, reasonable results have been obtained from 3D DIC design using a first layer mirror. However, a better but more expensive prism could be applied for high light reflection to improve the accuracy of the 3D DIC technique.

A difference in the tin and air sides of glass from manufacturers makes a minor difference in mechanical performance when glass is placed on the supporting side facing maximum tensile stress. This difference may affect the mechanical performance and Weibull probability of the glass. Because many repeats in the test have been conducted, there is a limited number of specimens that can be tested. For the next possible tests, this could be a variable for future experimental plans.

.

8.2. Mechanical performance of laminated glass at low velocity

Due to the limitation of the rig design, no 3D DIC was applied in this part of the experiment. A modification on the current rig could be beneficial to adapting 3D DIC by using similar techniques as in quasi-static ring on ring compression.

Due to the cost of the experiments, the testing specimen was limited. More testing specimens would definitely increase the credibility of this study and more could be understood about other performance aspects like different shapes of projectiles.

8.3. Mechanical performance of laminated glass at high velocity

Due to the cost of the experiments, the testing specimens were limited. More testing specimens would definitely increase the credibility of this study and more could be understood about other performance aspects like different shapes of projectiles and different hydrodynamic profiles.

Different projectiles could be studied on impact performance as well. This would allow us to have a better understanding of the contact time and fracture mechanical behaviour.

8.4. Peeling test

Adhesion property is always the interest of the research for laminate. A good adhesion property improves the performance of the laminate. A large number of literatures have been carried out on the analysis of adhesion. From the large amount of peeling off of glass fragments on laminated glass using an SGP interlayer, we can see that an understating of the adhesion properties between glass and polymer is important. Interpreting and understanding these peeling properties could lead to a better understanding of the types of the polymer that can be used as an adhesive layer and structural layer for the purpose of interlayer design.

Four configurations of laminate structures were compared in previous study which have not included in this thesis: PVB, TPU, SGP and SGP/TPU. Three adhesive fracture energy calculation methods were used: linear elastic fracture mechanism with stiffness approach, with cohesive zone model approach and ICPEEL spreadsheet. Results were compared. Due to soft material property of PVB and TPU, large elongation of peeling arm caused overestimated stretching contribution. As a result, adhesive fracture energy of PVB, TPU, SGP/TPU were overestimated. However, SGP/TPU showed largest results in all three methods. This proved the reason of using multi interlayer structural and showed potential application of this configuration. Further study is expected.

List of publication

Journal

Wang, Y., Mohagheghian, I., Jiang, L., Zhang, X., Yan, Y., Kinloch, A.J. and Dear, J.P. Structural performance of laminated glass windows", Material Science & Eng (A), In draft to be submitted.

Del Linz, P., Wang, Y., Hooper, P.A., Arora, H., Smith, D., Pascoe, L., Cormie, D., Blackman, B.R.K. and Dear, J.P., "Rate dependant mechanical properties of Polyvinyl Butyral", In draft.

Mohagheghian, I., Wang, Y., Guo, X., Yan, Y. and Dear, J.P. "Low velocity soft impact performance of laminated glass windows", International Journal of Solids and Structures, In draft to be submitted.

Mohagheghian, I., Wang, Y., Guo, X., Yan, Y., Dear, J.P. "High velocity soft impact damage of laminated glass windows", Journal of Impact Engineering, In draft to be submitted.

Jiang, L., Wang, Y., Mohagheghian, I., Li, X., Guo, X., Li, L., Dear, J.P., Yan, Y. Effect of residual stress on the fracture of chemically-strengthened thin aluminasilicate glass.

Jiang, L., Wang, Y., Mohagheghian, I., Li, X., Guo, X., Li, L., Dear, J.P., Yan, Y. Subcritical crack growth and lifetime prediction of chemical-strengthened aluminasilicate glass.

Zhang, X., Wang, Y., Mohagheghian, I., Guo, X., Dear, J.P., Yan, Y. The mechanical properties and the phase transition behaviour of a thermoplastic polyurethane.

Conference

Wang, Y., Zhang, X., Jiang, L., Arora, H. and Dear, J.P, "Impact resistance of laminated glass transparencies", ICEM16 - 16th International Conference on Experimental Mechanics, Barton, J. ed, University of Cambridge, UK, (7-11 July, 2014), Paper Ref: 747AT2E3.

To be published in Procedia Engineering and considered for publication in Journal of Materials Processing Technology.

Kelly, M., Arora, H., Del Linz, P., Worley, A., Kaye, M., Wang, Y., Chen, S., Yu, L., Fergusson, A., Hooper, P.A. and Dear, J.P., "Blast loading of composite sandwich structures", 7th International Conference (Technical Committee 4) on Fracture Mechanics related

to Polymers, Polymeric Composites and Adhesives, organised by the European Structural Integrity Society, Williams, J.G. and Blackman, B.R.K. eds.,Les Diablerets, Switzerland,

(14-18 September, 2014), Paper Ref: ESIS2014_0162. http://www.esistc4conference.com/

Del Linz, P., Wang, Y., Hooper, P.A., Smith, D., Cormie, D. Pascoe, L., Blackman, B.R.K. and Dear, J.P., "Reaction force and delamination properties of laminated glass windows subject to blast loads", 5th International Conference on Design and Analysis of Protective Structures (DAPS 2015), Furama Riverfront Hotel, Singapore, (19-21 May 2015), Paper 4.

9. References

[1] Nicholson R, Reed WS. Strategies for Prevention of Bird-Strike Events [Internet]. AERO Copyright © The Boeing. 2011. Available from: http://www.boeing.com/commercial/aeromagazine/articles/2011_q3/4/

[2] SKYbrary. Bird Strike [Internet]. EUROCONTROL. 2015 [cited 2015 Sep 21]. p. Bird Strike Risk and Military Flights. Available from: http://www.skybrary.aero/index.php/Bird_Strike#Bird_Strike_Risk_and_Military_Flights

[3] Maragakis I. Bird population trends and their impact on Aviation safety 1999-2008. Saf Report, Saf Anal Res Dep Eur Aviat Saf Agency. 2008;1–20.

[4] Hanna J, Thomas J. Hail cracks plane's windshields, forces emergency landing [Internet]. CNN. [cited 2015 Aug 9]. Available from: http://edition.cnn.com/2015/08/08/us/delta-emergency-landing-hail/

[5] NRC. NRC bird gun [Internet]. National Research Council of Canada. [cited 2015 May 5]. Available from: http://www.nrc-cnrc.gc.ca/eng/achievements/highlights/2008/chicken_cannon.html

[6] Édouard Bénédictus. Édouard Bénédictus - Inventor of laminated glass [Internet]. Saint Gobain. 2015 [cited 2015 Jun 7]. Available from: http://www.saint-gobain350years.com/#!/en/the-faces-of-saint-gobain/edouard-benedictus

[7] PPG Industries I. PPG Aerospace [Internet]. 2015 [cited 2015 Jun 7]. Available from: http://www.ppgaerospace.com/About-Us/History.aspx

[8] PPG Aerospace. 717, McDonnell Douglas DC-9, MD-80, MD-90 cockpit windows technical data [Internet]. [cited 2015 Jun 6]. Available from: http://www.ppgaerospace.com/Products/Transparencies/Commercial-Aviation.aspx

[9] PPG Aerospace. Next-Generation 737, Classic 737, 727, 707 Cockpit windows [Internet]. [cited 2015 Jun 6]. Available from: http://www.ppgaerospace.com/Products/Transparencies/Commercial-Aviation.aspx

[10] PPG Aerospace. Commercial Aviation 747 cockpit windows [Internet]. [cited 2015 Jun 6]. Available from: http://www.ppgaerospace.com/Products/Transparencies/Commercial-Aviation.aspx

[11] PPG Aerospace. Airbus - A300 / A310 / A330 / A340 cockpit windows [Internet]. [cited 2015 Jun 6]. Available from: http://www.ppgaerospace.com/Products/Transparencies/Commercial-Aviation.aspx

[12] PPG Aerospace. Airbus - A318 / A319 / A320 / A321 cockpit windows [Internet]. [cited 2015 Jun 6]. Available from: http://www.ppgaerospace.com/Products/Transparencies/Commercial-Aviation.aspx

[13] PPG Aerospace. McDonnell Douglas (Boeing) DC-10/MD-11 [Internet]. [cited 2015 Jun 6]. Available from: http://www.ppgaerospace.com/Products/Transparencies/Commercial-Aviation/McDonnell-Douglas-(Boeing)-DC-10-MD-11.aspx

[14] DEPARTMENT OF TRANSPORTATION. Sec. 25.775 - Windshields and windows. [Internet]. FEDERAL AVIATION REGULATIONS. [cited 2015 Sep 21]. Available from: https://www.law.cornell.edu/cfr/text/14/25.775

[15] Linz P Del, Hooper P, Arora H, Smith D, Cormie D, Dear J. Blast loading of Laminated glass windows.

[16] Hooper P. BLAST PERFORMANCE OF SILICONE-BONDED L A M I N AT E D G L A S S paul hooper March 2011 Mechanics of Materials Department of Mechanical Engineering Imperial College London A thesis submitted for the degree of Doctor of Philosophy of Imperial College London. 2011;(March).

[17] Standard B. Bullet resistant glazing — Part 1: Specification for glaszing for interior use. Br Stand. 1988;BS 5051-1.

[18] Standard B. Security glazing, Testing and classification of resistance against. Br Stand - Glas Build. 2000;(356).

[19] Products G, Tem- F, Vehicle M. Standard Test Method for Ball Drop Impact Resistance of Laminated Architectural Flat. ASTM. 2014;1–4.

[20] British Standard. Glass in building — Pendulum test — Impact test method and classification for flat glass. Br Stand - Glas Build. 2002;(12600).

[21] Standard B. Security glazing - Testing and classification of resistance against bullet attack. Br Stand - Glas Build. 2000;(1063).

[22] ASTM. Standard Test Method for Security Glazing Materials And Systems 1. ASTM. 2014;08(Reapproved 2013):1–13.

[23] British Standard. Glass in building Coaxial double ring test on flat specimens with small test surface areas. Br Stand 1288-5. 2000;

[24] ASTM C 1499-04. Standard Test Method for Monotonic Equibiaxial Flexural Strength of Advanced Ceramics at Ambient Temperature. 2013;1–11.

[25] Methods ST. Standard Test Methods for Flexural Properties of Unreinforced and Reinforced Plastics and Electrical Insulating Materials 1. ASTM. :1–11.

[26] British Standard. Determination of the bending strength of glass. Part 3. Test with specimen supported at two points (four point bending). Br Stand - Glas Build. 2000;(1288-3).

[27] Conshohocken W. Standard Test Method for 90 Degree Peel Resistance of Adhesives 1. 2012;1–6.

[28] Toshihiko Ono. Glass Strength and Failure. 2005.

[29] Ledbetter SR, Walker AR, Keiller AP. Structural Use of Glass. J Archit Eng. 2006 Sep;12(3):137–49.

[30] Timoshenko S, Woinowsky-Krieger S. Theory of plates and shells. Mcgraw-Hill College; 1959. 396 p.

[31] Kao R, Perrone N. Large-Deflection Solution o f the Coaxial-Ring- Circular-glass plate Flexure Problem Ea bl. 1971;54(11).

[32] Wilcox DI, Akarapu RK, Gulati ST, Widjaja S. Biaxial Stress in Thin Glass during Ring-on-Ring Testing with Large Deflections. 2013;874–6.

[33] Pećanac G, Bause T, Malzbender J. Ring-on-ring testing of thin, curved bi-layered materials. J Eur Ceram Soc [Internet]. 2011 Oct;31(12):2037–42. Available from: http://linkinghub.elsevier.com/retrieve/pii/S0955221911002512

[34] Bennison SJ, Jagota A, Smith CA. Fracture of Glass/Poly(vinyl butyral) (Butacite®) Laminates in Biaxial Flexure. J Am Ceram Soc [Internet]. 1999 Jul;82(7):1761–70. Available from: http://doi.wiley.com/10.1111/j.1151-2916.1999.tb01997.x

[35] Vepakomma KH, Westbrook J, Carley S, Kim J. Finite Element Analysis of Ring-on-Ring Test on LCD Panels. 2013;9(8):673–7.

[36] Mostafavi M, Marrow TJ. In situ observation of crack nuclei in poly-granular graphite under ring-on-ring equi-biaxial and flexural loading. Eng Fract Mech [Internet]. Elsevier Ltd; 2011 May;78(8):1756–70. Available from: http://linkinghub.elsevier.com/retrieve/pii/S0013794410004674

[37] Hooper J a. On the bending of architectural laminated glass. International Journal of Mechanical Sciences. 1973. p. 309–23, Vol 15.

[38] M.P. Linden, J.E. Minor, R.A. Behr CVGV. Evaluation of Laterally Loaded Glass Units by Theory and Experiment. Glas Res Test Lab Texas Tech Univ Lubbock, Texas. 1983;(NTIS Accession No. PB84-216423).

[39] Vallabhan CVG, Minor JE, Nagalla SR. Stresses in Layered Glass Units and Monolithic Glass Plates. J Struct Eng. 1987 Jan;113(1):36–43.

[40] Minor JE, Reznik PL. Failure Strengths of Laminated Glass. Journal of Structural Engineering. 1990. p. 1030–9 Vol 116.

[41] Behr RA, Minor JE, Norville HS. Structural Behavior of Architectural Laminated Glass. J Struct Eng. 1993 Jan;119(1):202–22.

[42] Bennison SJ, Smith C a., Van Duser a., Jagota A. Structural Performance of Laminated Glass Made with a “Stiff” Interlayer. Glas Process Days 2001 [Internet]. 2001;(June):283–7. Available from: http://www.glassfiles.com/library/22/article511.htm

[43] Norville HS, King KW, Swofford JL. Behavior and Strength of Laminated Glass. J Eng Mech. 1998 Jan;124(1):46–53.

[44] Duser A Van, Jagota A, Bennison SJ. Analysis of Glass/Polyvinyl Butyral Laminates Subjected to Uniform Pressure. J Eng Mech. 1999 Apr;125(4):435–42.

[45] Ivanov I V. Analysis, modelling, and optimization of laminated glasses as plane beam. Int J Solids Struct. 2006 Nov;43(22-23):6887–907.

[46] Jalham IS, Alsaed O. The Effect of Glass Plate Thickness and Type and Thickness of the Bonding Interlayer on the Mechanical Behavior of Laminated Glass. New J Glas Ceram. 2011;01(02):40–8.

[47] Shitanoki Y, Bennison SJ, Koike Y. Structural behavior thin glass ionomer laminates with optimized specific strength and stiffness. Compos Struct [Internet]. Elsevier Ltd; 2015 Jul;125:615–20. Available from: http://linkinghub.elsevier.com/retrieve/pii/S0263822315000896

[48] Backman ME, Goldsmith W. The mechanics of penetration of projectiles into targets. Int J Eng Sci. 1978;16(1):1–99.

[49] Dharani LR, Yu J. Failure modes of glass panels subjected to soft missile impact. Damage Fract Mech VIII. 2004;

[50] Shetty MS, Dharani LR, Stutts DS. Analysis of Laminated Architectural Glazing Subjected to Wind Load and Windborne Debris Impact. ISRN Civ Eng. 2012;2012:1–9.

[51] Pacios A, Postigo S, Huerta C. Relationship between characteristic parameters of impact test for safety glasses. Stahlbau. 2011;

[52] Pyttel T, Liebertz H, Cai J. Failure criterion for laminated glass under impact loading and its application in finite element simulation. Int J Impact Eng [Internet]. Elsevier Ltd; 2011 Apr [cited 2012 Nov 16];38(4):252–63. Available from: http://linkinghub.elsevier.com/retrieve/pii/S0734743X10001934

[53] Untaroiu CD, Shin J, Crandall JR. A design optimization approach of vehicle hood for pedestrian protection. Int J Crashworthiness. 2007;12(6):581–9.

[54] Zhao S, Dharani LR, Chai L, Barbat SD. Analysis of damage in laminated automotive glazing subjected to simulated head impact. Eng Fail Anal. 2006;13(4):582–97.

[55] Dolbeer R, Wright S. Wildlife strikes to civil aircraft in the United States 1990–2013. Other Bird Strike Aviat Mater. 2014;24:1–57, Vol 24.

[56] Mccreary I, Kingdom U, Reserved AR. The frequency and economic cost of bird strikes. 2009;(400).

[57] Thorpe J. Fatalities and destroyed civil aircraft due to bird strikes, 1912-2002. Int Bird Strike Committee, 26th Meet …. 2003;(May):5–9.

[58] Atkins Ltd., Food and Environment Research Agency (FERA), Easa for the. Bird Strike Damage & Windshield Bird Strike. 2007;1–181.

[59] Doubrava R, Strnad V. Bird strike analyses on the parts of aircraft structure. Proc 27th Congr …. 2010;

[60] Kangas P, Pigman GL. Develpment of Aircraft Windshield to resist impact with birds in flight Part II. Tech Dev Rep. 1950;

[61] Salehi H, Ziaei-Rad S, Vaziri-Zanjani M a. Bird impact effects on different types of aircraft bubble windows using numerical and experimental methods. Int J Crashworthiness. 2010;15(1):93–106.

[62] Wang FS, Yue ZF. Numerical simulation of damage and failure in aircraft windshield structure against bird strike. Mater Des [Internet]. Elsevier Ltd; 2010;31(2):687–95. Available from: http://dx.doi.org/10.1016/j.matdes.2009.08.029

[63] Dar UA, Zhang W, Xu Y. FE Analysis of Dynamic Response of Aircraft Windshield against Bird Impact. 2013;2013.

[64] Wang J, Xu Y, Zhang W. Finite element simulation of PMMA aircraft windshield against bird strike by using a rate and temperature dependent nonlinear viscoelastic constitutive model. Compos Struct. Elsevier Ltd; 2014;108:21–30.

[65] Grimaldi a., Sollo a., Guida M, Marulo F. Parametric study of a SPH high velocity impact analysis – A birdstrike windshield application. Compos Struct. Elsevier Ltd; 2013;96:616–30.

[66] Hedayati R, Ziaei-Rad S, Eyvazian A, Hamouda AM. Bird strike analysis on a typical helicopter windshield with different lay-ups. J Mech Sci Technol. 2014;28(4):1381–92.

[67] Wilbeck J. Impact behavior of low strength projectiles. Tech Rep AFML-TR-77-134. 1978;

[68] Wilbeck J, Rand J. The development of a substitute bird model. J Enginnering Power. 1981;103:725–30.

[69] Barber J, Taylor H, Wilbeck J. Bird impact forces and pressures on rigid and compliant targets. Tech Rep AFFDL-TR-77-60. 1978;(December 1976).

[70] Huntsman. Product Overview - Optical Aliphatic Films - PE499 [Internet]. 2009. Available from: http://www.huntsman.com/polyurethanes/Media Library/a_MC1CD1F5AB7BB1738E040EBCD2B6B01F1/Products_MC1CD1F5AB8081738E040EBCD2B6B01F1/Thermoplastic polyur_MDC92D212C2A5565FE040EBCD2B6B3E40/files/Product_Overview_screen2_10_2009.pdf

[71] Juang Y, Lee LJ, Koelling KW. Rheological analysis of polyvinyl butyral near the glass transition temperature. Polym Eng Sci [Internet]. 2001 Feb;41(2):275–92. Available from: http://doi.wiley.com/10.1002/pen.10727

[72] Optics E. First surface mirrors [Internet]. Edmund Optics Inc. 2015 [cited 2015 Oct 3]. Available from: http://www.edmundoptics.com/optics/optical-mirrors/flat-mirrors/51mm-larger-experimental-grade-first-surface-mirrors/3546/

[73] Ltd P. White Silicone Cord 60 shore [Internet]. 2015 [cited 2015 Nov 27]. Available from: https://www.polymax.co.uk/rubber-cords/silicone-cord/white-silicone-cord

[74] Aramis. User Information - Hardware. GOM. 2011;Page 11.

[75] National Instruments Corporation. Measuring Strain with Strain Gages [Internet]. National Instruments Corporation. [cited 2015 Oct 3]. Available from: http://www.ni.com/white-paper/3642/en/

[76] ASTM C1239-13. Standard Practice for Reporting Uniaxial Strength Data and Estimating Weibull Distribution Parameters for Advanced Ceramics. 2014;1–18.

[77] Collini L, Carfagni GR. Flexural strength of glass – ceramic for structural applications. J Eur Ceram Soc. Elsevier Ltd; 2013;

[78] Veer F a, Riemslag T, Romein T. The failure strength of glass, a non transparent value. Glas Perform Days 2007. 2007;610–4.

[79] Morrell R. Biaxial flexural strength testing of ceramic materials. Measurement Good Practice Guide No 12. National Physical Laboratory;

[80] Phantom. Phantom Miro M / R / LC310 [Internet]. 2015 [cited 2015 Oct 4]. Available from: http://www.visionresearch.com/Products/High-Speed-Cameras/Miro-M310/

[81] J-Flex Rubber. Translucent 40° Shore Silicone Sheet [Internet]. J-Flex Rubber. 2015 [cited 2015 Dec 1]. Available from: http://www.j-flex.co.uk/wp-content/uploads/FOOD-QUALITY-SILICONE-RUBBER-TRANSLUCENT-40-SHORE.pdf

[82] Manufacturing CB, Specimens CR, Determina- T, Sheets SV. Standard Test Methods for Vulcanized Rubber and Thermoplastic Elastomers —. 2015;(Reapproved 2013):1–14.

[83] Measurement IL-NCP. Accuracy: Strain [Internet]. Non Contact Precision. 2015 [cited 2015 Sep 30]. Available from: http://www.imetrum.com/how-it-works/

[84] Dolbeer R, Wright S. Wildlife strikes to civil aircraft in the United States 1990–2013. Other Bird Strike Aviat Mater [Internet]. 2014;24:1–57. Available from: http://digitalcommons.unl.edu/birdstrikeother/24/

[85] Sutton M, Orteu J, Schreier H. Image Correlation for Shape, Motion Measurements, and Deformation. Springer; 2009.

[86] Field JE. Stress Waves, Deformation and Fracture Caused by Liquid Impact. Philosophical Transactions of the Royal Society A: Mathematical, Physical and Engineering Sciences. 1966. p. 86–93.